The Astrophysical Journal Supplement Series, 233:17 (38pp), 2017 December https://doi.org/10.3847/1538-4365/aa96ad

BAT AGN Spectroscopic Survey. V. X-Ray Properties of the *Swift*/BAT 70-month AGN Catalog

C. Ricci[1,2,3,4], B. Trakhtenbrot[5,22], M. J. Koss[5], Y. Ueda[2], I. Del Vecchio[6], E. Treister[1], K. Schawinski[5], S. Paltani[7], K. Oh[5], I. Lamperti[5], S. Berney[5], P. Gandhi[8], K. Ichikawa[9,10,11], F. E. Bauer[1,12,13], L. C. Ho[3,14], D. Asmus[15], V. Beckmann[16], S. Soldi[17], M. Baloković[18], N. Gehrels[19], and C. B. Markwardt[20,21]

[1] Instituto de Astrofísica, Facultad de Física, Pontificia Universidad Católica de Chile, Casilla 306, Santiago 22, Chile; cricci@astro.puc.cl
[2] Department of Astronomy, Kyoto University, Oiwake-cho, Sakyo-ku, Kyoto 606-8502, Japan
[3] Kavli Institute for Astronomy and Astrophysics, Peking University, Beijing 100871, China
[4] Chinese Academy of Sciences South America Center for Astronomy and China-Chile Joint Center for Astronomy, Camino El Observatorio 1515, Las Condes, Santiago, Chile
[5] Institute for Astronomy, Department of Physics, ETH Zurich, Wolfgang-Pauli-Strasse 27, CH-8093 Zurich, Switzerland
[6] Department of Physics, University of Zagreb, Bijenička cesta 32, HR-10002 Zagreb, Croatia
[7] Department of Astronomy, University of Geneva, ch. d'Ecogia 16, CH-1290 Versoix, Switzerland
[8] School of Physics & Astronomy, University of Southampton, Highfield, Southampton, SO17 1BJ, UK
[9] National Astronomical Observatory of Japan, 2-21-1 Osawa, Mitaka, Tokyo 181-8588, Japan
[10] Department of Physics and Astronomy, University of Texas at San Antonio, One UTSA Circle, San Antonio, TX 78249, USA
[11] Department of Astronomy, Columbia University, 550 West 120th Street, New York, NY 10027, USA
[12] Space Science Institute, 4750 Walnut Street, Suite 205, Boulder, CO 80301, USA
[13] Millenium Institute of Astrophysics, Santiago, Chile
[14] Department of Astronomy, School of Physics, Peking University, Beijing 100871, China
[15] European Southern Observatory, Casilla 19001, Santiago 19, Chile
[16] CNRS/IN2P3, 3 rue Michel Ange, F-75794 Paris Cedex 16, France
[17] Centre Franois Arago, APC, Universit Paris Diderot, CNRS/IN2P3, 10 rue Alice Domon et Léonie Duquet, F-75205 Paris Cedex 13, France
[18] Cahill Center for Astronomy and Astrophysics, California Institute of Technology, Pasadena, CA 91125, USA
[19] NASA Goddard Space Flight Center, Mail Code 661, Greenbelt, MD 20771, USA
[20] Department of Astronomy, University of Maryland, College Park, MD 20742, USA
[21] Astroparticle Physics Laboratory, Mail Code 661, NASA Goddard Space Flight Center, Greenbelt, MD 20771, USA
Received 2016 November 10; revised 2017 August 31; accepted 2017 September 10; published 2017 December 5

Abstract

Hard X-ray ($\geqslant$10 keV) observations of active galactic nuclei (AGNs) can shed light on some of the most obscured episodes of accretion onto supermassive black holes. The 70-month *Swift*/BAT all-sky survey, which probes the 14–195 keV energy range, has currently detected 838 AGNs. We report here on the broadband X-ray (0.3–150 keV) characteristics of these AGNs, obtained by combining *XMM-Newton*, *Swift*/XRT, *ASCA*, *Chandra*, and *Suzaku* observations in the soft X-ray band ($\leqslant$10 keV) with 70-month averaged *Swift*/BAT data. The nonblazar AGNs of our sample are almost equally divided into unobscured ($N_{\rm H} < 10^{22}$ cm^{-2}) and obscured ($N_{\rm H} \geqslant 10^{22}$ cm^{-2}) AGNs, and their *Swift*/BAT continuum is systematically steeper than the 0.3–10 keV emission, which suggests that the presence of a high-energy cutoff is almost ubiquitous. We discuss the main X-ray spectral parameters obtained, such as the photon index, the reflection parameter, the energy of the cutoff, neutral and ionized absorbers, and the soft excess for both obscured and unobscured AGNs.

Key words: galaxies: active – galaxies: Seyfert – quasars: general – X-rays: diffuse background – X-rays: general

Supporting material: machine-readable tables

1. Introduction

Active galactic nuclei[23] (AGNs) are among the most energetic phenomena in the universe and are believed to play a significant role in the evolution of galaxies (e.g., Kormendy & Richstone 1995; Ferrarese & Merritt 2000; Gebhardt et al. 2000; Tremaine et al. 2002; Schawinski et al. 2006; Kormendy & Ho 2013). One of the most distinctive features of AGNs is their strong emission in the X-ray regime, which is produced by Comptonization of optical and UV photons (e.g., Haardt & Maraschi 1991) in a hot plasma located very close to the accreting supermassive black hole (SMBH). X-ray emission is therefore an important tracer of the physical properties of the accreting system and can constrain the amount of matter along the line of sight, typically parameterized as the neutral hydrogen column density ($N_{\rm H}$). X-ray emission can also be used to shed light on the structure of the circumnuclear material, by studying the spectral features created by the reprocessing of the primary X-ray radiation on the material surrounding the SMBH. The two main features produced by reprocessing of X-ray radiation in neutral material are the iron Kα line at 6.4 keV and a broad Compton "hump" peaking at $\sim$30 keV (e.g., Matt et al. 1991; Murphy & Yaqoob 2009).

The integrated emission of unresolved AGNs gives rises to the cosmic X-ray background (CXB; e.g., Giacconi et al. 1962; Bauer et al. 2004; Harrison et al. 2016). Studies carried out below 10 keV have shown that the shape of the CXB is significantly flatter (with a photon index $\Gamma \sim 1.4$; e.g., De Luca & Molendi 2004) than the typical X-ray spectrum of unobscured AGNs ($\Gamma \simeq 1.9$; e.g., Nandra & Pounds 1994). This, together with the fact that the CXB shows a clear peak at $\sim$30 keV, where the bulk of the reprocessed X-ray radiation is

[22] Zwicky Fellow.
[23] See Beckmann & Shrader (2012), Netzer (2013, 2015), and Brandt & Alexander (2015) for a recent review on the subject.

emitted, suggests that heavily obscured AGNs contribute significantly to the CXB. Synthesis models of the CXB (e.g., Ueda et al. 2003, 2014; Treister & Urry 2005; Gilli et al. 2007; Treister et al. 2009; Draper & Ballantyne 2010; Akylas et al. 2012) have shown that a fraction of 10%–30% of Compton-thick (CT, $\log(N_{\rm H}/{\rm cm}^{-2}) \geqslant 24$) AGNs are needed to reproduce the CXB. The fraction of CT AGNs inferred from synthesis models of the CXB is, however, strongly dependent on the assumptions made on the fraction of reprocessed X-ray emission, with stronger reflection components resulting in smaller fractions of CT AGNs (e.g., Gandhi et al. 2007; Treister et al. 2009; Ricci et al. 2011; Vasudevan et al. 2013b, 2016; Ueda et al. 2014).

Radiation at hard X-rays ($E \gtrsim 10$ keV) is less affected by the obscuring material, at least up to $N_{\rm H} \sim 10^{23.5}$–10^{24} cm^{-2} (see Figure 1 of Ricci et al. 2015), due to the decline of the photoelectric cross section with increasing energy. Hard X-ray observations are therefore very well suited to detect heavily obscured AGNs and allow us to obtain the least biased X-ray sample of local AGNs and to directly study the X-ray emission responsible for the peak of the CXB. Currently, there are four operating hard X-ray observatories in orbit. IBIS/ISGRI on board *INTEGRAL* (Winkler et al. 2003) was launched in 2002 and has so far detected more than 200 AGNs (Beckmann et al. 2006, 2009; Paltani et al. 2008; Panessa et al. 2008; Ricci et al. 2011; Malizia et al. 2012). *NuSTAR* (Harrison et al. 2013), launched in 2012, is the first on-orbit focusing hard X-ray telescope, and its serendipitous survey has detected 497 sources in the first 40 months of observations (Lansbury et al. 2017b; see also Chen et al. 2017). Thanks to its revolutionary characteristics, *NuSTAR* has been very efficient in constraining the properties of heavily obscured AGNs (e.g., Baloković et al. 2014; Gandhi et al. 2014; Stern et al. 2014; Annuar et al. 2015, 2017; Brightman et al. 2015; Koss et al. 2015, 2016b; Lansbury et al. 2015, 2017a; Boorman et al. 2016; Ricci et al. 2016a, 2016b, 2017a, 2017b). The recently launched mission *AstroSat* (Singh et al. 2014) carries on board two hard X-ray instruments: the Large Area Xenon Proportional Counters (LAXPC; 3–80 keV) and the cadmium–zinc–telluride coded-mask imager (CZTI, 10–150 keV). Finally, the NASA mission *Swift* (Gehrels et al. 2004), launched in 2005, carries on board the Burst Alert Telescope (BAT; Barthelmy et al. 2005; Krimm et al. 2013). BAT is a hard X-ray detector that operates in the 14–195 keV energy range and has proved to be an extremely valuable tool for studying AGNs in the local universe, since it is the only hard X-ray instrument to continuously survey the whole sky.

Early studies of *Swift*/BAT AGNs (e.g., Ajello et al. 2008; Tueller et al. 2008; Winter et al. 2008, 2009a; Burlon et al. 2011; Ajello et al. 2012) were focused on the first releases of the *Swift*/BAT catalog (Markwardt et al. 2005; Cusumano et al. 2010a, 2010b; Segreto et al. 2010; Tueller et al. 2010) or on relatively small subsamples (e.g., Vasudevan et al. 2013a). The latest release of the *Swift*/BAT catalog (70 months; Baumgartner et al. 2013) has, however, considerably increased the number of hard-X-ray-selected AGNs, detecting more than 800 extragalactic sources. The all-sky coverage of *Swift*/BAT allows us to detect very luminous and rare sources, and, being one of the least biased samples of AGNs available, it allows us to study a growing number of local heavily obscured AGNs. A large number of works have already been carried out studying pointed X-ray observations (e.g., Winter et al. 2009b; Ricci et al. 2010; Tazaki et al. 2011, 2013; Kawamuro et al. 2016b; Tanimoto et al. 2016; Marchesi et al. 2017; Oda et al. 2017) and the multiwavelength properties of *Swift*/BAT AGNs. This includes radio (e.g., Burlon et al. 2013; Wong et al. 2016), far-IR (e.g., Meléndez et al. 2014; Mushotzky et al. 2014; Shimizu et al. 2015, 2016), mid-IR (e.g., Meléndez et al. 2008; Weaver et al. 2010; Ichikawa et al. 2012, 2017), near-IR (e.g., Mushotzky et al. 2008; Lamperti et al. 2017; Onori et al. 2017a, 2017b; Ricci et al. 2017d), optical (e.g., Vasudevan et al. 2009; Koss et al. 2010; Winter et al. 2010; Ueda et al. 2015), and γ-ray (e.g., Sambruna et al. 2010; Teng et al. 2011) studies, as well as works focused on the host galaxy properties (e.g., Koss et al. 2011b), on variability (e.g., Shimizu & Mushotzky 2013; Soldi et al. 2014), and on peculiar sources (e.g., Koss et al. 2012; Hogg et al. 2012; Smith et al. 2014; Schawinski et al. 2015). Moreover, *NuSTAR* has been observing *Swift*/BAT AGNs since its launch in the framework of a legacy survey (M. Baloković et al., in preparation), providing high-quality data in the 3–80 keV energy range.

Our group has been working on a systematic study of the multiwavelength properties of a very large number of *Swift*/BAT-selected AGNs from the currently available 70-month catalog (Baumgartner et al. 2013) and a forthcoming extension (105 months; Oh et al. 2017). A large effort has been made to collect optical spectroscopy for most of the sources reported in the 70-month *Swift*/BAT catalog, which allowed us to infer black hole masses for both obscured and unobscured objects (Koss et al. 2017). The first results of the *Swift*/BAT AGN Spectroscopical Survey (BASS) include the study of the CT AGNs detected by BAT (Ricci et al. 2015; see also Koss et al. 2016a; Akylas et al. 2016), the analysis of the correlation between high-ionization optical emission lines and AGN X-ray emission (Berney et al. 2015), the study of the relationship between optical narrow emission lines and the physical parameters of the accreting SMBH (Oh et al. 2017), a near-IR spectroscopic study (Lamperti et al. 2017), and the analysis of the relationship between the X-ray photon index and the mass-normalized accretion rate (Trakhtenbrot et al. 2017). The detailed multiwavelength analysis of a large sample of local AGNs[24] will be a very important benchmark for studies of AGNs at higher redshifts, where the typical fluxes are significantly lower.

In this paper we present a compilation and analysis of the X-ray data available for the AGNs of the 70-month *Swift*/BAT catalog. This paper is structured as follows. In Section 2 we present our sample, in Section 3 we describe the data analysis of the soft X-ray data, and in Section 4 we illustrate the procedure adopted for the broadband X-ray spectral analysis of the sources and the models used. In Section 5.1 we discuss the luminosity and flux distributions of our sample, in Section 5.2 we examine the characteristics of the X-ray continuum, in Section 5.3 we report on the results obtained for the neutral and ionized absorbing material, and in Section 5.4 we discuss the properties of the soft excess of obscured and unobscured AGNs. Finally, in Section 6 we summarize our findings and present our conclusions. Throughout the paper we adopt standard cosmological parameters ($H_0 = 70$ km s^{-1} Mpc^{-1}, $\Omega_{\rm m} = 0.3$, $\Omega_\Lambda = 0.7$). Unless otherwise stated, uncertainties are quoted at the 90% confidence level.

[24] See also She et al. (2017a, 2017b) for a soft X-ray study of lower-luminosity local AGNs.

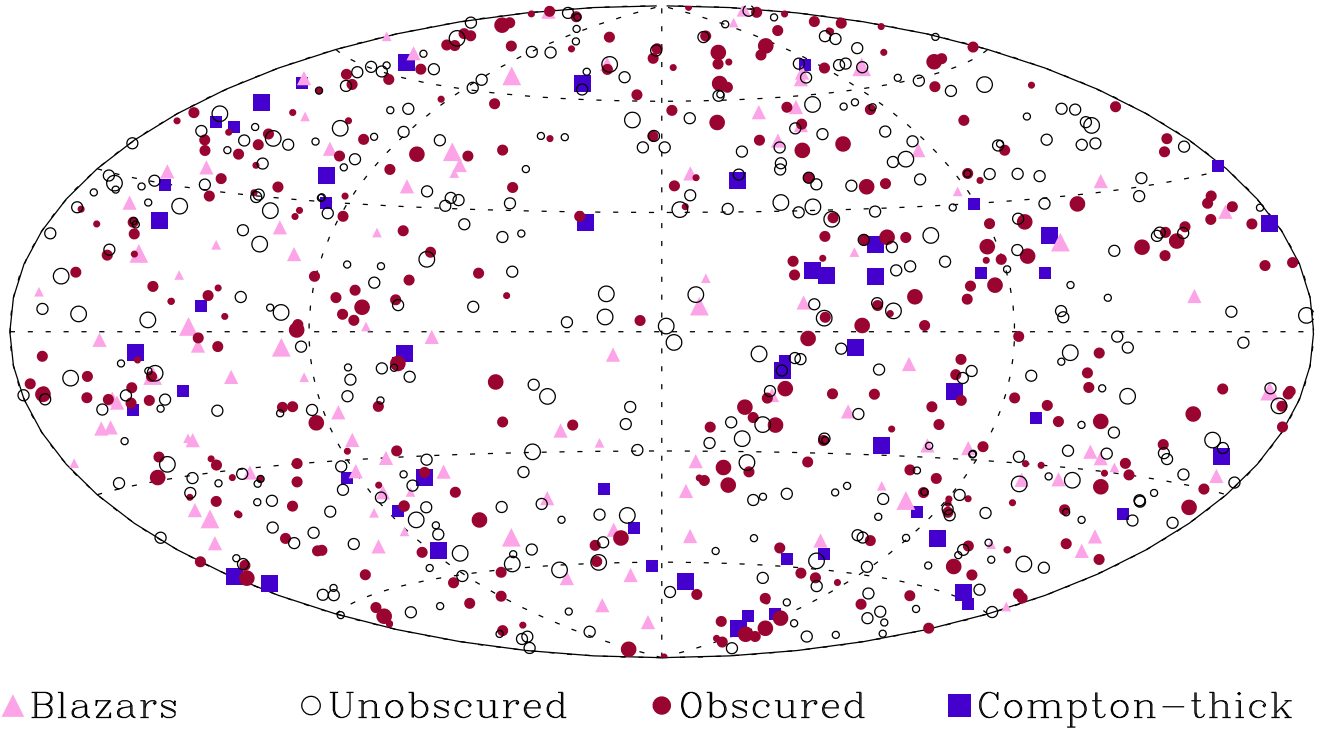

Figure 1. AGNs from the 70-month *Swift*/BAT catalog (Aitoff projection). Sources are divided into nonblazar AGNs and blazars as discussed in Section 2, and different sizes imply different intrinsic fluxes. Nonblazar AGNs are divided, depending on their line-of-sight column density, into unobscured ($N_{\rm H} < 10^{22}$ cm^{-2}), obscured ($10^{22} \leqslant N_{\rm H} < 10^{24}$ cm^{-2}) and CT ($N_{\rm H} \geqslant 10^{24}$ cm^{-2}; see Section 5.3.1 for details on the absorption properties of the sample).

2. Sample

Our sample consists of the 838 AGNs detected within the 70-month *Swift*/BAT catalog[25] (Baumgartner et al. 2013, Figure 1). We flagged all blazars in our sample according to the latest release (5.0.0; Massaro et al. 2015) of the Roma BZCAT[26] catalog (Massaro et al. 2009) and using the results of recent works on BAT-detected blazars (Ajello et al. 2009; Maselli et al. 2013). Overall 105 objects are classified as blazars. Of these, 26 are BL Lacs (BZB), 53 are flat-spectrum radio quasars (BZQ), and 26 are of uncertain type (BZU). This is a different terminology than that used in the optical catalog of Koss et al. (2017), which refers to these sources as beamed AGNs. Several sources have been identified as possible blazars by Koss et al. (2017) using optical spectroscopy and are not treated as blazars here. In Table 1 we report the list of sources in our sample, together with their counterparts, coordinates, redshifts, and blazar classification. For completeness, we also report the results obtained for the only non-AGN extragalactic source detected by *Swift*/BAT, M82 (a nearby starburst with X-ray emission produced by star formation; e.g., Ranalli et al. 2008), although we do not include it in our statistical analysis.

2.1. Counterpart Identification

The counterparts of the *Swift*/BAT sources were mostly taken from Baumgartner et al. (2013) and from recent follow-up studies (e.g., Parisi et al. 2009; Masetti et al. 2010; Lutovinov et al. 2012; Masetti et al. 2012; Parisi et al. 2012). In order to confirm the counterpart association, for all sources we studied the 2–10 keV images of the fields using *XMM-Newton*/EPIC, *Swift*/X-Ray Telescope (XRT), and *Chandra*/ACIS (we provide additional information on these data sets in Section 3). Furthermore, the object coordinates were cross-checked with the Two Micron All Sky Survey (2MASS; Skrutskie et al. 2006) and the *Wide-field Infrared Survey Explorer* (*WISE*; Wright et al. 2010) point-source catalogs, and deviations larger than 3″ were investigated individually. In 27 cases, the coordinates of the associated counterparts in the original BAT catalog do not accurately point to the nuclei of the systems, which in all cases are identified with a relatively bright *WISE* and 2MASS source. In a further five cases the situation is more complex, because the original counterpart does not point to an individual galaxy, but to a pair or triple. In these cases, the closest galaxy to the X-ray source with *WISE* colors consistent with an AGN was selected. In Appendix A we discuss the objects for which new counterparts were found, while in Appendix B we discuss the *Swift*/BAT sources that host dual AGNs. In three cases, where both dual AGNs contributed significantly to the BAT flux, we report the spectral parameters of the two AGNs (named D1 and D2).

2.2. Redshifts and Distances

2.2.1. Spectroscopic Redshifts and Redshift-independent Distances

Spectroscopic redshifts are available for most of the sources of our sample (803, i.e., ∼96%). The redshifts were taken from the first release (DR1) of the BASS optical catalog (Koss et al. 2017) and from the literature. For the closest objects in our sample (at $z < 0.01$), whenever available, we used redshift-independent measurements of the distance, using the mean reported in the NASA/IPAC Extragalactic Database (NED). Redshift-independent distances were considered for 44 objects.

[25] http://swift.gsfc.nasa.gov/results/bs70mon/
[26] http://www.asdc.asi.it/bzcat/

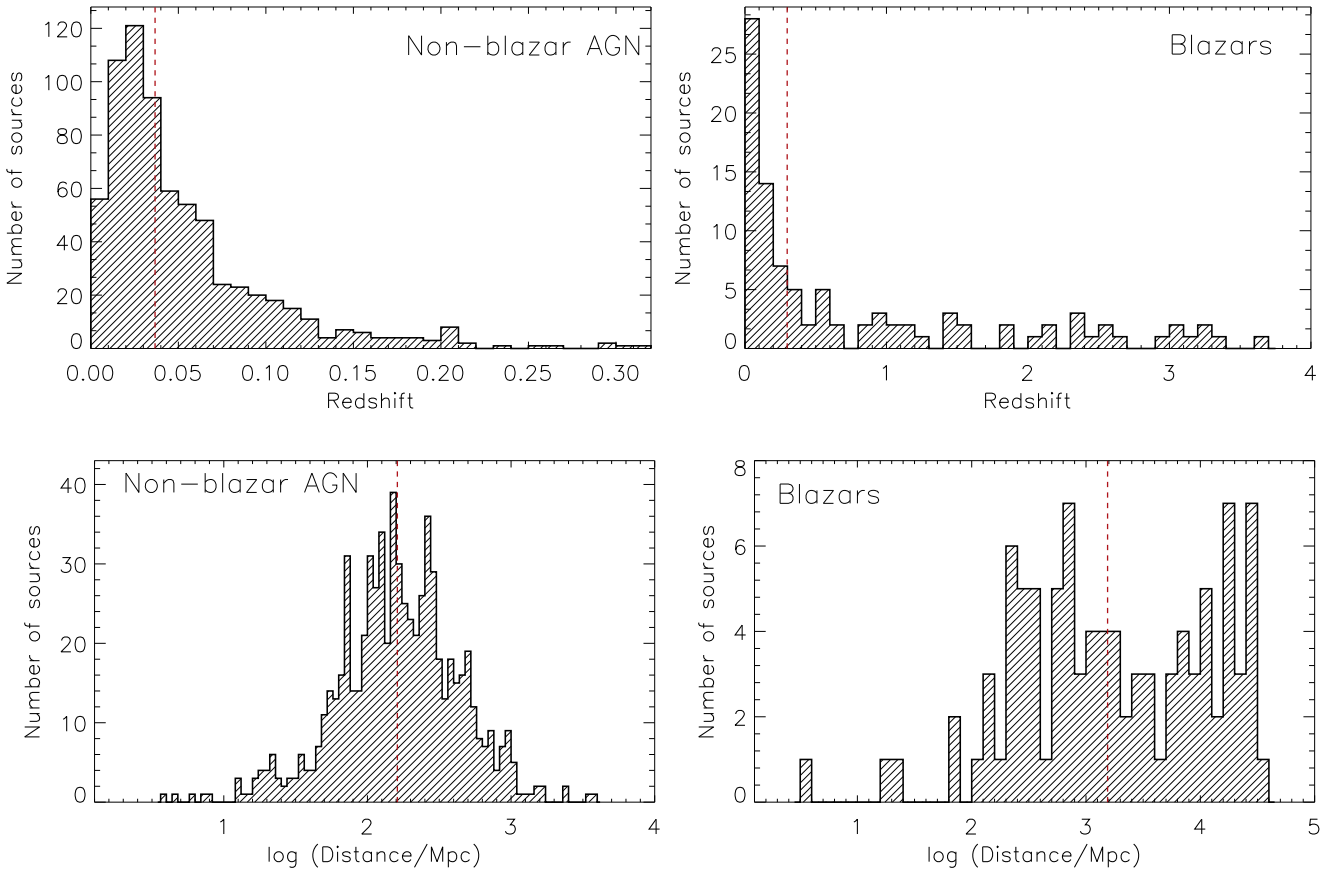

Figure 2. Top left panel: zoom-in of the $z = 0$–0.32 range of the redshift distribution of the nonblazar AGNs of our sample. There are four nonblazar AGNs at $z \geqslant 0.4$ that are excluded from this plot: SWIFT J1131.9−1233 ($z = 0.6540$), SWIFT J2344.6−4246 ($z = 0.5975$), SWIFT J1159.7−2002 ($z = 0.4500$), and SWIFT J0216.3 +5128 ($z = 0.422$). Top right panel: redshift distribution of the blazars. Bottom left panel: distribution of the distances of the nonblazar AGNs of our sample (including the redshift-independent distances). Bottom right panel: same as the bottom left panel, but for the blazars. For all panels the red dashed lines show the median for each sample. Among the 70-month catalog sources, nonblazar AGNs lie at much lower redshifts and distances (median values: $z = 0.0367$, $D = 161.6$ Mpc) compared to the strongly beamed and more luminous (see Section 5.1 and Figure 14) blazar population ($z = 0.299$, $D = 1565.3$ Mpc).

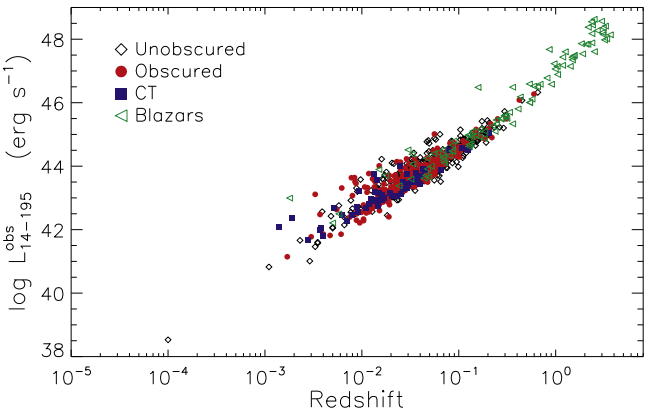

Figure 3. Observed 14–195 keV *Swift*/BAT luminosity vs. redshift for the AGNs of the 70-month *Swift*/BAT catalog. The sources are divided into blazars and nonblazar AGNs, with the latter being further classified into unobscured ($N_H < 10^{22}$ cm^{-2}), obscured ($10^{22} \leqslant N_H < 10^{24}$ cm^{-2}), and CT AGNs ($N_H \geqslant 10^{24}$ cm^{-2}; see Section 5.3.1 for details on the absorption properties of the sample).

The redshift and distance distribution of the nonblazar AGNs and the blazars in our sample are presented in the left and right panels of Figure 2, respectively. The median redshift and distance of nonblazar AGNs ($z = 0.0367$, $D = 161.6$ Mpc) are significantly lower than those of blazars ($z = 0.302$, $D = 1565$ Mpc), consistent with the very different luminosity distributions of these two classes of objects (see Section 5.1 and Figure 14).

Figure 3 presents the observed 14–195 keV *Swift*/BAT luminosity versus redshift for unobscured ($N_H < 10^{22}$ cm^{-2}), obscured ($10^{22} \leqslant (N_H/\mathrm{cm}^{-2}) < 10^{24}$), and CT ($N_H \geqslant 10^{24}$ cm^{-2}) AGNs and blazars in the sample.

2.2.2. Photometric Redshifts

The *Swift*/BAT 70-month sample includes 28 nonblazar AGNs and 7 blazars with no redshift measurement. For the subsample of nonblazar AGNs we calculated photometric redshifts using the LePHARE[27] code (Arnouts et al. 1999; Ilbert et al. 2006), which is a spectral energy distribution (SED) fitting code based on χ^2 minimization. We adopted a set of templates from Salvato et al. (2009, 2011), which includes some AGN models from Polletta et al. (2007) and hybrid templates combining AGN and host galaxy emission. This library has been optimized and extensively tested for SED fitting of AGN-dominated sources (see Salvato et al. 2009, for further details). Dust extinction was added to each template as a free parameter in the fit, by assuming the Calzetti et al. (2000) attenuation law.

[27] http://www.cfht.hawaii.edu/~arnouts/LEPHARE/lephare.html

Table 1
List of the *Swift*/BAT AGNs from the 70-month Catalog

(1) Source	(2) Counterpart	(3) R.A.	(4) Decl.	(5) Redshift	(6) Distance (Mpc)	(7) BZCAT
SWIFT J0001.0−0708	2MASX J00004876-0709117	0.2032	−7.1532	0.0375	165.2	⋯
SWIFT J0001.6−7701	2MASX J00014596−7657144	0.4419	−76.9540	0.0584	261.2	⋯
SWIFT J0002.5+0323	NGC 7811	0.6103	3.3519	0.0255	111.3	⋯
SWIFT J0003.3+2737	2MASX J00032742+2739173	0.8643	27.6548	0.0397	175.2	⋯
SWIFT J0005.0+7021	2MASX J00040192+7019185	1.0082	70.3217	0.0960	440.7	⋯
SWIFT J0006.2+2012	Mrk 335	1.5813	20.2029	0.0258	112.7	⋯
SWIFT J0009.4−0037	SDSS J000911.57−003654.7	2.2982	−0.6152	0.0733	331.3	⋯
SWIFT J0010.5+1057	Mrk 1501	2.6292	10.9749	0.0893	408.1	BZQ
SWIFT J0017.1+8134	[HB89] 0014+813	4.2853	81.5856	3.3660	29188.0	BZQ
SWIFT J0021.2−1909	LEDA 1348	5.2814	−19.1682	0.0956	438.7	⋯

Notes. Column (1): *Swift*/BAT ID. Column (2): name of the counterpart. Columns (3) and (4): coordinates (in degrees, J2000). Column (5): redshift. Column (6): distance in Mpc. Column (7): BZCAT class.
[a] For these sources only a photometric redshift (and its 1σ confidence interval) is reported.
[b] Sources for which redshift-independent measurements of the distance are reported.
(This table is available in its entirety in machine-readable form.)

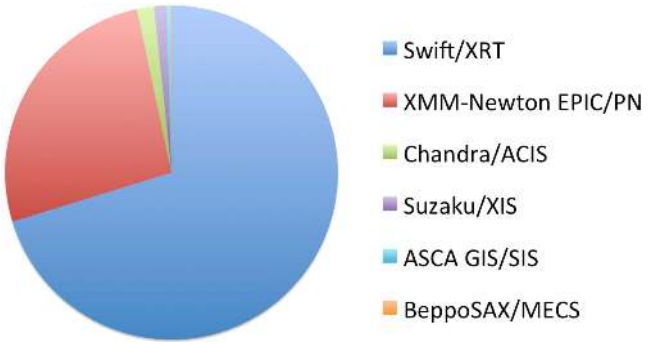

Figure 4. Facilities and instruments used for the analysis of the soft X-ray spectra (see Table 3).

To perform the SED fitting, we collected multiwavelength photometry in the ultraviolet, optical, and infrared regimes. We made use of the publicly available data from the *Galaxy Evolution Explorer* (*GALEX*; Martin et al. 2005) in the far-ultraviolet ($\lambda \sim 1550$ Å); the Sloan Digital Sky Survey Data Release 10 (SDSS-DR10; Ahn et al. 2014) in the optical (u, g, r, i, and z bands); the 2MASS catalog in the near-infrared (J, H, and K_s bands); the *WISE* and *AKARI* catalogs in the mid-infrared ($\lambda \sim 3.4$, 4.6, 12, 18, and 22 μm); and the *Infrared Astronomical Satellite* (*IRAS*; Neugebauer et al. 1984) in the far-infrared ($\lambda \sim 60$ and 100 μm). We collected broadband photometry for 27 out of the 28 sources without a listed redshift.[28]

The `LePHARE` code also builds a probability distribution function through the comparison of the observed SED with all the models in the library. This allows us to quantify the uncertainty of the resulting photometric redshift. We finally note that, since they represent a very small fraction (∼4%) of our sample, sources with photometric redshifts were only listed out of completeness and were not used for any study that used the X-ray luminosity.

[28] For one source, SWIFT J1535.8-5749, we did not retrieve enough data to perform SED fitting; therefore, no redshift is available for this object.

3. X-Ray Data and Data Analysis

The spectral analysis was carried out combining the 70-month time-averaged *Swift*/BAT spectra with data obtained by several X-ray facilities: *ASCA* (Section 3.1), *Chandra* (Section 3.2), *Suzaku* (Section 3.3), *Swift*/XRT (Section 3.4), and *XMM-Newton* (Section 3.5). Only two AGNs (SWIFT J1119.5+5132 and SWIFT J1313.6+3650A) were not observed by any X-ray facility in the 0.3–10 keV range, implying a completeness rate of ∼99.8%. The highest energy bin (i.e., 150–195 keV) of the *Swift*/BAT spectrum was not used owing to its poor response, such that it has a signal-to-noise ratio a factor of ∼100–1000 lower than the other seven BAT energy bins (Koss et al. 2013; see top panel of Figure 2 of their paper).

The core of our analysis is the spectral decomposition of all the X-ray data available for the *Swift*/BAT AGNs, to provide measurements of key physical properties related to the X-ray emission, including the intrinsic X-ray luminosity and the column density of matter along the line of sight. Therefore, we first checked the results obtained by fitting the *Swift*/XRT spectrum with a power-law model (see Section 4), visually inspecting the resulting best-fit models and the residuals. We then used X-ray data from *Swift*/XRT for the spectral analysis of unobscured sources, unless (i) we found evidence of ionized absorption or peculiar features or (ii) *Swift*/XRT data had low signal-to-noise ratio or were not available. For these objects we used *XMM-Newton* EPIC/PN data, or if no *XMM-Newton* observation was publicly available, *Suzaku*/X-ray Imaging Spectrometer (XIS), *Chandra*/ACIS, or *ASCA* SIS0/SIS1 and GIS2/GIS3 data were used. For obscured sources we used *XMM-Newton* EPIC/PN, *Suzaku*/XIS, *Chandra*/ACIS, or *ASCA* SIS0/SIS1 and GIS2/GIS3 data. In case none of those were available, we used *Swift*/XRT observations. For blazars we used *Swift*/XRT data, unless none were available. Whenever more than one observation was available, we used the deepest (after accounting for data filtering). We privileged *XMM-Newton* EPIC/PN observations over *Suzaku*/XIS, *Chandra*/ACIS, and *ASCA* SIS0/SIS1 and GIS2/GIS3 because of its larger collecting area in the 0.3–10 keV region, and due to the fact that *XMM-Newton* observed a larger number

Table 2
Log of the Soft X-Ray Observations

(1) Source	(2) Soft X-Ray Facility/Instrument	(3) Obs. ID	(4) Exposure (ks)	(5) Counts
SWIFT J0001.0−0708	*Swift*/XRT	40885001	8.5	815
SWIFT J0001.6−7701	*Swift*/XRT	41138001	9.6	346
SWIFT J0002.5+0323	*Swift*/XRT	47107002	10.8	3035
SWIFT J0003.3+2737	*Swift*/XRT	41139002	9.7	100
SWIFT J0005.0+7021	*XMM-Newton* EPIC/PN	0550450101	14.8	5343
SWIFT J0006.2+2012	*Swift*/XRT	35755001	204.3	56302
SWIFT J0009.4−0037	*Swift*/XRT	41140001	21.0	91
SWIFT J0010.5+1057	*Swift*/XRT	36363001	21.8	5148
SWIFT J0017.1+8134	*XMM-Newton* EPIC/PN	0112620201	19.1	15950
SWIFT J0021.2−1909	*Swift*/XRT	40886001	8.0	1515

Note. Column (1): *Swift*/BAT ID of the source. Column (2): X-ray facility used. Column (3): ID of the observations. Column (4): exposure. Column (5): number of counts.

(This table is available in its entirety in machine-readable form.)

of sources compared to the other satellites. In one case (SWIFT J2234.8-2542) the source was only observed by *BeppoSAX* below 10 keV, and we report the results of the study of Malizia et al. (2000) combined with the analysis of the *Swift*/BAT spectrum.

In the following we briefly describe the X-ray instruments we used, and the procedure we adopted, for the spectral extraction. Details of the soft X-ray observation used for the broadband X-ray spectral analysis of each source are reported in Table 2. Figure 4 shows the distribution of different instruments used for the analysis of the soft X-ray emission of *Swift*/BAT AGNs (see also Table 3).

3.1. ASCA

We used *ASCA* SIS0/SIS1 and GIS2/GIS3 data for three sources. The reduced spectra were obtained from the Tartarus database[29] (Turner et al. 2001), which collects the products obtained for 611 *ASCA* observations of AGNs.

3.2. Chandra

Chandra (Weisskopf et al. 2000) ACIS (Garmire et al. 2003) data were used for 14 sources. The reduction of *Chandra*/ACIS data was performed using CIAO v.4.6 (Fruscione et al. 2006) following the standard procedures. The data were first reprocessed using CHANDRA_REPRO, and the source spectra were then extracted using circular apertures of 10″ radius, centered on the optical counterpart of each source. Background spectra were extracted using circular regions with identical apertures, centered on regions where no other source was present. Both spectra were extracted using the SPECEXTRACT tool. Sources with significant pileup were modeled with the addition of the PILEUP model in XSPEC.

3.3. Suzaku

Suzaku (Mitsuda et al. 2007) XIS (Koyama et al. 2007) data were used to complement *Swift*/BAT spectra for 10 sources. For most of its operating time XIS was composed of three cameras, the front-illuminated (FI) XIS 0 and XIS 3 and the back-illuminated (BI) XIS 1 (hereafter BI-XIS).

For each of the three XIS cameras, we reprocessed the data and extracted the spectra from the cleaned event files using a circular aperture with a radius of 1.′7 centered on the source. The background was taken from a source-free annulus centered at the source peak, with an internal and external radius of 3.′5 and 5.′7, respectively. We generated the ancillary response matrices (ARFs) and the detector response matrices (RMFs) using the XISRMFGEN and XISSIMARFGEN tasks (Ishisaki et al. 2007), respectively. The spectra obtained by XIS 0 and XIS 3 were merged using MATHPHA, ADDRMF, and ADDARF.

Table 3
Summary of the Soft X-Ray Spectra Used

Facility/Instrument	Sources
Swift/XRT	588
XMM-Newton EPIC/PN	220
Chandra/ACIS	14
Suzaku/XIS	10
ASCA GIS/SIS	3
BeppoSAX/MECS	1

3.4. Swift/XRT and BAT

The XRT (Burrows et al. 2005) on board *Swift* followed up nearly all of the sources detected by BAT in the first 70 months of operations. *Swift*/XRT data analysis was performed using the XRTPIPELINE following the standard guidelines (Evans et al. 2009). *Swift*/XRT observations were used for a total of 588 sources.

3.5. XMM-Newton

We used *XMM-Newton* (Jansen et al. 2001) EPIC/PN (Strüder et al. 2001) observations for 220 sources. The original data files were reduced using the *XMM-Newton* Standard Analysis Software version 12.0.1 (Gabriel et al. 2004), and the raw PN data files were then processed using the `epchain` task.

[29] http://heasarc.gsfc.nasa.gov/FTP/asca/data/tartarus/

Table 4
Summary of the Components Included in the Different X-ray Spectral Models

Model	TBABS$_{Gal}$	C_{BAT}	ZPHABS	CABS	ZXIPCF	ZPCFABS	PEXRAV[a]	BB	APEC		Sources
A1	✓	✓	✓	✓	…	…	✓	…	…		101
A2	✓	✓	✓	✓	…	…	✓	✓	…		170
A3	✓	✓	✓	✓	✓	…	✓	…	…		35
A4	✓	✓	✓	✓	✓✓	…	✓	…	…		6
A5	✓	✓	✓	✓	✓	…	✓	✓	…		33
A6	✓	✓	✓	✓	✓✓	…	✓	✓	…		5
A7	✓	✓	✓	✓	…	…	✓	…	✓✓		1
A8	✓	✓	✓	✓	✓	✓	✓	✓	…		1
Model	TBABS$_{Gal}$	C_{BAT}	ZPHABS	CABS	ZXIPCF	ZPCFABS	CUTOFFPL	PEXRAV[b]	APEC	SCATT	
B1	✓	✓	✓	✓	…	…	✓	✓	…	✓	272
B2	✓	✓	✓	✓	…	…	✓	✓	✓	✓	87
B3	✓	✓	✓	✓	…	…	✓	✓	✓✓	✓	19
B4	✓	✓	✓	✓	…	…	✓	✓	✓✓✓	✓	1
B5	✓	✓	✓	✓	✓	…	✓	✓	✓	✓	1
B6	✓	✓	✓	✓	…	✓✓	…	✓[a]	…	…	3
B7	✓	✓	✓	✓	…	…	✓	✓	✓✓[c]	✓	1
B8	✓	✓	✓	✓	…	…	✓	✓	✓[c] ✓[c]	✓	1
B9	✓	✓	✓	✓	…	…	✓	✓	✓✓	…	1
Model	TBABS$_{Gal}$	C_{BAT}	ZPHABS	CABS	ZXIPCF	POW	BKN	BKN2	BB	SCATT	
C1	✓	✓	✓	✓	…	✓	…	…	…	…	52
C2	✓	✓	✓	✓	…	✓	…	…	✓	…	10
C3	✓	✓	✓	✓	✓	✓	…	…	…	…	3
C4	✓	✓	✓	✓	✓✓	✓	…	…	…	…	2
C5	✓	✓	✓	✓	…	✓	…	…	…	✓	6
C6	✓	✓	✓	✓	…	…	✓	…	…	…	23
C7	✓	✓	✓	✓	…	…	…	✓	✓	…	1

Notes. The table lists the different components that were used by the models and the number of sources for which each model was adopted. When more than one check mark is reported, the component was used more than once. SCATT is the scattered component (f_{scat} × CUTOFFPL in XSPEC), while C_{BAT} is the cross-calibration constant (CONS in XSPEC). Details about the spectral components can be found in Section 4.1, while the accurate syntax used in XSPEC is reported in Sections 4.2.1–4.2.3.

[a] The reflection parameter was set to be $R \geqslant 0$, i.e., the component takes into account the primary X-ray emission (in the form of a cutoff power-law) and reprocessed radiation at the same time.

[b] The reflection parameter was set to be negative, i.e., the reflection component is disconnected from the primary X-ray emission and assumed to be unobscured.

[c] Absorption by neutral material was considered for the thermal component.

For every observation, we inspected the background light curve in the 10–12 keV energy band, in order to filter the exposures for periods of high-background activity. Only patterns corresponding to single and double events (PATTERN $\leqslant$4) were selected. We extracted the source spectra from the final filtered event list using circular apertures centered on the object, with a typical radius of 20″. Regions with smaller radii were used for the sources detected with a low signal-to-noise ratio. The background was extracted from circular regions of 40″ radius, located on the same CCD as the source, where no other X-ray source was detected. We checked for the presence of pileup using the EPATPLOT task. For observations with significant pileup we used an annular region with an inner radius set such that no pileup was present. Finally, we created ARFs and RMFs using the ARFGEN and RMFGEN tasks, respectively.

4. X-Ray Spectral Analysis

The X-ray spectral analysis was carried out using XSPEC v.12.7.1b (Arnaud 1996). For all models reported in what follows, we took into account Galactic absorption in the direction of the source, by adding photoelectric absorption (i.e., using the TBABS component in XSPEC; Wilms et al. 2000), fixed to the value from the H I maps of Kalberla et al. (2005), assuming solar metallicity. The combined X-ray spectra were then analyzed using a series of models of successive complexity, which are listed in Table 4. First, all sources were fitted using a simple power-law model (TBABS$_{Gal}$·(ZPOW) in XSPEC), and the residuals were then visually inspected to assess whether the X-ray spectrum showed signatures of neutral or ionized absorption. A cross-calibration constant (C_{BAT}) was added to all models to take into account possible variability between the 70-month averaged *Swift*/BAT spectra and the considerably shorter soft X-ray observations, as well as cross-calibration uncertainties. It should be remarked that this factor does not take into account possible spectral variability between the hard and soft X-ray spectra, which might accompany flux variability.

Sources were divided into two main categories depending on their BZCAT classification: nonblazar AGNs (Sections 4.2.1 and 4.2.2) and blazars (Section 4.2.3). The spectra of eight sources originally classified as blazars show signatures of reprocessed X-ray emission, or are heavily contaminated by other components, and were therefore fitted using nonblazar

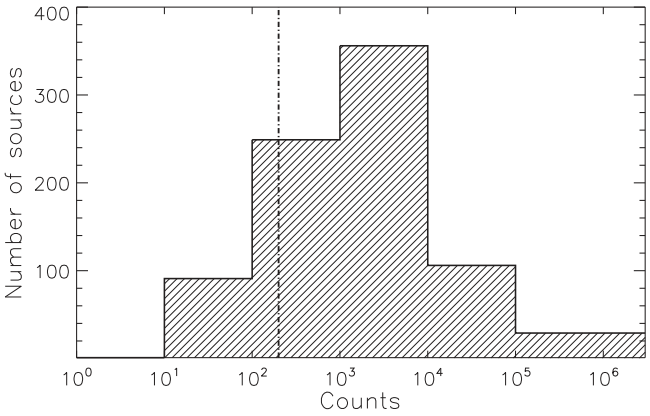

Figure 5. Distribution of the $\leqslant$10 keV counts for the AGNs of our sample with soft X-ray observations available. The vertical dot-dashed line shows the threshold used to separate objects fitted with Cash ($<$200 counts) and χ^2 ($\geqslant$200 counts) statistics (see Section 4 for details). The counts from different instruments were summed for observations carried out but *Suzaku*/XIS and *ASCA* GIS/SIS. The median of the number of counts of our sample is $\sim$1600.

models. These sources are 3C 120 (Kataoka et al. 2007), 3C 273 (Haardt et al. 1998; Soldi et al. 2008), Cen A (Evans et al. 2004), Mrk 348 (Marchese et al. 2014), NGC 1052 (Brenneman et al. 2009), and NGC 7213 (Bianchi et al. 2008b). Besides these sources, the X-ray spectrum of Mrk 1501 also shows evidence of reprocessed X-ray radiation, in the form of an Fe Kα feature. NGC 1275 was also fitted using a different model, since its X-ray spectrum shows peculiar features owing to the fact that the source is located at the center of the Perseus cluster. Nonblazar AGNs were then further divided, based on the initial power-law fit, into two categories: those showing relatively weak intrinsic absorption from neutral material (Section 4.2.1) and those showing clear signatures of obscuration (Section 4.2.2). Different sets of models were used for sources in different categories. In all cases we started with the simplest models, and after visual inspection of the residuals, we increased their complexity, adding components if the fit was significantly improved.

We used χ^2 statistics to fit the soft X-ray spectra when the number of counts was $\geq$200, and Cash statistics (C-stat; Cash 1979) when it was below 200. For the 692 sources for which more than 200 source counts were available, we rebinned the spectral data to have 20 counts per bin and used χ^2 statistics. For the remaining 144 objects we rebinned the soft X-ray spectra to have one count per bin and adopted Cash statistics, while we still used χ^2 statistics for the *Swift*/BAT spectra. The median number of counts across the entire sample is 1600. Figure 5 presents the distribution of counts below 10 keV. Fits were considered to be significantly improved by the addition of a component if $\Delta\chi^2 > 2.71$ (or ΔC-stat$^2 > 2.71$) for each extra free parameter.

In the next sections, we report in detail the spectral components (Section 4.1) and the models (Sections 4.2.1–4.2.3) we used for the broadband X-ray spectral fitting. The histograms showing the number of times each best-fit model was used are illustrated in Figure 6 for unobscured AGNs (top panel), obscured AGNs (middle panel), and blazars (bottom panel). The main spectral parameters obtained by the broadband X-ray spectral fitting are reported in Table 5. In the top panel of Figure 7 we show the values of the χ^2/C-stat obtained with the best-fit model versus the number of degrees of freedom (dof) for the sources in our sample, while in the

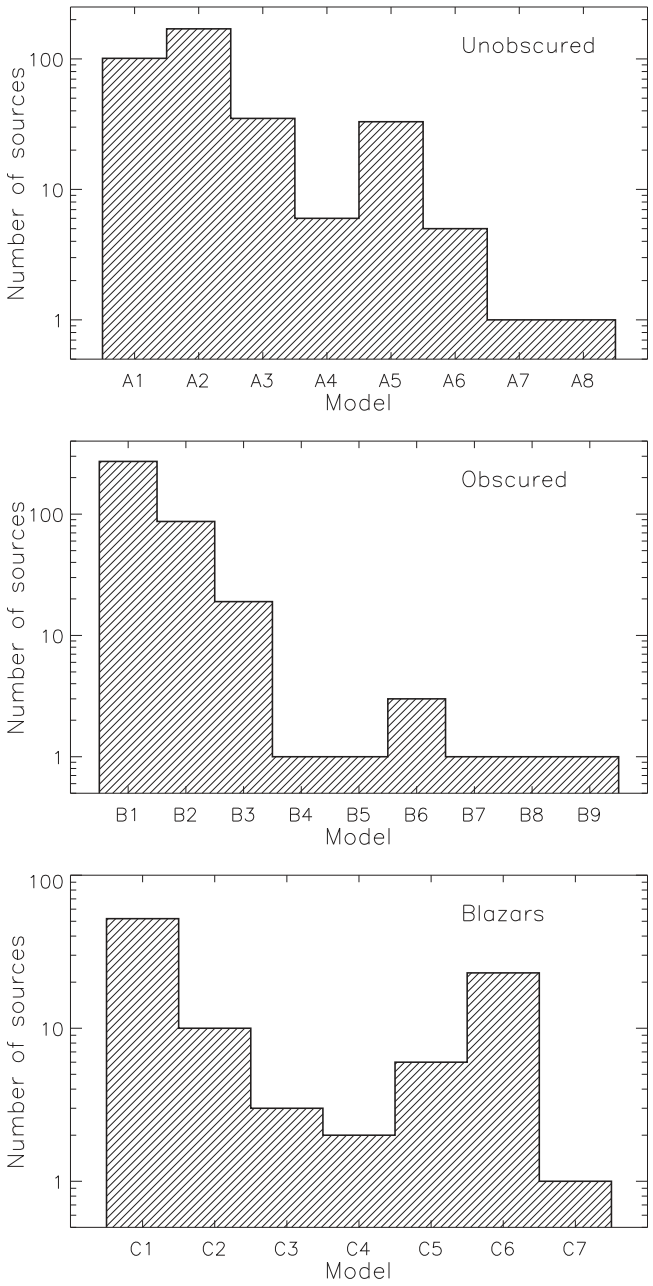

Figure 6. Distribution of the different X-ray spectral models used for unobscured AGNs (top panel; see Section 4.2.1 for details), obscured AGNs (middle panel; Section 4.2.2), and blazars (bottom panel; Section 4.2.3). Overall 26 spectral models were used to fit the broadband X-ray spectra of the AGNs in the 70-month *Swift*/BAT catalog. The different components used in the models are listed in Table 4, and the models are illustrated in Figures 8–11 (with the exception of models D1 and D2; see Section 4.2.4).

bottom panel we show the ratio between χ^2 (or C-stat) and the dof versus the number of counts. The median value of the ratio between χ^2 and the dof is 0.996 ± 0.008, confirming the satisfactory quality of the spectral fitting.

4.1. Model Components

In the following we describe the different components used for the X-ray spectral fitting and the free parameters of each model.

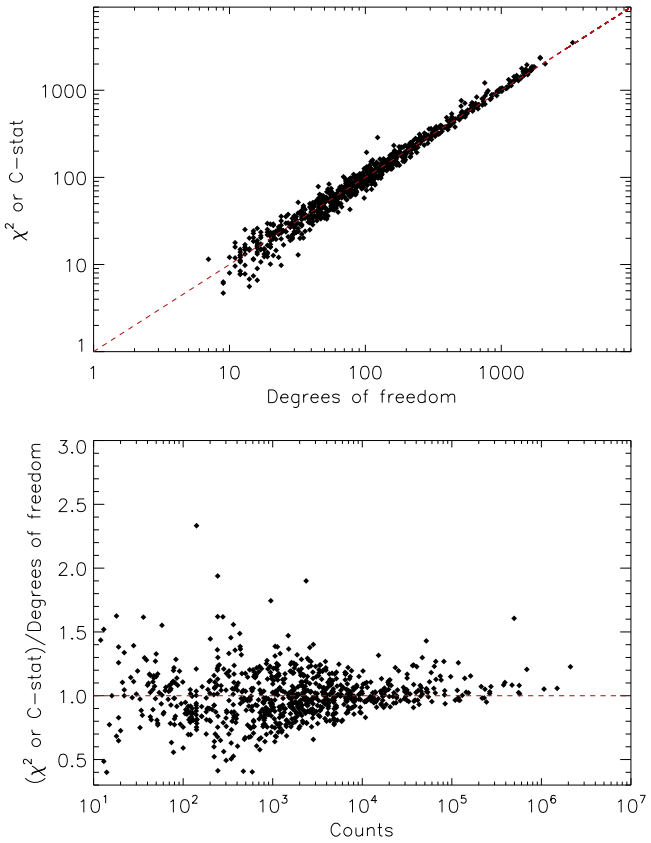

Figure 7. Top panel: values of the χ^2 and the C-stat obtained by fitting the whole sample of AGNs vs. the dof. Bottom panel: ratio between χ^2 (or C-stat) and the dof vs. the number of counts. In both panels the red dashed line represents $\chi^2/\mathrm{dof} = 1$ or C-Stat/dof = 1.

4.1.1. X-Ray Continuum

For the X-ray continuum of the nonblazar AGNs we used a power-law component with a high-energy cutoff (CUTOFFPL in XSPEC). The free parameters of this model are the photon index (Γ), the energy of the cutoff (E_C), and the normalization (no_{cut}). To take into account reprocessing of the primary X-ray continuum by circumnuclear material, we used the PEXRAV model (Magdziarz & Zdziarski 1995), which assumes reflection by a semi-infinite slab. The inclination angle i was fixed to 30° for all objects, in order to have a value of the reflection parameter ($R = \Omega/2\pi$, where Ω is the covering factor of the reflecting material) independent of any assumption on the geometry of obscured and unobscured AGNs. The metallicity was fixed to solar, and thus the sole free parameter of this model is R. For blazars we used a simple power-law model (POW) or, when required by the fit, a broken (BKN) or a double broken (BKN2) power law. For the power-law model the free parameters are the photon index (Γ) and the normalization (no_{pow}). The broken power-law model considers a continuum that changes its slope at an energy E_{brk}. The two different photon indices are Γ_1 and Γ_2 for $E < E_{brk}$ and $E > E_{brk}$, respectively. The free parameters of this model are E_{brk}, Γ_1, Γ_2, and the normalization (no_{bkn}). In the double broken power-law model the continuum changes slope twice: at E^1_{brk} and E^2_{brk}. The photon indices are Γ_1, Γ_2, and Γ_3 for $E < E^1_{brk}$, $E^1_{brk} \leqslant E < E^2_{brk}$, and $E \geqslant E^2_{brk}$, respectively. The free parameters are E^1_{brk}, E^2_{brk}, Γ_1, Γ_2, Γ_3, and the normalization (no_{bkn2}). No reflection component was considered for blazars, since most of the X-ray emission arises from the jets, which washes out any signature of reprocessed radiation. In Table 5 we report the values of Γ_1 for the blazars for which a broken power-law continuum was used, while the values of Γ_2, Γ_3, E^1_{brk}, and E^2_{brk} are reported in Table 6.

4.1.2. Absorption

Absorption of the X-ray radiation by neutral material occurs as a result of the combined effect of photoelectric absorption and Compton scattering. Photoelectric absorption was taken into account using the ZPHABS model, with the redshift fixed to the systemic redshift of each source. Compton scattering was considered using the CABS model. The only free parameter for these two models is the column density, which was tied to have the same value in all fits (i.e., $N_H(\mathrm{CABS}) = N_H(\mathrm{ZPHABS}) = N_H$). Whenever the column density could not be constrained because the source was completely unobscured, it was fixed to $N_H/\mathrm{cm}^{-2} = 0$. The redshift was fixed to $z = 0$ for the sources for which no spectroscopic redshift was available. When required by the data, we used a partial covering neutral absorber model ZPCFABS, whose free parameters are N_H and the covering fraction (f_{cov}). The values of N_H from the best-fit models are listed in Table 5.

Absorption by ionized gas (also referred to as "warm absorption") was taken into account using the ZXIPCF model (Reeves et al. 2008), which uses a grid of XSTAR absorption models (Bautista & Kallman 2001; Kallman & Bautista 2001). The free parameters of this model are the column density (N_H^W), the ionization parameter (ξ), and the covering factor (f_{cov}^W) of the warm absorber. The ionization parameter is defined as $\xi = L_{ion}/nr^2$, where n is the density of the absorber, L_{ion} is the ionizing luminosity of the source in the range 5 eV–300 keV, and r is the distance between the ionizing source and the absorbing material. The values of N_H^W, ξ, and f_{cov}^W obtained by our spectral analysis are listed in Table 7.

4.1.3. Soft Excess

An excess over the X-ray primary emission below ~1–2 keV (the "soft excess") has been found in both obscured and unobscured sources, although it is widely believed to have a very different physical origin in the two cases. For unobscured objects the soft excess might be due to any of three potential mechanisms: (i) blurred relativistic reflection (e.g., Crummy et al. 2006; Fabian et al. 2009; Vasudevan et al. 2014), (ii) Comptonization of the seed optical/UV photons in plasma colder than that responsible for the primary X-ray component (e.g., Mehdipour et al. 2011; Done et al. 2012; Boissay et al. 2014, 2016), or (iii) smeared absorption by ionized material (e.g., Gierliński & Done 2004). For obscured objects this feature could have one or several of the following origins: (i) emission from a thermal plasma possibly related to star formation (e.g., Iwasawa et al. 2011), (ii) radiative-recombination continuum created by gas photoionized by the AGN (e.g., Bianchi et al. 2006; Guainazzi & Bianchi 2007), or (iii) scattering of the primary X-ray emission in Compton-thin circumnuclear material (e.g., Ueda et al. 2007).

Given the different physical origin, we adopted different models to reproduce the soft excess in unobscured and obscured AGNs. For unobscured sources we used a blackbody component (BBODY), with the free parameters being the temperature (kT_{bb}) and the normalization. This is not a physical

Table 5
Parameters Obtained by the Analysis of the Broadband X-Ray Spectra

(1) Source	(2) $\log N_{\rm H}$ ($\rm cm^{-2}$)	(3) Γ	(4) E_c (keV)	(5) R	(6) $C_{\rm BAT}$	(7) $f_{\rm scatt}$ (%)	(8) kT (keV)	(9) Model	(10) Statistic/dof
SWIFT J0001.0−0708	22.19 [22.11–22.26]	$1.64^{+0.60}_{-0.18}$	$\geqslant 29$	$\leqslant 1.7$	$0.8^{+0.6}_{-0.3}$	$\leqslant 1.1$	⋯	B1	34.7/40 [χ^2]
SWIFT J0001.6−7701	⋯	$1.83^{+0.57}_{-0.37}$	$\geqslant 47$	$\leqslant 1.3$	$1.0^{+0.4}_{-0.8}$	⋯	⋯	A3	14.8/17 [χ^2]
SWIFT J0002.5+0323	⋯	$2.23^{+0.06}_{-0.06}$	NC	$4.2^{+3.0}_{-0.7}$	$0.5^{+0.5}_{-0.2}$	⋯	⋯	A1	131.5/120 [χ^2]
SWIFT J0003.3+2737	22.86 [22.78–22.98]	$1.76^{+0.28}_{-0.40}$	NC	$1.1^{+2.2}_{-1.0}$	1.0[a]	$\leqslant 0.7$	⋯	B1	83.7/111 [C]
SWIFT J0005.0+7021	22.61 [22.56–22.68]	$1.46^{+0.29}_{-0.20}$	47^{+47}_{-20}	$\leqslant 2.4$	1.0[a]	$\leqslant 0.7$	⋯	B1(G)	243.3/241 [χ^2]
SWIFT J0006.2+2012	20.48 [20.26–20.51]	$2.82^{+0.08}_{-0.03}$	$\geqslant 185$	$0.8^{+1.0}_{-0.4}$	$3.7^{+1.4}_{-0.6}$	⋯	$0.149^{+0.002}_{-0.008}$	A6(G)	571.1/515 [χ^2]
SWIFT J0009.4−0037	23.61 [23.36–24.04]	$1.64^{+0.48}_{-0.87}$	NC	$0.8^{+1.7}_{-0.4}$	1.0[a]	$1.0^{+3.6}_{-0.9}$	⋯	B1(G)	99.0/83 [C]
SWIFT J0010.5+1057	21.04 [21.00–21.11]	$1.73^{+0.03}_{-0.07}$	$\geqslant 269$	$0.6^{+0.2}_{-0.2}$	$1.1^{+0.2}_{-0.2}$	⋯	$0.122^{+0.007}_{-0.007}$	A2(G)	232.1/196 [χ^2]
SWIFT J0017.1+8134	21.95 [21.85–22.04]	$1.52^{+0.02}_{-0.02}$	⋯	⋯	$2.3^{+2.2}_{-1.2}$	⋯	⋯	C6	585.1/565 [χ^2]
SWIFT J0021.2−1909	21.98 [21.92–22.08]	$1.70^{+0.22}_{-0.13}$	86^{+211}_{-44}	$\leqslant 0.2$	$0.7^{+0.1}_{-0.3}$	$2.0^{+1.2}_{-1.2}$	⋯	B1	72.0/71 [χ^2]

Notes. Column (1): *Swift*/BAT ID of the source. Column (2): value of the logarithm of the column density and the 90% confidence interval. Column (3): photon index. Column (4): energy of the cutoff. Column (5): reflection parameter. Column (6): cross-calibration between *Swift*/BAT and the soft X-ray spectra. Column (7): fraction of scattered emission observed in the soft X-ray band. Column (8): temperature of the blackbody component (for unobscured objects) or of the thermal plasma component (for obscured objects). Column (9): model used (G is reported when a Gaussian line around ∼6–7 keV was added; see Section 4 for details). Column (10): value of the statistic and the number of degrees of freedom. Objects for which no column density was reported have $\log(N_{\rm H}/{\rm cm^{-2}}) \lesssim 20$. NC—value not constrained. *—value fixed.
[a] The value of $C_{\rm BAT}$ was not constrained so that the constant was fixed to 1.
(This table is available in its entirety in machine-readable form.)

Table 6
Parameters of the Broken Power-law Continuum

(1) Source	(2) Γ_2	(3) $E_{\rm brk}$ (keV)
SWIFT J0017.1+8134	$2.6^{+0.7}_{-0.5}$	13^{+31}_{-10}
SWIFT J0036.0+5951	$2.96^{+0.13}_{-0.11}$	7^{+1}_{-1}
SWIFT J0122.0−2818	$-2.2^{+0.4}_{-0.2}$	88^{+27}_{-16}
SWIFT J0122.9+3420	$2.52^{+0.51}_{-0.40}$	17^{+8}_{-15}
SWIFT J0142.0+3922	$1.74^{+0.09}_{-0.08}$	$2.5^{+0.6}_{-0.5}$
SWIFT J0225.0+1847	$1.71^{+0.20}_{-0.16}$	$7.5^{+1.4}_{-0.4}$
SWIFT J0404.0−3604	$1.95^{+0.14}_{-0.09}$	$3.9^{+1.4}_{-0.8}$
SWIFT J0550.7−3212A	$3.58^{+1.35}_{-0.66}$	$18.8^{+2.0}_{-2.5}$
SWIFT J0710.3+5908	$2.85^{+1.37}_{-0.57}$	32^{+10}_{-9}
SWIFT J0841.4+7052	$1.63^{+0.02}_{-0.02}$	$3.7^{+0.6}_{-0.5}$

Note. Column (1): *Swift*/BAT ID of the source. Column (2): second photon index. Column (3): energy of the break between Γ_1 and Γ_2. For SWIFT J1256.2−0551 two sets of values are reported since the source was fitted using model C7, which considers a double broken power law. For this object the second line reports the value of Γ_3 and $E^2_{\rm brk}$.
(This table is available in its entirety in machine-readable form.)

Table 7
Parameters of the Warm Absorbers

(1) Source	(2) $N_{\rm H}^{\rm W}$ (10^{22} $\rm cm^{-2}$)	(3) $\log \xi$ (erg cm $\rm s^{-1}$)	(4) $f_{\rm cov}^{\rm W}$ (%)
SWIFT J0001.6−7701	10^{+5}_{-3}	$1.4^{+0.6}_{-0.1}$	96^{+2}_{-3}
SWIFT J0006.2+2012	$2.91^{+0.06}_{-0.04}$	$0.42^{+0.02}_{-0.02}$	95^{+2}_{-1}
SWIFT J0006.2+2012	52^{+8}_{-9}	$3.18^{+0.06}_{-0.13}$	80^{+7}_{-9}
SWIFT J0113.8−1450	$0.44^{+0.18}_{-0.16}$	$0.4^{+0.4}_{-0.5}$	49^{+3}_{-6}
SWIFT J0154.9−2707	3^{+5}_{-2}	$\leqslant 1.6$	74^{+6}_{-4}
SWIFT J0207.0+2931	$0.39^{+0.07}_{-0.06}$	$0.44^{+0.15}_{-0.23}$	71^{+8}_{-10}
SWIFT J0207.0+2931	$0.79^{+0.33}_{-0.16}$	$2.41^{+0.15}_{-0.14}$	$\geqslant 84$
SWIFT J0208.5−1738	5^{+9}_{-2}	$1.3^{+0.9}_{-1.5}$	58^{+14}_{-21}
SWIFT J0222.3+2509	$0.5^{+1.3}_{-0.2}$	$\leqslant 1.5$	68^{+10}_{-18}
SWIFT J0226.4−2821	$2.8^{+1.7}_{-1.1}$	$0.9^{+0.3}_{-0.3}$	$\geqslant 97$

Note. Column (1): *Swift*/BAT ID of the source. Column (2): column density. Column (3): ionization parameter. Column (4): covering fraction of the ionized absorber. Sources reported more than once were fitted considering more than one layer of ionized absorbing material.
(This table is available in its entirety in machine-readable form.)

model, and it provides only a phenomenological representation of this feature; given the uncertain origin of the soft excess, we deem this to be the best approach. For obscured AGNs a second cutoff power-law component was added to the model, with the values of the photon index, the cutoff energy, and the normalizations fixed to those of the primary X-ray emission. A multiplicative constant ($f_{\rm scatt}$), of typically a few percent of the primary X-ray emission (Section 5.4.2), was added to this second cutoff power law to renormalize the flux, as a free parameter. For obscured sources we also added, when necessary, a collisionally ionized plasma (APEC). The free parameters of the APEC model are the temperature ($kT_{\rm therm.}$) and the normalization. It should be noted that an unobscured scattered component could also be due to a partially covering absorber, in particular for values of $f_{\rm scatt} \geqslant 5\%$–$10\%$.

4.1.4. Fe Kα Emission Lines

The fluorescent iron Kα emission line has been observed almost ubiquitously in the X-ray spectra of AGNs (e.g., Mushotzky et al. 1993; Shu et al. 2010) and is composed of a narrow (e.g., Shu et al. 2011; Iwasawa et al. 2012; Ricci et al. 2013a, 2013b, 2014b) and a broad (e.g., Mushotzky et al. 1995; Nandra et al. 1997; Patrick et al. 2012) component. The narrow Fe Kα line could originate in the molecular torus (e.g., Nandra 2006; Ricci et al. 2014a), in the broad-line region (e.g., Bianchi et al. 2008b), in an intermediate region between these two

(Gandhi et al. 2015), and from very extended (>10–100 pc) material (e.g., Young et al. 2001; Arévalo et al. 2014; Bauer et al. 2015).

The broad component is likely to be due to relativistic reflection from the innermost region of the accretion flow (e.g., Fabian et al. 2000; Brenneman & Reynolds 2009; Reynolds 2014), although at least for some objects it might be due to the distortion of the X-ray continuum created by highly ionized absorbing material along the line of sight (e.g., Turner & Miller 2009, and references therein).

In this work we do *not* attempt to reproduce the broad Fe Kα emission line in the *Swift*/BAT AGNs under study, and we limit our analysis to the more prominent and more common narrow component. This was done by adding a Gaussian emission line profile (ZGAUSS in XSPEC) to all high-quality spectra (i.e., *XMM-Newton* EPIC/PN, *Chandra*, *Suzaku*/XIS) unless the line could not be constrained. A Gaussian line was also taken into account for *Swift*/XRT spectra if residuals at ~6.4 keV were found fitting the continuum. The parameters of this component are the peak energy, the width (σ), and the normalization ($n_{\rm Gauss}$) of the line. The energy of the line was fixed to 6.4 keV if it could not be constrained, while the width was fixed to 10 eV (i.e., lower than the energy resolution of the X-ray instruments we used) if the line was not resolved. The values of the energy, equivalent width (EW), width, and normalization of the lines obtained are listed in Table 8. The properties of the Fe Kα line and its relation with the physical characteristics of the accreting SMBH will be discussed in detail in a forthcoming publication.

4.2. Spectral Models

In the following we list the different models that we adopted for the X-ray spectral fitting of our sources. In Table 4 we summarize the different spectral models, while in Figures 8–11 we illustrate the models we used, highlighting the different components. In Figure 12 we show, as an example of the typical fitting quality, four broadband X-ray spectra of different types of AGNs (unobscured, obscured, blazar, and CT).

4.2.1. Unobscured Sources

A total of 352 AGNs were fitted using this set of models (i.e., models A1 to A8; top panel of Figure 6).

Model A1:

$\rm TBABS_{Gal} \times C_{BAT} \times$ ZPHABS $\times$ CABS $\times$ PEXRAV.

This model includes primary X-ray emission and reflection, both of them obscured by the same column density. Used for 101 AGNs.

Model A2:

$\rm TBABS_{Gal} \times C_{BAT} \times$ ZPHABS $\times$ CABS $\times$ (PEXRAV + BB).

This model is the same as model A1, with the addition of a blackbody component to take into account the presence of a soft excess below 1 keV. Used for 170 sources.

Model A3:

$\rm TBABS_{Gal} \times C_{BAT} \times \times$ ZPHABS $\times$ CABS $\times$ ZXIPCF $\times$ PEXRAV.

Same as model A1, plus a layer of partially covering ionized material. Used for 35 AGNs.

Model A4:

$\rm TBABS_{Gal} \times C_{BAT} \times$ ZPHABS $\times$ CABS $\times$ ZXIPCF $\times$ ZXIPCF $\times$ PEXRAV.

Same as model A3, plus another layer of partially covering ionized material. Used for six objects.

Model A5:

$\rm TBABS_{Gal} \times C_{BAT} \times$ ZPHABS $\times$ CABS $\times$ ZXIPCF $\times$ (PEXRAV + BB).

Same as model A2, plus a partially covering ionized absorber. Used for 33 X-ray spectra.

Model A6:

$\rm TBABS_{Gal} \times C_{BAT} \times$ ZPHABS $\times$ CABS $\times$ ZXIPCF $\times$ ZXIPCF $\times$ (PEXRAV + BB).

Same as model A5, plus another partially covering ionized absorber. Used for five sources.

Model A7:

$\rm TBABS_{Gal} \times C_{BAT} \times$ (ZPHABS $\times$ CABS $\times$ PEXRAV + APEC + APEC).

This model was used only for SWIFT J0955.5+6907 (M81) and adds emission from two components of collisionally ionized plasma to model A1. These two components, with different temperatures, are included to take into account the emission from hot gas, possibly associated with star formation and point sources (Page et al. 2003).

Model A8:

$\rm TBABS_{Gal} \times C_{BAT} \times$ ZPCFABS $\times$ ZXIPCF $\times$ CABS $\times$ (PEXRAV + BB).

This model was used only for SWIFT J1210.5+3924 (NGC 4151) and adds a partially covering neutral absorber to model A5. These two components, with different temperatures, are added to take into account the emission from hot gas, possibly associated with star formation and point sources (Page et al. 2003).

4.2.2. Obscured Sources

A total of 386 objects were fitted using this set of models (i.e., models B1 to B9; middle panel of Figure 6). For obscured sources we separated the primary X-ray emission from the reflection in order to leave the latter unobscured. Reprocessed X-ray radiation was taken into account by tying the values of the normalization of the power law and of the cutoff energy to those of the primary X-ray emission, while leaving the reflection component free to vary. The value of R was set to have only negative values, in order to consider only X-ray reflection in the model. For the sources for which reprocessed radiation and primary X-ray emission were decomposed, the cross-calibration constant was added only to the primary X-ray emission. This reflects a scenario in which most of the X-ray variability is due to the obscured primary X-ray continuum, while unobscured reflected radiation, produced in the torus and/or in the BLR, does not vary significantly on the timescales probed here (e.g., Arévalo et al. 2014).

Model B1:

$\rm TBABS_{Gal} \times (C_{BAT} \times$ ZPHABS $\times$ CABS $\times$ CUTOFFPL + PEXRAV + $f_{\rm scatt} \times$ CUTOFFPL).

This model considers an absorbed primary X-ray emission, an unobscured reflection component, and a scattered component. Used for 272 sources.

Model B2:

$\rm TBABS_{Gal} \times (C_{BAT} \times$ ZPHABS $\times$ CABS $\times$ CUTOFFPL + PEXRAV + $f_{\rm scatt} \times$ CUTOFFPL + APEC).

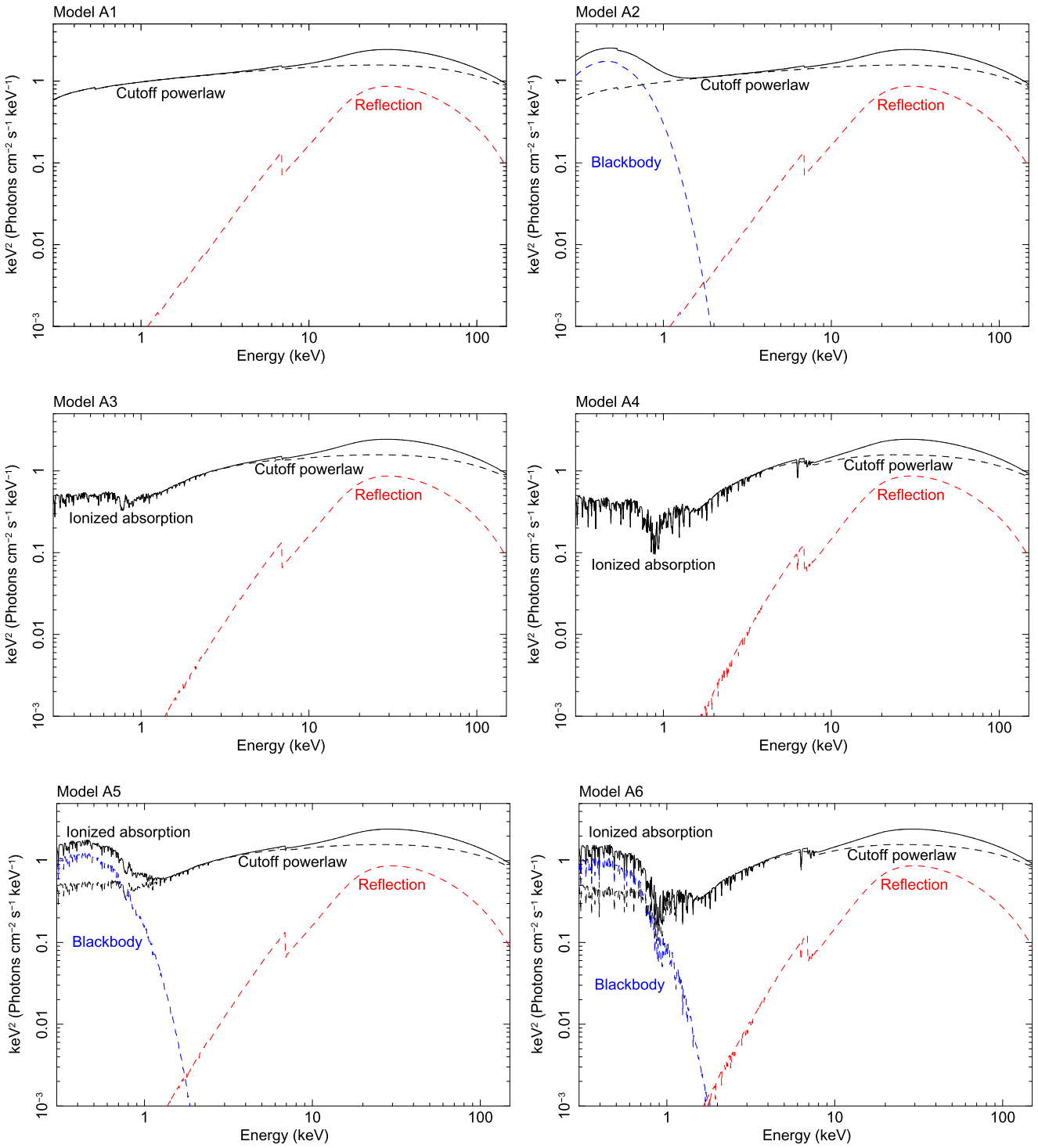

Figure 8. Models used for the X-ray spectral analysis (A1 to A6). In the models A1 to A6 the reflection and primary components were decoupled in PEXRAV for the purpose of visual clarity. See Table 4 and Section 4.2 for details.

Same as model B1, plus a collisionally ionized plasma component. Used for 87 AGNs.

Model B3:

$\mathrm{TBABS_{Gal}} \times (C_{\mathrm{BAT}} \times \mathrm{ZPHABS} \times \mathrm{CABS} \times \mathrm{CUTOFFPL} + \mathrm{PEXRAV} + f_{\mathrm{scatt}} \times \mathrm{CUTOFFPL} + \mathrm{APEC} + \mathrm{APEC})$.

Same as model B2, plus a second collisionally ionized plasma. Used for 19 objects.

Model B4:

$\mathrm{TBABS_{Gal}} \times (C_{\mathrm{BAT}} \times \mathrm{ZPHABS} \times \mathrm{CABS} \times \mathrm{CUTOFFPL} + \mathrm{PEXRAV} + f_{\mathrm{scatt}} \times \mathrm{CUTOFFPL} + \mathrm{APEC} + \mathrm{APEC} + \mathrm{APEC})$.

Same as model B3, plus a third collisionally ionized plasma. Used only for SWIFT J1322.2−1641 (MCG −03−34−064).

Model B5:

$\mathrm{TBABS_{Gal}} \times (C_{\mathrm{BAT}} \times \mathrm{ZPHABS} \times \mathrm{CABS} \times \mathrm{ZXIPCF} \times \mathrm{CUTOFFPL} + \mathrm{PEXRAV} + f_{\mathrm{scatt}} \times \mathrm{CUTOFFPL} + \mathrm{APEC})$.

Same as model B2, plus a partially covering ionized absorber. Used only for SWIFT J0333.6−3607 (NGC 1365).

Model B6:

$\mathrm{TBABS_{Gal}} \times (C_{\mathrm{BAT}} \times \mathrm{ZPCFABS} \times \mathrm{ZPCFABS} \times \mathrm{CABS} \times \mathrm{PEXRAV})$.

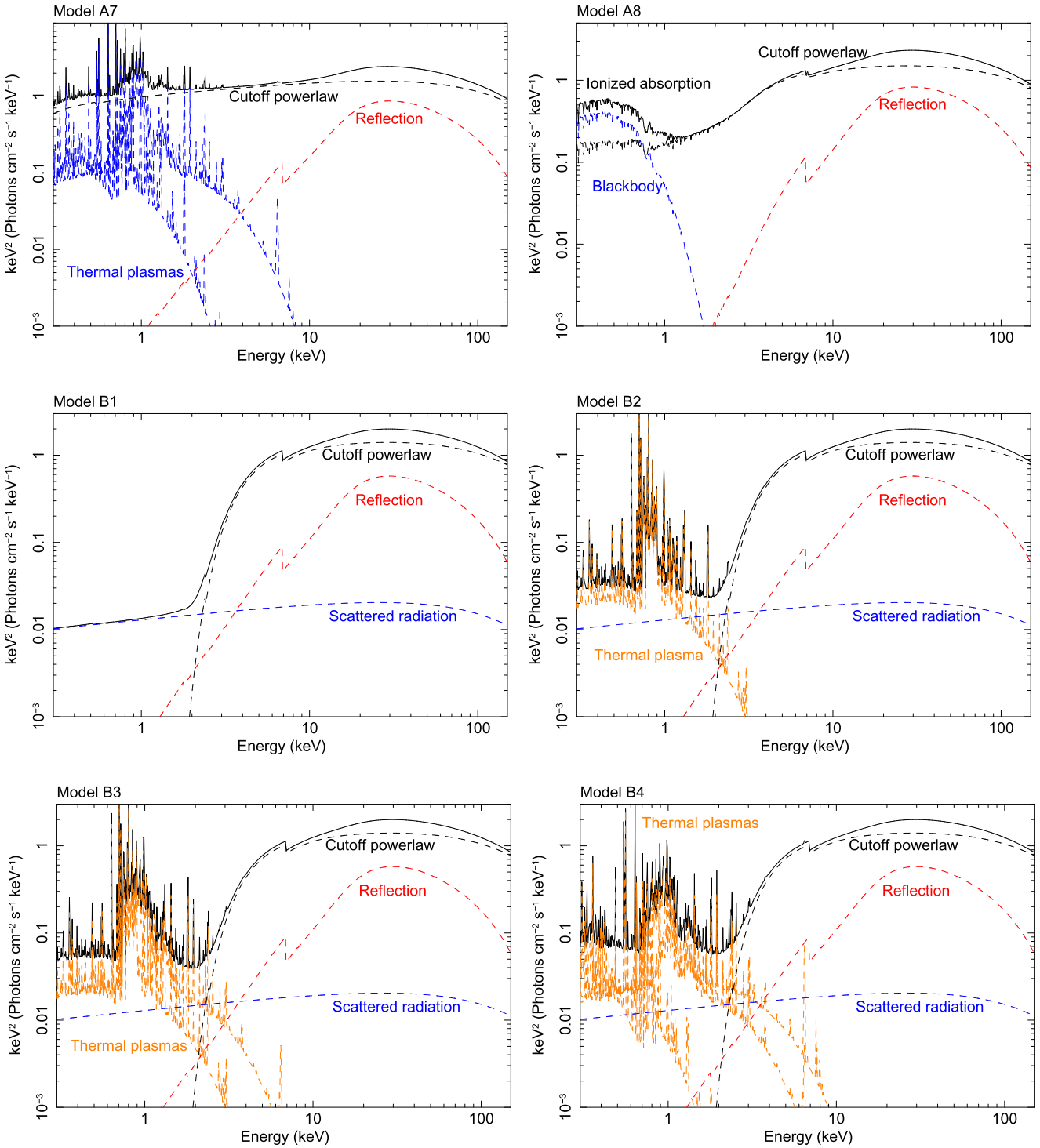

Figure 9. Models used for the X-ray spectral analysis (A7 to B4). In models A7 and A8 the reflection and primary components were decoupled in PEXRAV for the purpose of visual clarity. See Table 4 and Section 4.2 for details.

Considers a double partially covering absorber instead of fully covering material. This model was used only for SWIFT J0552.2−0727 (NGC 2110), SWIFT J2124.6+5057 (4C 50.55), and SWIFT J2223.9−0207 (3C 445). For the latter also a thermal plasma was added to the model. The column density of the CABS term was fixed to the sum of the values of $N_{\rm H}$ of the two partially covering absorbers, weighted over their covering factor.

Model B7:

$\mathrm{TBABS_{Gal}} \times (C_{\rm BAT} \times \mathrm{ZPHABS} \times \mathrm{CABS} \times \mathrm{CUTOFFPL} + \mathrm{PEXRAV} + f_{\rm scatt} \times \mathrm{CUTOFFPL} + \mathrm{ZPHABS} \times \mathrm{APEC} + \mathrm{APEC})$.

Same as model B3, plus neutral absorption for one of the two collisionally ionized plasma models. Used only for SWIFT J1206.2+5243 (NGC 4102).

Model B8:

$\mathrm{TBABS_{Gal}} \times (C_{\rm BAT} \times \mathrm{ZPHABS} \times \mathit{cabs} \times \mathrm{CUTOFFPL} + \mathrm{PEXRAV} + f_{\rm scatt} \times \mathrm{CUTOFFPL} + \mathrm{ZPHABS} \times \mathrm{APEC} + \mathrm{ZPHABS} \times \mathrm{APEC})$.

Same as model B3, plus two neutral absorption components, one for each of the collisionally ionized plasma components. Used only for SWIFT J1652.9+0223 (NGC 6240).

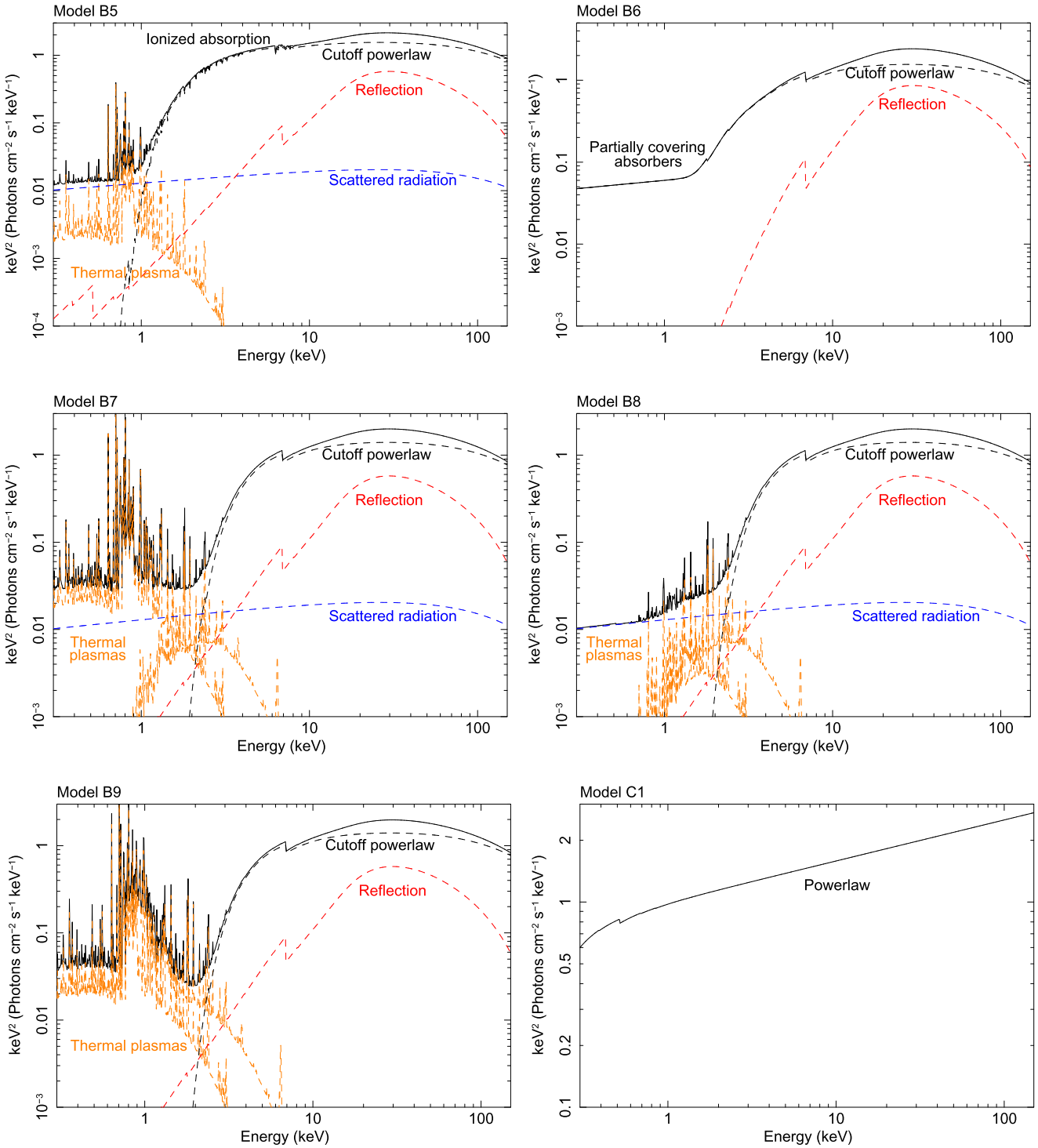

Figure 10. Models used for the X-ray spectral analysis (B5 to C1). See Table 4 and Section 4.2 for details.

Model B9:

$\mathrm{TBABS_{Gal}} \times (C_{\mathrm{BAT}} \times \mathrm{ZPHABS} \times \mathrm{CABS} \times \mathrm{CUTOFFPL} + \mathrm{PEXRAV} + \mathrm{APEC} + \mathrm{APEC})$.

Same as model B3, with the exception of the scattered component. This model was applied only for SWIFT J0319.7 +4132 (NGC 1275).

4.2.3. Blazars

A total of 97 objects were fitted using this set of models (i.e., models C1 to C7; bottom panel of Figure 6). For all the blazars, with the exception of the eight listed in Section 4, we considered a power law for the primary X-ray emission and did not take into account reprocessed radiation. The models we applied are the following.

Model C1:

$\mathrm{TBABS_{Gal}} \times C_{\mathrm{BAT}} \times \mathrm{ZPHABS} \times \mathrm{CABS} \times \mathrm{POW}$.

This model considers an absorbed power-law continuum. Used for 52 objects.

Model C2:

$\mathrm{TBABS_{Gal}} \times C_{\mathrm{BAT}} \times (\mathrm{ZPHABS} \times \mathrm{CABS} \times \mathrm{POW} + \mathrm{BB})$.

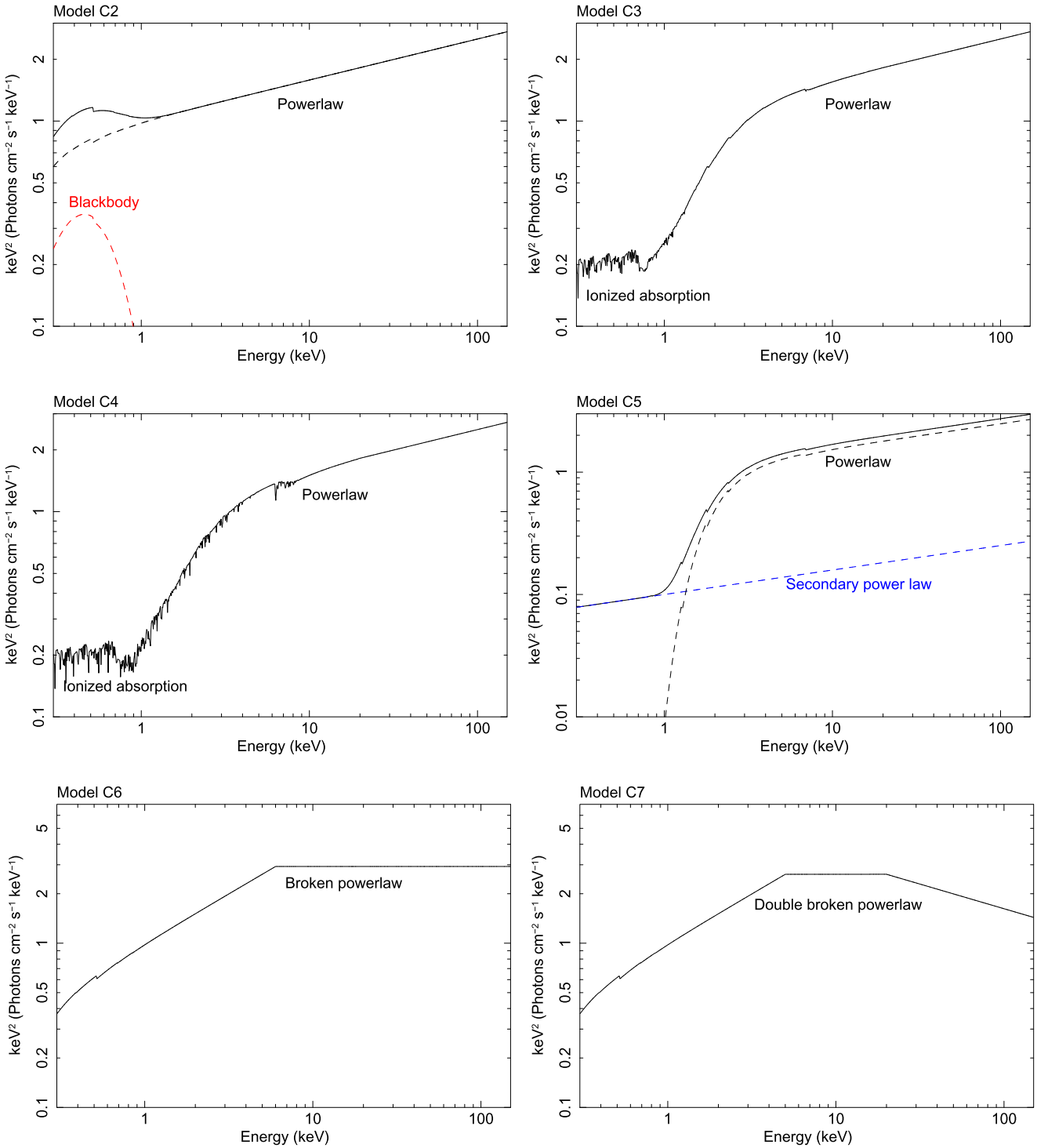

Figure 11. Models used for the X-ray spectral analysis (C2 to C7). See Table 4 and Section 4.2 for details.

Same as model C1, plus a blackbody component. Used for 10 blazars.

Model C3:

$\mathrm{TBABS_{Gal}} \times C_{\mathrm{BAT}} \times \mathrm{ZPHABS} \times \mathrm{CABS} \times \mathrm{ZXIPCF} \times \mathrm{POW}$.

Same as model C1, including also an ionized absorption component. Used for three objects: SWIFT J0507.7+6732, SWIFT J1224.9+2122, and SWIFT J1625.9+4349 (87GB 050246.4+673341, PG 1222+216, and 87GB 162418.8+435342, respectively).

Model C4:

$\mathrm{TBABS_{Gal}} \times C_{\mathrm{BAT}} \times \mathrm{ZPHABS} \times \mathrm{CABS} \times \mathrm{ZXIPCF} \times \mathrm{ZXIPCF} \times \mathrm{POW}$.

Same as model C1, plus two ionized absorption components. Used for two objects: SWIFT J1557.8−7913 (PKS 1549−79) and SWIFT J2346.8+5143 (2MASX J23470479+5142179).

Model C5:

$\mathrm{TBABS_{Gal}} \times C_{\mathrm{BAT}} \times (\mathrm{ZPHABS} \times \mathrm{CABS} \times \mathrm{POW} + f_{\mathrm{scatt}} \times \mathrm{POW})$.

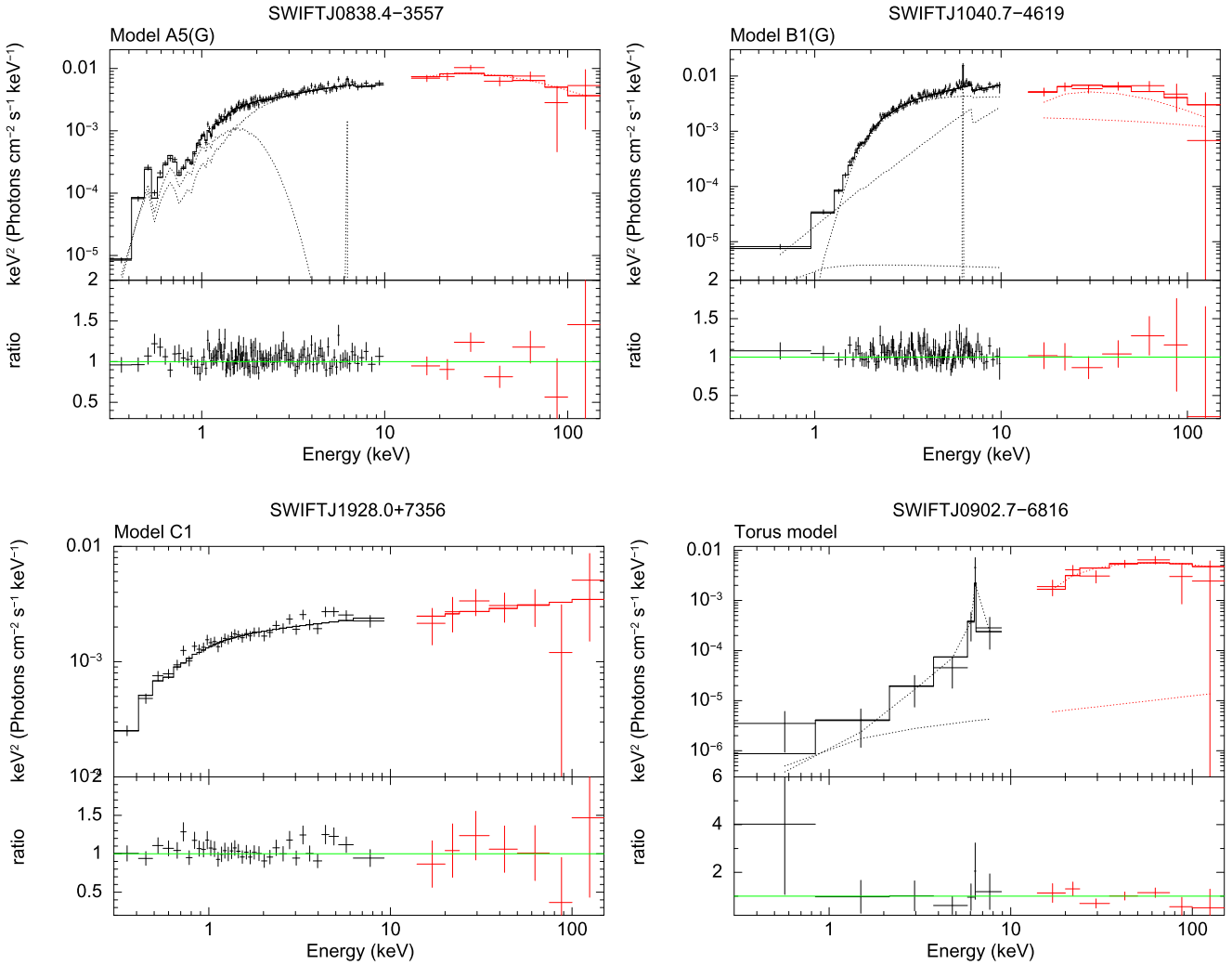

Figure 12. Example of spectra fitted with different models. Top left panel: *XMM-Newton* EPIC/PN (black) and *Swift*/BAT (red) spectrum of SWIFT J0838.4−3557 fitted with model A5, which considers the X-ray continuum and a blackbody component absorbed by a partially covering ionized absorber, plus a Gaussian line. Top right panel: *XMM-Newton* EPIC/PN (black) and *Swift*/BAT (red) spectrum of SWIFT J1040.7−4619 fitted with model B1, which includes an obscured X-ray continuum, reflection, a scattered cutoff power-law component, and a Gaussian line. Bottom left panel:*Swift*/XRT (black) and BAT (red) spectrum of the blazar SWIFT J1928.0+7356 fitted with model C1 (i.e., power-law continuum plus absorption). Bottom right panel: *Swift*/XRT (black) and BAT (red) spectrum of the CT AGN SWIFT J0902.7−6816 fitted with a self-consistent torus model plus a scattered component. The bottom panels of the four figures show the ratio between the models and the data.

Same as model C1, plus a power-law component, which might be either unobscured jet emission or scattered emission as in obscured nonblazar AGNs. Used for six blazars.

Model C6:

$\mathrm{TBABS_{Gal}} \times C_{\mathrm{BAT}} \times \mathrm{ZPHABS} \times \mathrm{CABS} \times \mathrm{BKN}$.

In this model the primary X-ray emission is produced by a broken power law. Used for 23 sources.

Model C7:

$\mathrm{TBABS_{Gal}} \times C_{\mathrm{BAT}} \times (\mathrm{ZPHABS} \times \mathrm{CABS} \times \mathrm{BKN2})$.

In this model the primary X-ray component is described by a double broken power law. Used only for SWIFT J1256.2−0551 (3C 279).

4.2.4. Other Models

For two objects (SWIFT J0956.1+6942 and SWIFT J2234.8−2542) we used two additional models to reproduce their X-ray emission.

Model D1:

$\mathrm{TBABS_{Gal}} \times C_{\mathrm{BAT}} \times [\mathrm{ZPHABS} \times \mathrm{CABS} \times \mathrm{CUTOFFPL} + \mathrm{ZPHABS} \times \mathrm{CABS} \times (\mathrm{APEC} + \mathrm{APEC})]$.

Just in one case, the nearby star-forming galaxy SWIFT J0956.1+6942 (M82, $z = 0.000677$, i.e., the closest extragalactic *Swift*/BAT source), was it necessary to use a model that consisted of a cutoff power-law X-ray continuum and two absorbed collisional plasmas. No AGN is present in this object (e.g., Gandhi et al. 2011), and all the X-ray flux can be explained by star formation (e.g., Ranalli et al. 2008). In this model the cutoff power law represents the X-ray emission of the population of X-ray binaries, while the two collisionally ionized plasma models take into account the emission from hot gas. The results obtained by the spectral analysis for this object are summarized in Appendix C.

Model D2:

$\mathrm{TBABS_{Gal}} \times \mathrm{ZPHABS} \times \mathrm{CABS} \times \mathrm{POW}$.

Table 8
Parameters of the Gaussian Lines

(1) Source	(2) $E_{K\alpha}$ (keV)	(3) EW (eV)	(4) σ (eV)	(5) Normalization (10^{-6} ph cm^{-2} s^{-1})
SWIFT J0005.0+7021	$6.43^{+0.08}_{-0.07}$	80^{+25}_{-36}	...	$4.8^{+2.7}_{-2.7}$
SWIFT J0006.2+2012	6.4[a]	110^{+76}_{-53}	...	$6.9^{+3.2}_{-2.8}$
SWIFT J0009.4−0037	6.4[a]	$\leqslant 676$	...	$5.5^{+8.1}_{-3.9}$
SWIFT J0010.5+1057	$6.12^{+0.09}_{-0.38}$	162^{+116}_{-113}	...	$17.8^{+13.5}_{-9.5}$
SWIFT J0025.8+6818	$6.48^{+0.06}_{-0.05}$	836^{+595}_{-778}	...	$11.9^{+9.3}_{-6.8}$
SWIFT J0030.0−5904	$5.5^{+0.7}_{-0.5}$	7300^{+4056}_{-5641}	...	$\leqslant 9.2$
SWIFT J0036.3+4540	$6.52^{+0.60}_{-0.09}$	585^{+232}_{-411}	...	$37.4^{+31.0}_{-27.4}$
SWIFT J0042.9+3016B	6.4[a]	$\leqslant 721$	...	$\leqslant 26.4$
SWIFT J0046.2−4008	$6.40^{+0.04}_{-0.04}$	92^{+30}_{-10}	...	$4.0^{+1.4}_{-1.4}$
SWIFT J0048.8+3155	$6.39^{+0.03}_{-0.02}$	53^{+7}_{-6}	...	$24.7^{+6.0}_{-6.0}$

Note. Column (1): sources for which a Gaussian line was added to the broadband spectral model. Column (2): energy. Column (3): equivalent width. Column (4): width. Column (5): normalization of the line. The uncertainties on the equivalent width represent the 68% confidence interval. NC—not constrained.
[a] Value fixed.

(This table is available in its entirety in machine-readable form.)

Table 9
Spectral Parameters Obtained with the Torus Model

(1) Source	(2) θ_{OA} (Deg)	(3) $\log N_H$ (cm^{-2})	(4) Γ	(5) f_{scatt} (%)	(6) kT (keV)	(7) C_{BAT}	(8) Statistic/dof
SWIFT J0009.4−0037	60[a]	23.56 [23.41–23.70]	$1.66^{+0.29}_{-0.27}$	$1.1^{+1.7}_{-0.7}$	...	...	102.1/86
SWIFT J0025.8+6818	$\geqslant 42$	24.14 [23.72–24.32]	$1.94^{+0.27}_{-0.56}$	$\leqslant 1.3$	...	$0.39^{+0.78}_{-0.27}$	46.5/49
SWIFT J0030.0−5904	60[a]	24.03 [23.79–24.43]	$1.78^{+0.35}_{-0.38}$	$\leqslant 0.8$	...	...	22.3/17
SWIFT J0105.5−4213	60[a]	24.18 [23.95–24.30]	$2.12^{+0.25}_{-0.41}$	$\leqslant 0.6$	...	...	32.6/38
SWIFT J0106.8+0639	$\leqslant 66$	23.54 [23.46–23.66]	$1.83^{+0.15}_{-0.19}$	$1.6^{+1.4}_{-0.8}$	...	...	99.2/104
SWIFT J0111.4−3808	$\geqslant 78$	24.33 [24.32–24.34]	$2.64^{+0.11}_{-0.09}$	$\leqslant 0.1$	...	...	380.7/295
SWIFT J0122.8+5003	58^{+12}_{-14}	24.24 [24.09–24.58]	$2.81^{+0.16}_{-0.15}$	$\leqslant 0.1$	...	...	91.6/115
SWIFT J0128.9−6039	60[a]	24.13 [23.90–24.32]	$2.18^{+0.21}_{-0.36}$	$\leqslant 0.1$	...	...	25.7/25
SWIFT J0130.0−4218	$\geqslant 36$	24.20 [24.02–24.55]	$2.45^{+0.35}_{-0.15}$	$\leqslant 0.02$	...	...	22.5/22
SWIFT J0131.8−3307	$\leqslant 79$	23.89 [23.74–23.96]	$2.08^{+0.28}_{-0.36}$	$\leqslant 0.1$	$0.85^{+0.21}_{-0.27}$	...	49.4/42

Notes. The table lists, for the objects with $\log(N_H/cm^{-2})$ within their 90% confidence intervals, the following. Column (1): sources for which the torus model of Brightman & Nandra (2011) was applied. Column (2): half-opening angle of the torus. Column (3): column density. Column (4): photon index. Column (5): fraction of scattered radiation. Column (6): temperature of the thermal plasma. Column (7): cross-calibration constant between the soft and hard X-ray spectra. Column (8): value of the statistic and the dof.
[a] Value fixed.

(This table is available in its entirety in machine-readable form.)

For SWIFT J2234.8−2542 we combined the results of the spectral analysis of the *BeppoSAX* spectrum (Malizia et al. 2000) with the *Swift*/BAT spectrum. This was done fitting the *Swift*/BAT spectrum, fixing the column density to the value reported by Malizia et al. (2000), with model D2.

4.2.5. Compton-thick AGNs

In order to self-consistently take into account absorbed and reprocessed X-ray radiation, the 75 sources that, after being fitted with the models reported above, were found to have column density values consistent with $N_H \sim 10^{24}$ cm^{-2}, within their 90% uncertainties, were fitted with the spherical-toroidal model of Brightman & Nandra (2011). The free parameters of this model are the column density, which is the same for every line of sight intercepting the torus; the half-opening angle of the torus (θ_{OA}); and the inclination angle (θ_i). We left θ_{OA} free to vary unless the parameter could not be constrained, in which case it was fixed to 60°. To reduce the degree of complexity of the models, the value of θ_i was fixed to the maximum allowed value (87°) for all sources. The main properties of the CT AGNs from our sample have been reported in a recently published paper (Ricci et al. 2015), while the spectral parameters obtained are listed in Table 9.

Table 10
Median Values of the Parameters Obtained by the Broadband X-Ray Spectral Analysis of the Nonblazar AGN of Our Sample

(1)	(2)	(3)	(4)	(5)	(6)
			Nonblazar AGNs		
Parameters	All	<22	$\geqslant 22$	22–24	$\geqslant 24$
$\log L_{2-10}$[a]	43.41	43.56	43.26	43.24	43.46
$\log L_{20-50}$[b]	43.38	43.58	43.22	43.23	43.12
$\log L_{14-150}$[c]	43.74	43.92	43.62	43.63	43.53
Γ[d]	1.78 ± 0.01	1.80 ± 0.02	1.76 ± 0.02	1.70 ± 0.02	2.05 ± 0.05
$\Gamma_{\rm BAT}$[e]	1.96 ± 0.01	2.02 ± 0.02	1.89 ± 0.02	1.90 ± 0.02	1.75 ± 0.04
$C_{\rm BAT}$[f]	1.00 ± 0.05	1.00 ± 0.05	1.00 ± 0.08	1.00 ± 0.09	1.00 ± 0.12
$E_{\rm C}$[g]	381 ± 16	384 ± 21	380 ± 24	386 ± 25	341 ± 70
$E_{\rm C}$[h]	200 ± 29	210 ± 36	189 ± 26	188 ± 27	449 ± 64
$E_{\rm C}$[i]	76 ± 6	80 ± 7	74 ± 11	74 ± 11	43 ± 15
R[j]	0.53 ± 0.09	0.83 ± 0.14	0.37 ± 0.11	0.38 ± 0.11	0.15 ± 0.12
R[k]	1.3 ± 0.1	1.8 ± 0.2	0.6 ± 0.2	0.6 ± 0.2	0.25 ± 0.10
$N_{\rm H}$[l]	10^{22}	10^{20}	1.5×10^{23}	10^{23}	2×10^{24}
$N_{\rm H}^{\rm W}$[m]	2.8×10^{22}	2.8×10^{22}	...	...	...
$f_{\rm C}^{\rm W}$[n]	63 ± 4	63 ± 4	...	...	...
$\log \xi$[o]	1.45 ± 0.16	1.45 ± 0.16	...	...	...
$kT_{\rm bb}$[p]	0.110 ± 0.003	0.110 ± 0.003	...	...	...
$f_{\rm scatt}$[q]	1.0 ± 0.5	...	1.0 ± 0.4	1.1 ± 0.5	0.6 ± 0.5
$f_{\rm scatt}$[r]	1.4 ± 0.6	...	1.4 ± 0.6	1.5 ± 0.5	0.4 ± 0.3
$kT_{\rm therm.}$[s]	0.50 ± 0.05	...	0.50 ± 0.05	0.49 ± 0.06	0.56 ± 0.07

Notes. The table lists the median values of the parameters (column (1)) obtained by the broadband X-ray spectral analysis for the whole sample of nonblazar AGNs (column (2)), objects with $N_{\rm H} < 10^{22}$ cm^{-2} (column (3)), sources with $N_{\rm H} \geqslant 10^{22}$ cm^{-2} (column (4)), AGNs with $N_{\rm H} = 10^{22-24}$ cm^{-2} (column (5)), and objects with $N_{\rm H} \geqslant 10^{24}$ cm^{-2} (column (6)).
[a] Absorption-corrected and k-corrected 2–10 keV luminosity (log(erg s^{-1})). See Section 5.1.
[b] Absorption-corrected and k-corrected 20–50 keV luminosity (log(erg s^{-1})). See Section 5.1.
[c] Absorption-corrected and k-corrected 14–150 keV luminosity (log(erg s^{-1})). See Section 5.1.
[d] Photon index obtained by fitting the 0.3–150 keV spectrum (Section 5.2.1).
[e] Photon index obtained by fitting *Swift*/BAT spectrum with a power-law model (Section 5.2.1).
[f] Cross-calibration constant between the 0.3–10 keV and the *Swift*/BAT spectra (Section 5.2.2).
[g] Cutoff energy (keV) obtained considering also upper and lower limits (Section 5.2.3).
[h] Cutoff energy (keV) obtained considering the lower limits and applying the Kaplan–Meier estimator (Section 5.2.3).
[i] Cutoff energy (keV) obtained using only the sources for which the parameter could be inferred (Section 5.2.3).
[j] Reflection parameter obtained considering also upper and lower limits (Section 5.2.4).
[k] Reflection parameter obtained using only the sources for which the parameter could be inferred (Section 5.2.4).
[l] Column density of the neutral material (cm^{-2}). See Section 5.3.1.
[m] Column density of the ionized absorber (cm^{-2}). See Section 5.3.2.
[n] Covering factor of the ionized absorber (%). See Section 5.3.2.
[o] Ionization parameter of the warm absorber (erg cm s^{-1}). See Section 5.3.2.
[p] Temperature of the blackbody component (keV). See Section 5.4.1.
[q] Fraction of scattered radiation (%) obtained considering also upper and lower limits (Section 5.4.2).
[r] Fraction of scattered radiation (%) obtained using only the sources for which the parameter could be inferred (Section 5.4.2).
[s] Temperature of the thermal plasma (keV). See Section 5.4.2.

5. Results

In the following we report the results obtained by the broadband X-ray spectral analysis of the 836 AGNs of our sample. In Section 5.1 we describe how we calculated the fluxes and luminosities and discuss the luminosity distributions of different classes of AGNs. In Section 5.2 we discuss the properties of the X-ray continuum, in particular the photon index (Section 5.2.1), the cross-calibration constant (Section 5.2.2), the high-energy cutoff (Section 5.2.3), and the reflection component (Section 5.2.4). In Section 5.3 we summarize the properties of the neutral (Section 5.3.1) and ionized (Section 5.3.2) absorbers, while in Section 5.4 we discuss those of the soft excess for unobscured (Section 5.4.1) and obscured (Section 5.4.2) nonblazar AGNs. The median values of the parameters of nonblazar AGNs and blazars are reported in Tables 10 and 11, respectively. Through the paper the errors on the median values are the median absolute deviations.

5.1. Fluxes and Luminosities

The absorption-corrected fluxes of the continuum emission (i.e., excluding the soft excess and Fe Kα component) were measured in three energy bands: 2–10 keV, 20–50 keV, and 14–150 keV (F_{2-10}, F_{20-50}, and F_{14-150}, respectively). To be consistent with what was reported in the *Swift*/BAT catalogs, we also report the fluxes in the 14–195 keV band (F_{14-195}), which were obtained by extrapolating the 14–150 keV fluxes by assuming a power law with a photon index of $\Gamma = 1.8$, consistent with the typical value

Table 11
Median Values of the Parameters Obtained by Our Spectral Analysis

(1)	(2)	(3)	(4)	(5)
		Blazars		
Parameters	All	BZQ	BZB	BZU
$\log L_{2-10}$[a]	45.37	46.23	45.09	44.25
$\log L_{20-50}$[b]	45.15	46.48	44.63	44.20
$\log L_{14-150}$[c]	45.53	47.01	44.92	44.70
Γ[d]	1.68 ± 0.04	1.54 ± 0.05	2.05 ± 0.06	1.67 ± 0.09
$\Gamma_{\rm BAT}$[e]	1.87 ± 0.06	1.71 ± 0.06	2.42 ± 0.10	1.85 ± 0.11
$C_{\rm BAT}$[f]	1.00 ± 0.35	0.80 ± 0.15	1.10 ± 0.63	1.20 ± 0.45
$N_{\rm H}$[g]	2.6×10^{20}	1.0×10^{20}	4.0×10^{20}	1.6×10^{21}

Notes. The table lists the median values of the parameters obtained by the broadband X-ray spectral analysis (column (1)) for the whole sample of blazars (column (2)), for the flat-spectrum radio quasars (column (3)), for the BL Lacs (column (4)), and for the blazars of uncertain type (column (5)).
[a] Absorption-corrected and *k*-corrected 2–10 keV luminosity (log(erg s^{-1})). See Section 5.1.
[b] Absorption-corrected and *k*-corrected 20–50 keV luminosity (log(erg s^{-1})). See Section 5.1.
[c] Absorption-corrected and *k*-corrected 14–150 keV luminosity (log(erg s^{-1})). See Section 5.1.
[d] Photon index obtained by fitting the 0.3–150 keV spectrum (Section 5.2.1).
[e] Photon index obtained by fitting the *Swift*/BAT spectrum with a power-law model (Section 5.2.1).
[f] Cross-calibration constant between the 0.3–10 keV and the *Swift*/BAT spectra (Section 5.2.1).
[g] Column density of the neutral material (cm^{-2}). See Section 5.3.1.

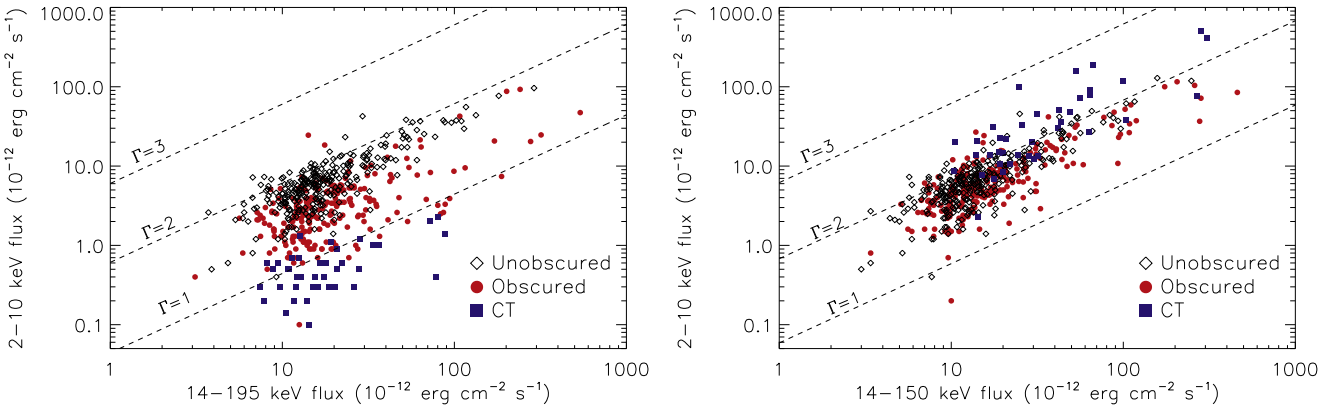

Figure 13. Left panel: observed 2–10 keV flux vs. the observed 14–195 keV *Swift*/BAT flux reported in Baumgartner et al. (2013) for the nonblazar AGNs of our sample. Right panel: absorption-corrected 2–10 keV flux vs. the absorption-corrected flux in the 14–150 keV range. In both panels the dashed lines represent the fluxes expected for values of the photon index of $\Gamma = 1$, 2, and 3, assuming that the X-ray continuum is produced by a simple power-law component. The nonblazar AGNs are divided into unobscured, obscured, and CT.

found for *Swift*/BAT AGNs (see Section 5.2.1). In the left panel of Figure 13 we show the observed 2–10 keV flux versus the 14–195 keV flux, while in the right panel we show the absorption-corrected 2–10 keV flux versus the absorption-corrected 14–150 keV flux. The plot shows that, once the emission has been corrected for absorption, most of the sources lie in the region predicted for a power-law continuum with a slope in the range $\Gamma = 1$–3. In Table 12 we report the values of the observed 2–10 keV and 14–195 keV fluxes ($F_{2-10}^{\rm obs}$ and $F_{14-195}^{\rm obs}$, respectively) and of the intrinsic 2–10 keV, 20–50 keV, 14–150 keV, and 14–195 keV fluxes for all the sources of our sample.

The absorption-corrected and *k*-corrected continuum luminosities were calculated, for the 803 sources for which spectroscopic redshifts were available, in the 2–10 keV, 20–50 keV, 14–150 keV, and 14–195 keV bands (L_{2-10}, L_{20-50}, L_{14-150}, and L_{14-195}, respectively) using the following relation:

$$L_{\rm i} = 4\pi d_{\rm L}^2 \frac{F_{\rm i}}{(1+z)^{2-\Gamma}}, \quad (1)$$

where $F_{\rm i}$ is either the 2–10 keV, 20–50 keV, 14–150 keV, or 14–195 keV flux and $d_{\rm L}$ is the luminosity distance. We used redshift-independent distance for the 44 objects at $z < 0.01$ for which these measurements were available (see Section 2.2.1). For blazars the *k*-correction was calculated using the broadband Γ for L_{2-10} and the photon index obtained by fitting the *Swift*/BAT spectra with a single power-law model ($\Gamma_{\rm BAT}$) for the L_{20-50}, L_{14-150}, and L_{14-195} luminosities. The observed (i.e., *k*-corrected but not absorption-corrected) 2–10 keV and 14–195 keV luminosities ($L_{2-10}^{\rm obs}$ and $L_{14-195}^{\rm obs}$, respectively) were calculated in a similar way. In Table 13 we report the observed 2–10 keV and 14–195 keV luminosities and the intrinsic 2–10 keV, 20–50 keV, 14–150 keV, and 14–195 keV luminosities for all the sources in our sample with spectroscopic redshifts.

The distributions of L_{14-150} and L_{2-10} for nonblazar AGNs are shown in the top panels of Figure 14. These panels show that the median luminosity of unobscured AGNs is higher than

Table 12
X-Ray Fluxes of the Sources of Our Sample

	Observed		Intrinsic			
(1)	(2)	(3)	(4)	(5)	(6)	(7)
SWIFT ID	F_{2-10}^{obs} (10^{-12} erg cm^{-2} s^{-1})	F_{14-195}^{obs} (10^{-12} erg cm^{-2} s^{-1})	F_{2-10} (10^{-12} erg cm^{-2} s^{-1})	F_{20-50} (10^{-12} erg cm^{-2} s^{-1})	F_{14-150} (10^{-12} erg cm^{-2} s^{-1})	F_{14-195} (10^{-12} erg cm^{-2} s^{-1})
SWIFT J0001.0−0708	7.3	13.0	8.4	5.4	10.8	12.3
SWIFT J0001.6−7701	3.2	10.1	5.2	3.7	9.0	10.3
SWIFT J0002.5+0323	4.8	11.7	4.8	4.0	8.7	9.9
SWIFT J0003.3+2737	1.7	13.0	3.1	4.3	11.2	12.8
SWIFT J0005.0+7021	3.6	12.7	4.7	5.6	10.6	12.1
SWIFT J0006.2+2012	6.0	18.4	11.2	7.0	14.2	16.2
SWIFT J0009.4−0037	0.8	9.3	3.1	3.5	10.6	12.1
SWIFT J0010.5+1057	7.7	31.4	7.7	10.5	26.8	30.6
SWIFT J0017.1+8134	3.3	10.1	3.4	4.3	9.6	11.0
SWIFT J0021.2−1909	10.6	17.3	11.2	6.9	14.0	16.0

Note. Column (2): observed 2–10 keV flux. Column (3): observed 14–195 keV flux. Column (4): intrinsic 2–10 keV flux. Column (5): intrinsic 20–50 keV flux. Column (6): intrinsic 14–150 keV flux. Column (7): intrinsic 14–195 keV flux.

(This table is available in its entirety in machine-readable form.)

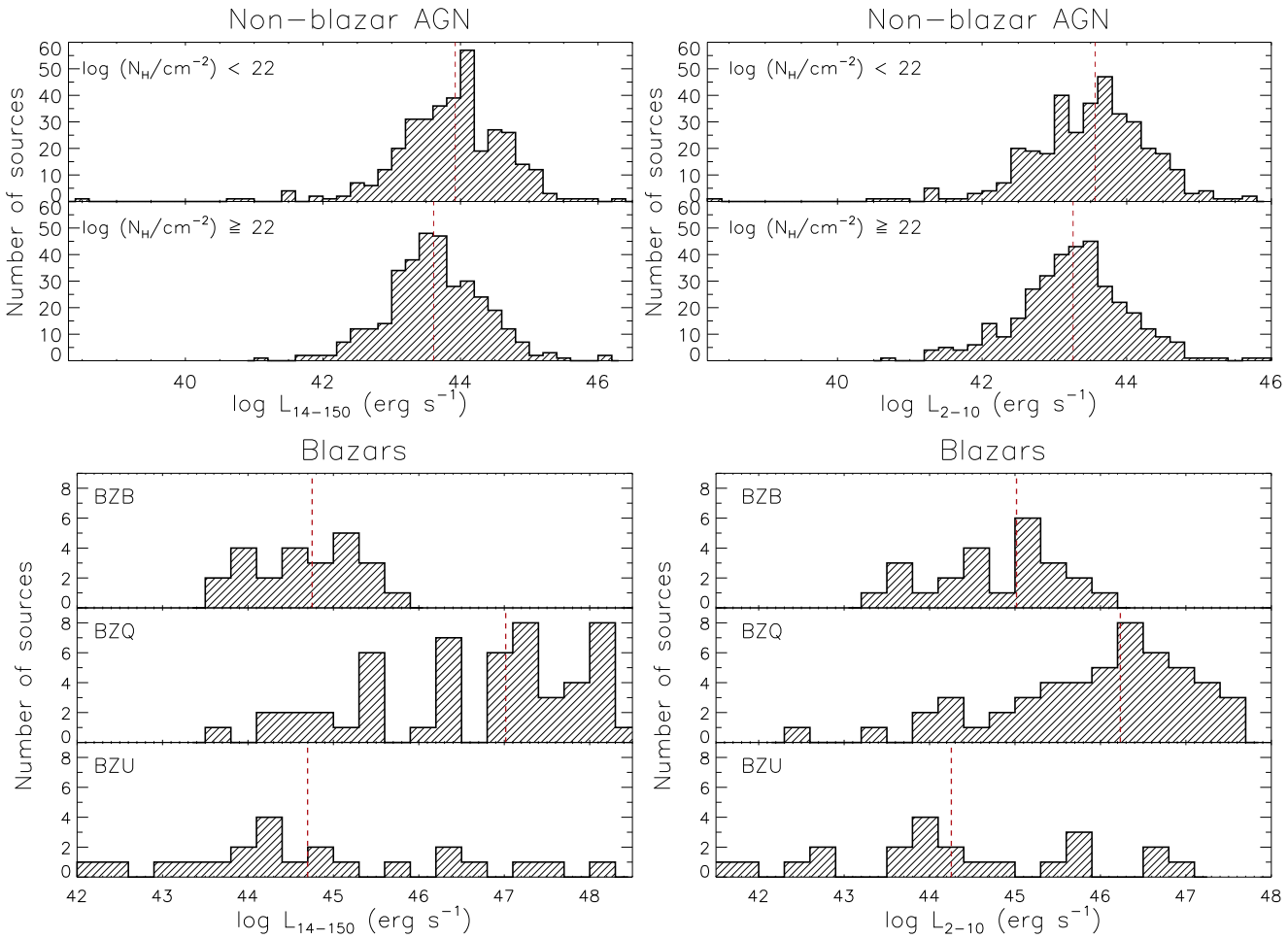

Figure 14. Top panels: absorption-corrected 14–150 keV (left panel) and 2–10 keV (right panel) luminosity distributions of the nonblazar AGNs of our sample. Nonblazar AGNs are divided into sources with $N_{\rm H} < 10^{22}$ cm^{-2} and those with $N_{\rm H} \geqslant 10^{22}$ cm^{-2}. In both panels the red dashed vertical lines represent the median value of the luminosity. Bottom panels: absorption-corrected 14–150 keV (left panel) and 2–10 keV (right panel) luminosity distributions of the blazars. The blazars are divided into BL Lacs (BZB), flat-spectrum radio quasars (BZQ), and blazars of uncertain type (BZU). In both panels the red dashed vertical lines show the median value of the luminosity for the different types of blazars. The median values of the luminosities are listed in Tables 10 and 11 for nonblazar AGNs and blazars, respectively.

Table 13
X-Ray Luminosities of the Sources of Our Sample

	Observed		Intrinsic			
(1)	(2)	(3)	(4)	(5)	(6)	(7)
SWIFT ID	$\log L_{2-10}^{\rm obs}$ (erg s^{-1})	$\log L_{14-195}^{\rm obs}$ (erg s^{-1})	$\log L_{2-10}$ (erg s^{-1})	$\log L_{20-50}$ (erg s^{-1})	$\log L_{14-150}$ (erg s^{-1})	$\log L_{14-195}$ (erg s^{-1})
SWIFT J0001.0−0708	43.37	43.62	43.43	43.24	43.54	43.60
SWIFT J0001.6−7701	43.41	43.91	43.62	43.48	43.86	43.92
SWIFT J0002.5+0323	42.85	43.24	42.85	42.78	43.11	43.17
SWIFT J0003.3+2737	42.79	43.67	43.05	43.19	43.61	43.67
SWIFT J0005.0+7021	43.90	44.45	44.02	44.09	44.37	44.43
SWIFT J0006.2+2012	42.97	43.46	43.24	43.04	43.34	43.40
SWIFT J0009.4−0037	43.01	44.07	43.60	43.65	44.13	44.19
SWIFT J0010.5+1057	44.18	44.79	44.18	44.31	44.72	44.78
SWIFT J0017.1+8134	47.22	47.71	47.23	47.33	47.68	47.74
SWIFT J0021.2−1909	44.38	44.59	44.40	44.19	44.50	44.55

Note. Column (2) observed 2–10 keV luminosity. Column (3): observed 14–195 keV luminosity. Column (4) intrinsic 2–10 keV luminosity. Column (5): intrinsic 20–50 keV luminosity. Column (6): intrinsic 14–150 keV luminosity. Column (7): intrinsic 14–195 keV luminosity.

(This table is available in its entirety in machine-readable form.)

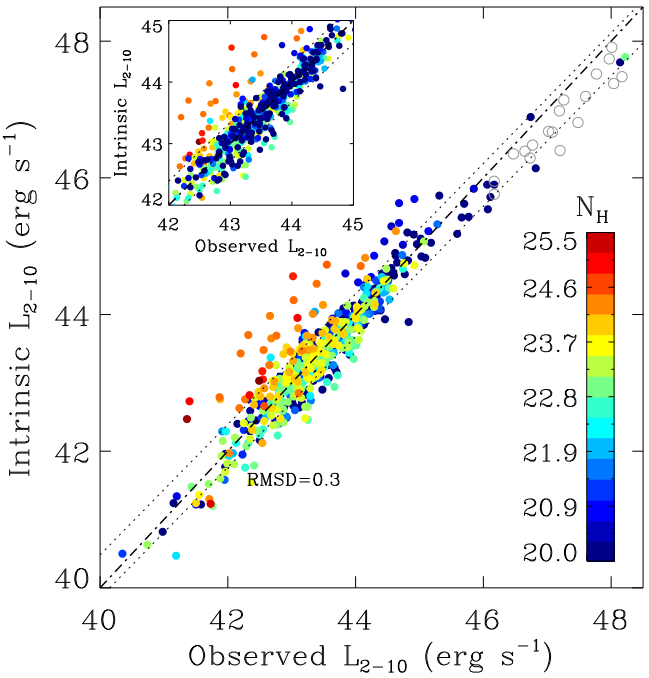

Figure 15. Intrinsic 2–10 keV luminosity obtained by our spectral fitting vs. the value calculated from the observed 14–195 keV luminosity ($L_{2-10}(\mathrm{obs}) = 0.37 \times L_{14-195}$). The top left panel shows a zoom-in of the $\log L_{2-10} = \log L_{2-10}(\mathrm{obs}) = 42$–45 region, plotting the unobscured sources on top of the obscured. The dot-dashed line represents the $L_{2-10} = L_{2-10}(\mathrm{obs})$ case, while the dotted lines show the scatter of the correlation. The blazars are illustrated as open points and were not used for the fit. The plot shows that for objects with column densities $\log(N_H/\mathrm{cm}^{-2}) \lesssim 23.7$ the two values of the 2–10 keV luminosity are consistent (with a scatter of ∼0.3 dex).

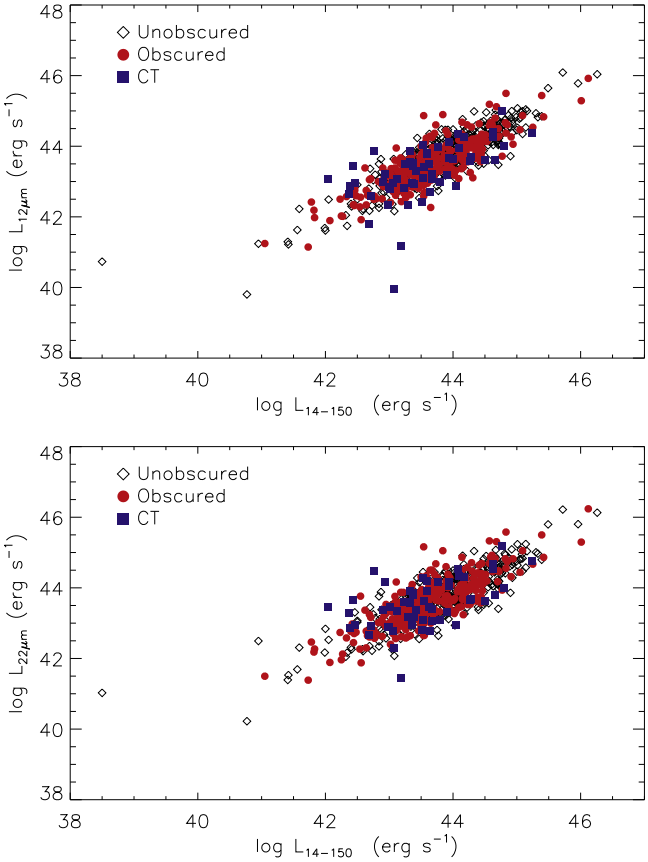

Figure 16. Top panel: intrinsic 14–150 keV luminosity vs. the 12 μm luminosity for unobscured (open black diamonds), obscured (red circles), and CT (blue squares) nonblazar AGNs. Bottom panel: same as the top panel, but for the 22 μm luminosities.

that of obscured AGNs. This is likely related to the intrinsically different luminosity functions of obscured and unobscured AGNs (e.g., Della Ceca et al. 2008; Burlon et al. 2011; Aird et al. 2015) and is consistent with the observed decrease of the fraction of obscured sources with increasing luminosity (e.g., Ueda et al. 2003, 2014; Treister & Urry 2006; Burlon et al. 2011). Due to the strong beaming, blazars (right panel of Figure 14) have on average higher luminosities than nonblazar AGNs. As seen in many previous studies, among the blazars the flat-spectrum radio quasars are significantly more luminous than the BL Lacs (e.g., Fossati et al. 1998; Ghisellini et al. 2010).

In Koss et al. (2017) we reported the observed 2–10 keV luminosities obtained by transforming the observed 14–195 keV luminosities into 2–10 keV luminosities using a correction factor of 0.37 (i.e., $L_{2-10}(\mathrm{obs}) = 0.37 \times L_{14-195}$). In Figure 15 we show that the values of $L_{2-10}(\mathrm{obs})$ for objects with $\log(N_H/\mathrm{cm}^{-2}) \lesssim 23.7$ are in good agreement with the 2–10 keV luminosities inferred from our spectral analysis. The scatter of ∼0.3 dex in the plot is likely due to differences in the shape of the X-ray continuum and to intrinsic flux variability of the primary X-ray emission. Above $\log(N_H/\mathrm{cm}^{-2}) \simeq 23.7$ Compton scattering becomes non-negligible, and even the hard X-ray emission is depleted (see Figure 1 of Ricci et al. 2015), resulting in underestimated values of $L_{2-10}(\mathrm{obs})$. It should be remarked that while most CT AGNs lie in the range $\Gamma = 1.7$–2.3 (Figure 13), a few sources have absorption-corrected 2–10 keV fluxes considerably higher than those expected using the 14–150 keV flux, and their L_{2-10} emission might be overestimated. In the top panel of Figure 16 we illustrate the relation between the intrinsic 14–150 keV luminosity and the 12 μm luminosity (from *WISE* and high spatial resolution observations) for the objects of our sample. A clear correlation between the mid-IR and X-ray luminosity of nonblazar AGNs has been found in the past years by a large number of studies (e.g., Lutz et al. 2004; Gandhi et al. 2009; Ichikawa et al. 2012, 2017; Asmus et al. 2015; Stern 2015) and has been interpreted as the signature of reprocessing of the accreting SMBH emission by dust in the torus. The plot shows that CT AGNs follow the same trend as obscured and unobscured sources, thus confirming that we are able to accurately constrain the intrinsic hard X-ray luminosity for these objects. A similar trend is also observed considering the 22 μm luminosities (bottom panel of Figure 16). We therefore recommend, for CT AGNs, using the 20–50 keV and 14–150 keV fluxes and luminosities and the intrinsic 2–10 keV fluxes and luminosities obtained from *Swift*/BAT luminosities assuming $\Gamma = 1.8$ (see Table 14).

5.2. X-Ray Continuum Properties

5.2.1. Photon Index

The distribution of photon indices inferred from the broadband spectral analysis is shown in the top left panel of Figure 17 for unobscured and obscured AGNs.[30] We find that the median values (red dashed vertical lines) of Γ for sources with

[30] The median of the uncertainties on the photon index for the whole sample of nonblazar AGNs is $\Delta\Gamma = 0.17$.

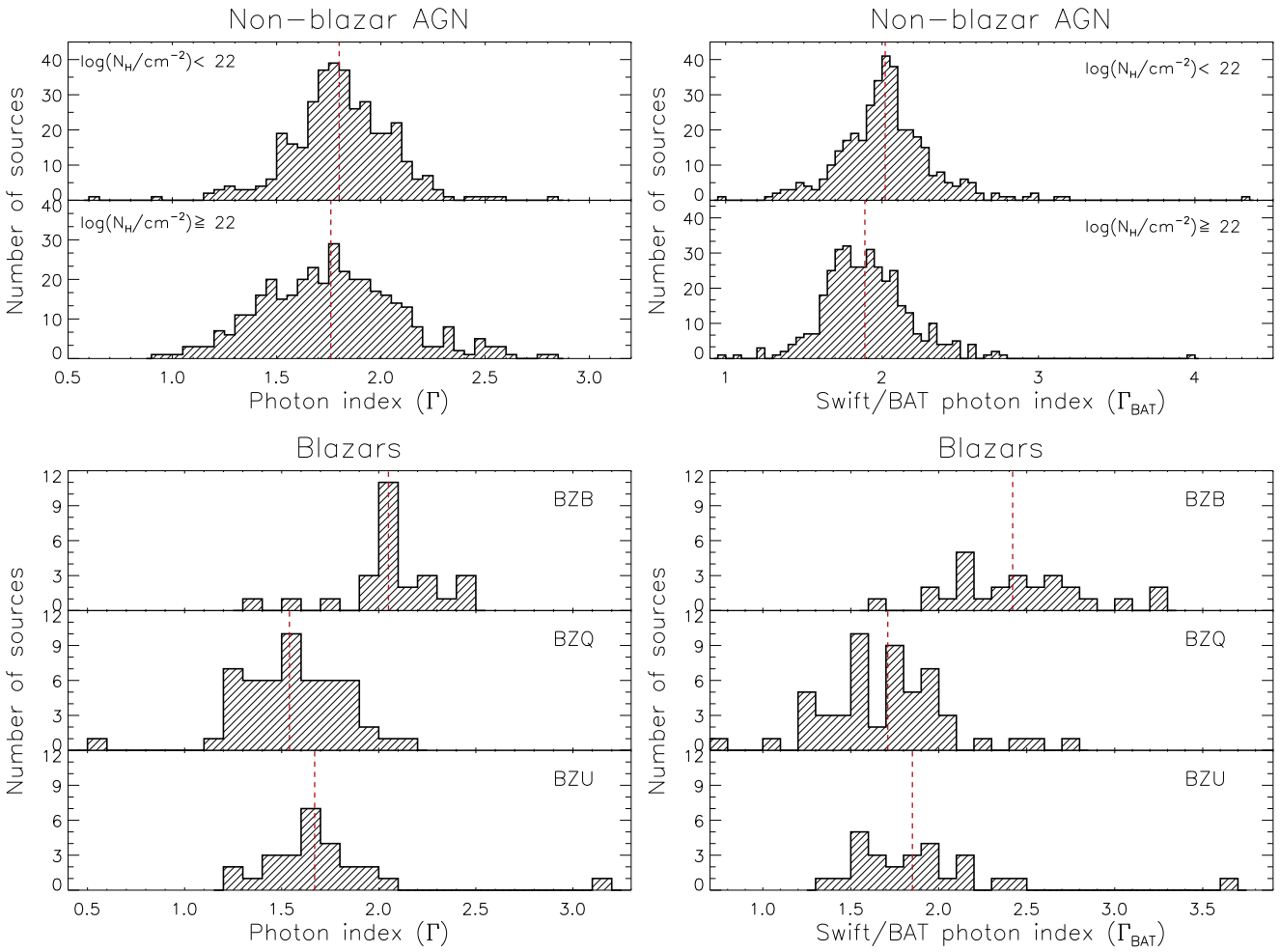

Figure 17. Top left panel: distribution of the best-fitting photon indices obtained by the broadband X-ray spectroscopy for nonblazar AGNs with $N_{\rm H} < 10^{22}$ cm^{-2} (top panel) and $N_{\rm H} \geqslant 10^{22}$ cm^{-2} (bottom panel). Top right panel: distribution of the photon indices obtained fitting the *Swift*/BAT spectra of nonblazar AGNs with $N_{\rm H} < 10^{22}$ cm^{-2} (top panel) and $N_{\rm H} \geqslant 10^{22}$ cm^{-2} (bottom panel) with a simple power-law model (Baumgartner et al. 2013). Bottom left panel: same as the top left panel, but for blazars. The blazars are divided into BL Lacs (BZB), flat-spectrum radio quasars (BZQ), and blazars of uncertain type (BZU). Bottom right panel: same as the top right panel, but for blazars. In all panels the red dashed vertical lines show the median values of the distributions. The median photon indices are listed in Tables 10 and 11 for nonblazar AGNs and blazars, respectively.

Table 14
Intrinsic 2–10 keV Fluxes and Luminosities of the CT Sources of Our Sample

(1) SWIFT ID	(2) F_{2-10} (10^{-12} erg cm^{-2} s^{-1})	(3) logL_{2-10} (erg s^{-1})
SWIFT J0025.8+6818	13.1	42.63
SWIFT J0030.0−5904	7.5	43.16
SWIFT J0105.5−4213	7.1	43.17
SWIFT J0111.4−3808	28.4	42.95
SWIFT J0122.8+5003	10.6	43.00
SWIFT J0128.9−6039	5.9	44.86
SWIFT J0130.0−4218	7.4	43.05
SWIFT J0242.6+0000	76.4	42.39
SWIFT J0250.7+4142	12.0	42.75
SWIFT J0251.3+5441	18.9	42.99

Note. Column (2): intrinsic 2–10 keV fluxes. Column (3): intrinsic 2–10 keV luminosities. Both flux and luminosities were calculated from the intrinsic 14–150 keV values assuming $\Gamma = 1.8$.

(This table is available in its entirety in machine-readable form.)

$\log(N_{\rm H}/{\rm cm}^{-2}) \geqslant 22$ and $\log(N_{\rm H}/{\rm cm}^{-2}) < 22$ are consistent (1.76 ± 0.02 and 1.80 ± 0.02, respectively). The total nonblazar sample has a median of 1.78 ± 0.01, consistent with the value found by Winter et al. (2009a) (see also Alexander et al. 2013). Compton-thin obscured AGNs have significantly lower photon indices ($\Gamma = 1.70 \pm 0.02$) than unobscured objects, while CT AGNs are found to typically have steeper slopes ($\Gamma = 2.05 \pm 0.05$). The distribution of Γ of sources with $\log(N_{\rm H}/{\rm cm}^{-2}) \geqslant 22$ is broader than that of AGNs with $\log(N_{\rm H}/{\rm cm}^{-2}) < 22$, and a Kolmogorov–Smirnov test results in a p-value of $\sim 10^{-4}$, suggesting that the two populations are significantly different. The origin of this difference might be related to the larger fraction of sources with lower 0.3–10 keV counts among the obscured sources, which increases the scatter of Γ, and to the population of CT AGNs with $\Gamma > 2$. A significant difference between sources with $\log(N_{\rm H}/{\rm cm}^{-2}) \geqslant 22$ and $\log(N_{\rm H}/{\rm cm}^{-2}) < 22$ is found for the photon indices obtained by fitting the 14–195 keV *Swift*/BAT spectrum with a simple power-law model ($\Gamma_{\rm BAT}$; top right panel of Figure 17), with

Table 15
Values of Γ_{nEc} and $\Gamma_{0.3-10}$

(1) Source	(2) Γ_{nEc}	(3) $\Gamma_{0.3-10}$
SWIFT J0001.0−0708	$1.86^{+0.26}_{-0.25}$	$1.85^{+0.23}_{-0.32}$
SWIFT J0001.6−7701	$1.96^{+0.60}_{-0.49}$	$1.69^{+0.90}_{-0.42}$
SWIFT J0002.5+0323	$2.22^{+0.07}_{-0.06}$	$2.16^{+0.05}_{-0.05}$
SWIFT J0003.3+2737	$1.41^{+0.53}_{-0.24}$	$1.41^{+0.36}_{-2.23}$
SWIFT J0005.0+7021	$1.93^{+0.42}_{-0.05}$	$1.49^{+0.11}_{-0.10}$
SWIFT J0006.2+2012	$2.83^{+0.20}_{-0.12}$	$2.91^{+0.09}_{-0.11}$
SWIFT J0009.4−0037	$2.19^{+0.86}_{-0.54}$	$1.35^{+0.94}_{-0.89}$
SWIFT J0010.5+1057	$1.73^{+0.04}_{-0.02}$	$1.73^{+0.03}_{-0.06}$
SWIFT J0017.1+8134	...	$1.52^{+0.03}_{-0.03}$
SWIFT J0021.2−1909	$1.69^{+0.23}_{-0.13}$	$1.70^{+0.10}_{-0.24}$

Note. The table lists the values of Γ_{nEc} and $\Gamma_{0.3-10}$
(This table is available in its entirety in machine-readable form.)

unobscured AGNs showing a steeper X-ray spectrum (2.02 ± 0.02) than their $\log(N_H/cm^{-2}) \geqslant 22$ counterparts (1.89 ± 0.02). This is likely related to the fact that Γ_{BAT} is affected by obscuration and that for $\log(N_H/cm^{-2}) \gg 23$ the hard X-ray continuum is flattened by the presence of the reprocessed X-ray radiation emerging from the obscured primary continuum.

To further study the shape of the X-ray continuum, we calculated the photon indices using two alternative approaches. First, we refitted all the nonblazar AGNs of our sample using the same models described in Section 4, fixing the high-energy cutoff to the maximum value allowed ($E_C = 500$ keV), in order to minimize the spectral curvature due to the cutoff. We report the values of the photon index obtained using this approach (Γ_{nEc}) in Table 15. Second, we set $E_C = 500$ keV, excluded the X-ray reprocessed emission,[31] and fitted the data only in the 0.3–10 keV band. This was done using the same best-fitted model obtained from the broadband X-ray spectral analysis, ignoring, besides the high-energy cutoff and the reflection component, also the cross-calibration constant. The photon index obtained with this approach is affected by absorption for objects in which the line-of-sight column density is $N_H \gg 10^{23}$ cm^{-2}, since Compton scattering would significantly deplete the X-ray emission and the relative influence of the reprocessed X-ray emission would be stronger. The values of the photon index obtained following this procedure ($\Gamma_{0.3-10}$) are also reported in Table 15.

In Figure 18 we compare the four different photon indices described above. We consider only objects with $\log(N_H/cm^{-2}) \leqslant 23.5$ since obscuration would most significantly affect $\Gamma_{0.3-10}$ above this value. The top left panel compares Γ with Γ_{BAT} for blazars and nonblazar AGNs. The plot shows that for nonblazar AGNs the values of Γ are typically lower than Γ_{BAT}. This difference is likely due to the presence of a cutoff in the modeling of the primary X-ray continuum, as found by several studies of broadband X-ray emission of AGNs (e.g., Ballantyne et al. 2014; Baloković et al. 2015; Lubiński et al. 2016). In agreement with the idea that a high-energy cutoff is almost ubiquitous in the X-ray spectra of AGNs, we find that the large majority (∼80%) of the objects have $\Gamma_{0.3-10} < \Gamma_{BAT}$ (top right panel). Similarly, also Γ_{nEc} tends to be lower than Γ_{BAT} (middle left panel).

[31] This was done fixing the reflection parameter to $R = 0$ for models A1–A8 and B6 and removing the reflection component for models B1–B5 and B7–B9.

To test how reflection influences the observed value of Γ_{BAT}, we simulated *Swift*/BAT spectra using PEXRAV, setting $\Gamma = 1.9$ and $E_C = 500$ keV and the 14–195 keV flux to (1–2) $\times 10^{-11}$ erg cm^{-2} s^{-1} (consistent with the typical flux of the BAT AGNs of our sample) assuming different values of the reflection parameter. The spectrum was then fitted with a simple power-law model, similar to what has been done for the *Swift*/BAT 70-month catalog. The value of Γ_{BAT} does not increase significantly for larger values of the reflection parameter (left panel of Figure 19). We then carried out similar simulations, fixing the reflection parameter and varying the energy of the cutoff, and found that Γ_{BAT} increases significantly as the energy of the cutoff decreases (right panel of Figure 19). This clearly shows that the steepening of Γ_{BAT} with respect to Γ is due to the presence of a cutoff.

We further find that, for most of our AGNs (both blazars and nonblazar sources), $\Gamma_{0.3-10} \simeq \Gamma$ (middle right panel of Figure 18). For the blazars this is due to the fact that no cutoff or reflection was considered in the fitting, while for the nonblazar AGNs this implies that we are able to recover the intrinsic value of Γ for most objects. The values of Γ_{nEc} are substantially higher than those of Γ (bottom left panel) and $\Gamma_{0.3-10}$ (bottom right panel). In particular, only ∼21% (∼14%) of the objects have $\Gamma_{nEc} < \Gamma$ ($\Gamma_{nEc} < \Gamma_{0.3-10}$). This is due to the fact that, to compensate for the spectral curvature due to the cutoff, the broadband X-ray spectral fit carried out to obtain Γ_{nEc} results in larger values of R and in steeper slopes.

The median value of both Γ and Γ_{BAT} is lower for blazars ($\Gamma = 1.68 \pm 0.04$, $\Gamma_{BAT} = 1.87 \pm 0.06$) than for the nonblazar AGNs (1.78 ± 0.01, 1.96 ± 0.01). The distributions of Γ and Γ_{BAT} are illustrated in the left and right bottom panels of Figure 17, respectively. The X-ray continuum of the flat-spectrum radio quasars is very flat ($\Gamma = 1.54 \pm 0.05$, $\Gamma_{BAT} = 1.71 \pm 0.06$), and it differs significantly from that of BL Lacs, which typically show steeper X-ray emission ($\Gamma = 2.05 \pm 0.06$, $\Gamma_{BAT} = 2.42 \pm 0.10$). These differences in spectral shape are consistent with what has been found by Sambruna et al. (2010), who, combining *Swift*/BAT with *Fermi*/LAT spectra, argued that this behavior (i.e., more luminous blazars are flatter in the hard X-ray band) is in agreement with the so-called "blazar sequence" (e.g., Fossati et al. 1998; Inoue & Totani 2009).

5.2.2. Cross-calibration Constant

As mentioned in Section 4, a cross-calibration constant between the soft X-ray spectra and the 70-month averaged *Swift*/BAT spectra (C_{BAT}) was added to all models. We find that both the obscured and unobscured samples have a median of $C_{BAT} = 1$, consistent with the idea that the 0.3–10 keV observations are randomly sampling the variable flux of the X-ray source. In the top panel of Figure 20 we illustrate the distribution of $\log C_{BAT}$ for objects with $\log(N_H/cm^{-2}) < 22$ (top panel) and $\log(N_H/cm^{-2}) \geqslant 22$ (bottom panel). The standard deviation of $\log C_{BAT}$ for the latter (0.22 dex) is consistent with that of the former (0.21 dex).

The uncertainties on the values of C_{BAT} are typically higher for more obscured objects (with a median of $\Delta C_{BAT} \sim 0.55$) than for those with $\log(N_H/cm^{-2}) < 22$ ($\Delta C_{BAT} \sim 0.45$) and blazars ($\Delta C_{BAT} \sim 0.25$). This difference is likely related to the complexity of the modeling when absorption is present, as well as to the fact that the soft X-ray spectra of the most obscured sources typically have a lower number of counts.

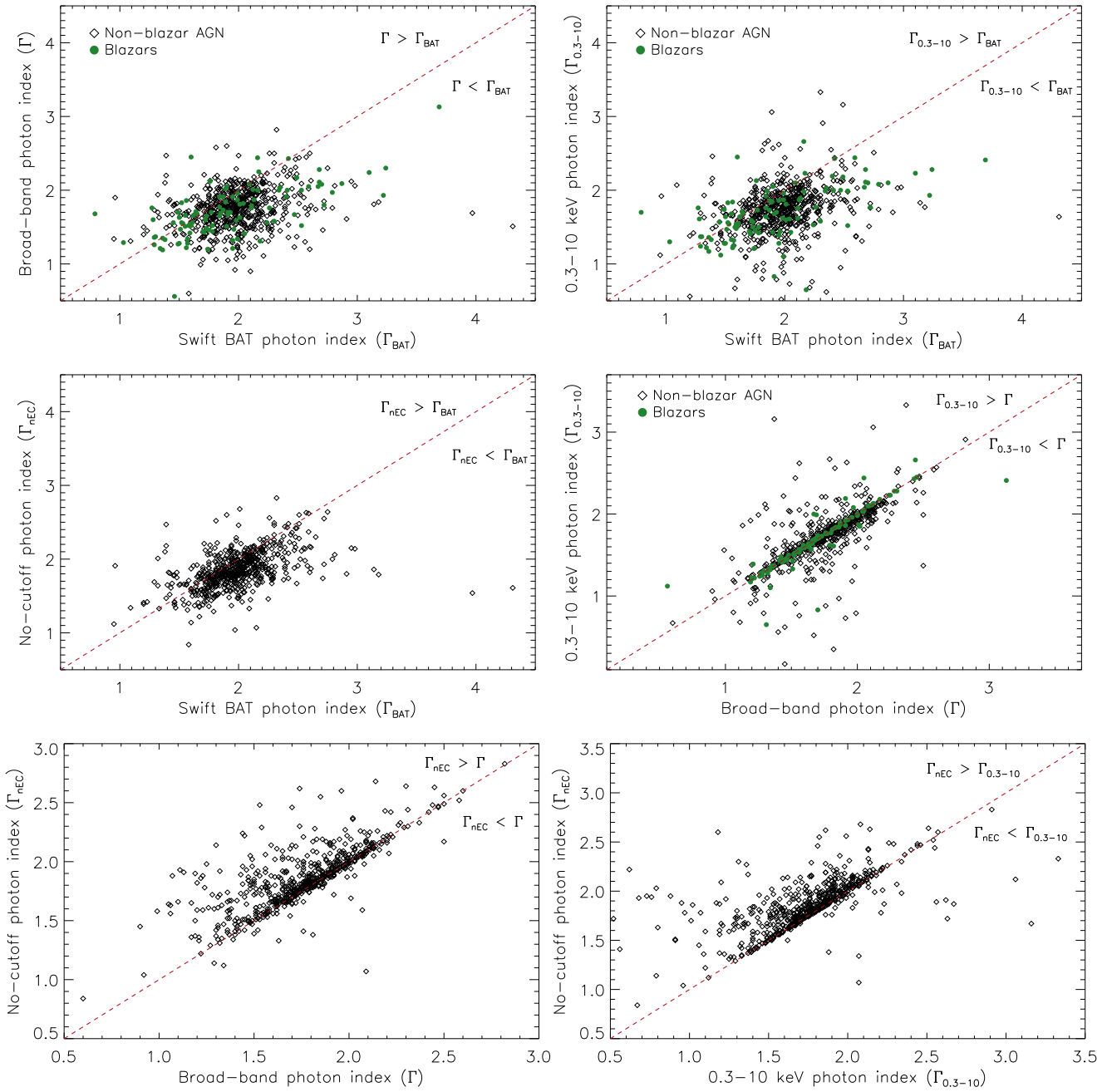

Figure 18. Scatter plot of the photon indices obtained using different approaches for objects with $\log(N_{\rm H}/{\rm cm}^{-2}) \leqslant 23.5$. The values of Γ were inferred from the broadband (0.3–150 keV) X-ray spectral analysis as discussed in Section 4. $\Gamma_{\rm BAT}$ was obtained by fitting the 14–195 keV *Swift*/BAT spectra with a simple power-law model, and values were reported in Baumgartner et al. (2013). We calculated $\Gamma_{\rm nEc}$ by fixing the value of the high-energy cutoff to $E_{\rm C} = 500$ keV, while $\Gamma_{0.3-10}$ was obtained using the best X-ray spectral model for each object, and fitting only the 0.3–10 keV spectra fixing $E_{\rm C} = 500$ keV while setting the reflection parameter to $R = 0$ (i.e., no reflection). The plot shows the values of Γ, $\Gamma_{\rm BAT}$, and $\Gamma_{0.3-10}$ for blazars and nonblazar AGNs. For $\Gamma_{\rm nEc}$ we only show the nonblazar AGNs, since no high-energy cutoff was considered when fitting blazars (with the few exceptions reported in Section 4).

The standard deviation found for the whole sample of nonblazar AGNs ($\sigma \simeq 0.22$ dex) is similar to the dispersion obtained comparing L_{2-10}(obs) to L_{2-10} (0.3 dex; Figure 15). The difference between these two values (0.22 and 0.3 dex) could be related to differences in the spectral shape of the X-ray continuum, which would increase the dispersion of L_{2-10}(obs) versus L_{2-10}, as discussed in Section 5.1. Studying a sample of 45 Compton-thin obscured *Swift*/BAT AGNs with *Suzaku*, Kawamuro et al. (2016a) found a dispersion in $C_{\rm BAT}$ of 0.21 dex, which is consistent with the value obtained here. This confirms that with our spectral analysis we are able to quantify the intrinsic variability of the X-ray source and that, on the timescales probed by our study (days to several years), the X-ray variability of nonblazar AGNs is ∼0.2 dex.

While the median value of blazars is also consistent with 1 ($C_{\rm BAT} = 1.00 \pm 0.35$; bottom panel of Figure 20), it has a larger scatter ($\sigma \simeq 0.3$ dex) than for the nonblazar AGNs, consistent with the stronger variability of these objects, observed across the entire electromagnetic spectrum (e.g., Ulrich et al. 1997). The number of blazars with $C_{\rm BAT} > 2$ (10)

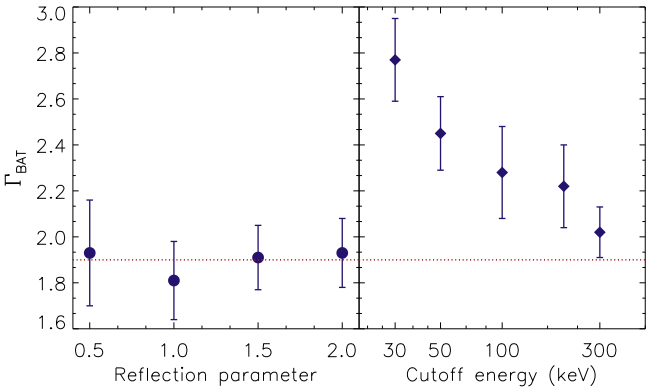

Figure 19. Left panel: photon index obtained by fitting with a power-law model simulated *Swift*/BAT spectra (setting $\Gamma = 1.9$ and $E_C = 500$ keV and the 14–195 keV flux to (1–2) $\times$ 10^{-11} erg cm^{-2} s^{-1}) assuming different values of the reflection parameter. The red dotted line shows the correct value of photon index of the primary X-ray continuum. Right panel: same as left panel, setting $\Gamma = 1.9$ and $R = 0.5$ and varying the values of the high-energy cutoff. The plot shows that decreasing values of the high-energy cutoff lead to the increase of the *Swift*/BAT photon index, while values of the reflection parameter do not typically affect significantly Γ_{BAT}. Exposure times in the simulations were set to 9.5 $\times$ 10^6 s, consistent with the exposure of ~50% of the sky for the 70-month *Swift*/BAT catalog.

is larger than that of objects of the same class with $C_{BAT} < 0.5$ (5). This is likely related to the fact that several soft X-ray observations of the blazars in our sample have been triggered by the object being in a bright state (e.g., Stroh & Falcone 2013).

5.2.3. High-energy Cutoff

The distributions of the cutoff energies for the nonblazar AGNs of our sample are shown in the left panel of Figure 21. For 418 (7) sources only a lower (upper) limit of E_C could be obtained. As expected, most of the 161 sources for which it was possible to constrain E_C have values $E_C \lesssim 100$ keV, i.e., within the energy range covered by our spectral analysis, and a median value of $E_C = 76 \pm 6$ keV. We found that AGNs with $\log(N_H/\mathrm{cm}^{-2}) < 22$ and those with $\log(N_H/\mathrm{cm}^{-2}) \geqslant 22$ have consistent median cutoff energies (80 ± 7 keV and 74 ± 11 keV, respectively). The eight CT AGNs for which E_C could be constrained have a median of 43 ± 15 keV, lower than Compton-thin and unobscured objects. This is probably due to the fact that PEXRAV fails to identify the curvature of the spectra of these heavily obscured objects as reprocessed emission and associates it with an X-ray continuum with a low cutoff energy, confirming the importance of using physical torus models to study CT AGNs. We find that the mean of our sample is $E_C = 90 \pm 5$ keV, with a standard deviation of $\sigma = 61$ keV. This is lower than the value found by Malizia et al. (2014) studying the broadband X-ray spectra of a sample of 41 type I AGNs ($E_C = 128$ keV, $\sigma = 46$ keV). We compared the values of the cutoff energy obtained by our study with those found by the analysis of *NuSTAR* observations (Marinucci et al. 2016; Tortosa et al. 2017 and references therein) and found that the values are roughly in agreement (Figure 22), with the exception of NGC 5506, for which the energy of the cutoff found by *NuSTAR* (720^{+130}_{-190} keV; Matt et al. 2015) is significantly higher than that inferred using *Swift*/BAT (127^{+21}_{-15} keV). For two of the objects reported by Marinucci et al. (2016), 3C 382 (Ballantyne et al. 2014) and

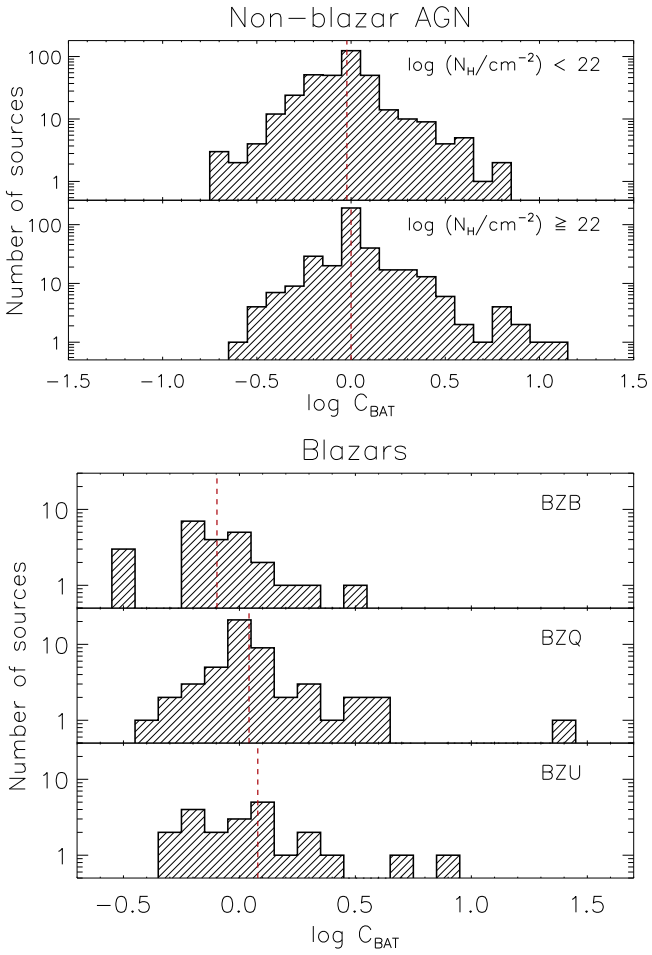

Figure 20. Top panel: distribution of the cross-calibration (C_{BAT}) constants obtained by our spectral analysis for the nonblazar AGNs of our sample. The sample is divided into objects with $\log(N_H/\mathrm{cm}^{-2}) < 22$ (top panel) and $\log(N_H/\mathrm{cm}^{-2}) \geqslant 22$ (bottom panel). Bottom panel: same as the top panel, but for the blazars. The blazars are divided into BL Lacs (BZB), flat-spectrum radio quasars (BZQ), and blazars of uncertain type (BZU). The median values of C_{BAT} are listed in Tables 10 and 11 for nonblazar and blazars, respectively. The dispersion in C_{BAT} shows the typical X-ray variability on the timescales probed here (days to several years).

Fairall 9 (Fabian et al. 2015), the data did not allow us to constrain the energy of the cutoff.

Since for most of the sources of our sample we could only obtain lower and upper limits on the energy of the cutoff, the median and mean values reported above are not representative of the whole sample of *Swift*/BAT AGNs. To better constrain the median of the sample, including also upper and lower limits, we performed 10,000 Monte Carlo simulations for each value of E_C. For each simulation we used the following approach: (i) the values of E_C of the detections were substituted with values randomly selected from a Gaussian distribution centered on the best-fit value, with the standard deviation given by its uncertainty; (ii) the upper limits U were substituted with a random value from a uniform distribution in the interval $[0, U]$; and (iii) the lower limits L were substituted with a value randomly selected from a uniform distribution in the interval $[L, 1000]$. In the last step we assumed that the maximum value of the cutoff energy is 1000 keV. For each Monte Carlo run we calculated the median of all values and then used the mean of the 10,000 simulations. The values obtained are reported in Table 10. We find that the whole sample has a median cutoff

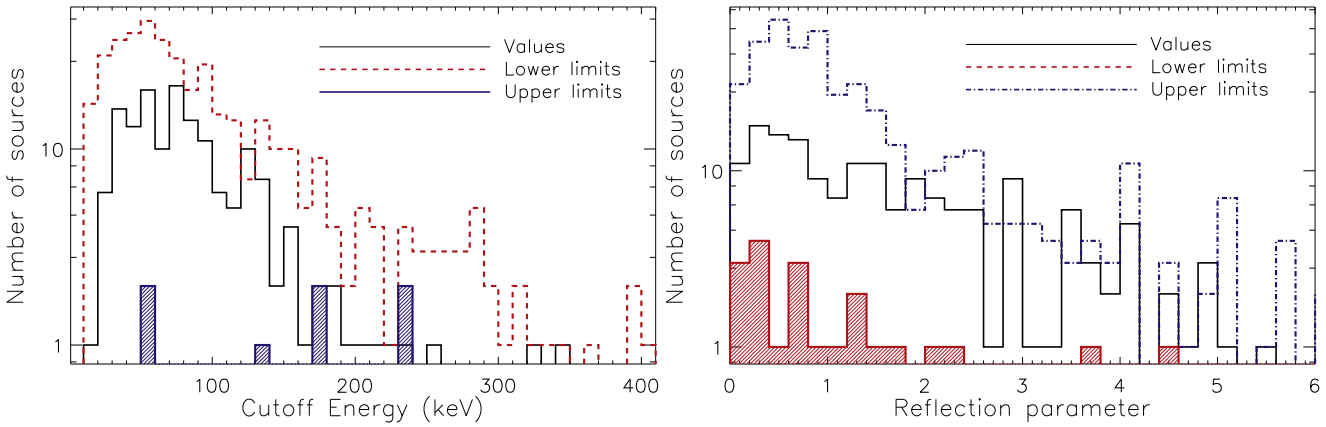

Figure 21. Left panel: distribution of the cutoff energies for the nonblazar AGNs. The plot shows the values (black solid histogram), the lower limits (red dashed histogram), and the upper limits (blue double-dot-dashed histogram). Right panel: distribution of the reflection parameters for the nonblazar AGNs. The plot shows the values (black solid histogram), the lower limits (red dashed histogram), and the upper limits (blue dot-dashed histogram). The median values of E_C and R are listed in Table 10.

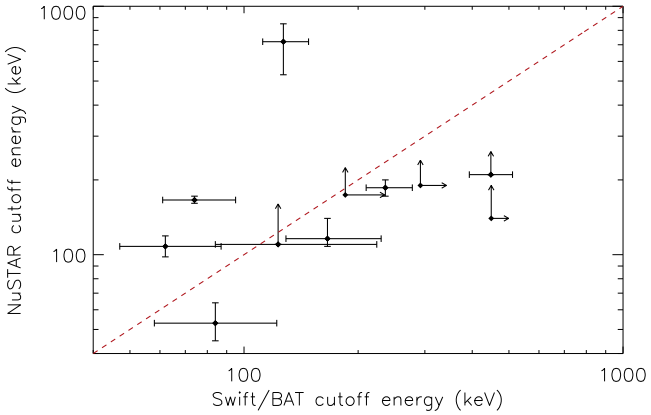

Figure 22. Values of the cutoff energy obtained with *NuSTAR* (from Marinucci et al. 2016) vs. the values obtained by our analysis using *Swift*/BAT for the same objects. The objects reported in the plot are Ark 120 (Matt et al. 2014), Mrk 335 (Parker et al. 2014), NGC 7213 (Ursini et al. 2015), 3C 390.3 (Fabian et al. 2015), IC 4329A (Brenneman et al. 2014), NGC 5506 (Matt et al. 2015), SWIFT J2127.4+5654 (Marinucci et al. 2014a), MCG −05−23−016 (Balokovíć et al. 2015), MCG−06−30−015 (Marinucci et al. 2014b), NGC 2110 (Marinucci et al. 2015), and SWIFT J1737.5−2908 (Tortosa et al. 2017). The red dashed line illustrates the scenario in which the two energies are the same. The plot shows that the values of the high-energy cutoff are roughly in agreement, with the exception of NGC 5506, for which the energy of the cutoff found by *NuSTAR* is significantly higher than that inferred using *Swift*/BAT.

energy of $E_C = 381 \pm 16$ keV, and the value of AGNs with $\log(N_H/cm^{-2}) < 22$ (384 ± 21 keV) is consistent with that of objects with $\log(N_H/cm^{-2}) = 22$–24 (386 ± 25 keV) and with the one obtained for CT AGNs (341 ± 70 keV). Considering a maximum cutoff energy of 500 keV (800 keV), we obtain, for the total sample, a median of $E_C = 244 \pm 8$ keV (332 ± 12 keV). These values are in good agreement with what was obtained by Ballantyne (2014) ($E_C = 270^{+170}_{-80}$ keV) fitting the X-ray luminosity function of local AGNs in four energy bands.

To further test the typical values of the cutoff energy and avoid issues related to the choice of the maximum cutoff energy, we also calculated the mean and median using the Kaplan–Meier estimator and including the lower limits (see Section 5 of Shimizu et al. 2016, for details). We found that, for the whole sample, the median (mean) is 200 ± 29 keV (319 ± 23 keV), while for unobscured AGNs it is 210 ± 36 keV (331 ± 29 keV). For objects with $\log(N_H/cm^{-2}) = 22$–24 the median (mean) is 188 ± 27 keV (262 ± 22 keV), and for CT AGNs it is 449 ± 64 keV (272 ± 51 keV).

5.2.4. Reflection

The distributions of the reflection parameters (R) are shown in the right panel of Figure 21. We could constrain R for 170 objects, while for 490 we obtain an upper limit and for 23 a lower limit. The median value of R among the sources for which the parameter could be constrained is $R = 1.3 \pm 0.1$. It should be noted that this value does not correspond to the *intrinsic* median of hard-X-ray-selected AGNs, since it is typically easier to infer this parameter when its value is large. We found that 51 objects have values of $R > 2$, albeit most of them have large uncertainties (the median fractional error is ∼70%), and only 16 are consistent with $R \geqslant 2$ within their respective uncertainties. Most of the objects (35) with $R \geqslant 2$ are unobscured AGNs. This might lend support to the idea that this enhanced fraction of reprocessed flux with respect to the primary X-ray emission is caused by relativistic reflection, as predicted by the light-bending scenario (e.g., Miniutti & Fabian 2004).

We took into account the upper and lower limits on R following the same approach used for E_C (Section 5.2.3). In this case, however, we allowed the lower limits to vary in the range [L, 10] i.e., we assumed a maximum value of $R = 10$. We find that the median of the whole sample is $R = 0.53 \pm 0.09$. AGNs with $\log(N_H/cm^{-2}) < 22$ typically have larger reflection parameters ($R = 0.83 \pm 0.14$) than those with $\log(N_H/cm^{-2}) \geqslant 22$ ($R = 0.37 \pm 0.11$). We also find that CT AGNs have significantly lower intensity of the reprocessed X-ray continuum relative to the primary X-ray luminosity ($R = 0.15 \pm 0.12$). The decrease of the reflection component with increasing obscuration would be in agreement with the idea that most of the reprocessing in AGNs is due to the accretion disk, so that objects observed pole-on are able to see more of the reprocessed radiation than those observed edge-on. Our results are in disagreement with what was found by Ricci et al. (2011) stacking *INTEGRAL* IBIS/ISGRI spectra and with the results of Vasudevan et al. (2013b) and Esposito & Walter (2016) obtained by stacking *Swift*/BAT spectra. All these works in fact showed that the stacked spectra of obscured AGNs tend to have more reflection than those of their less obscured counterparts. Similar results were also obtained by

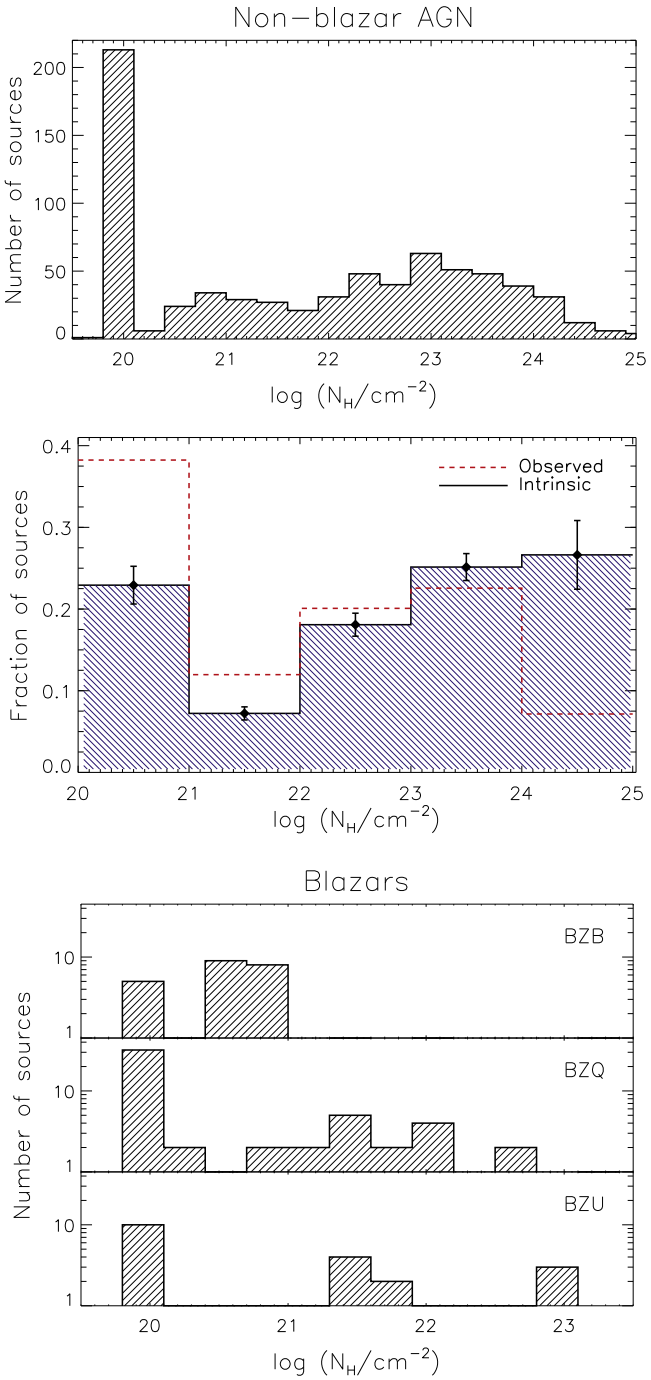

Figure 23. Top panel: distribution of the line-of-sight column density for the nonblazar AGNs. Sources that do not show any sign of obscuration were arbitrarily assigned $\log(N_{\rm H}/{\rm cm}^{-2}) = 20$ for visual clarity. Middle panel: observed (red dashed line) and intrinsic (black solid line; from Ricci et al. 2015) column density distribution of nonblazar AGNs. Bottom panel: same as the top panel, but for blazars. The sources were divided into BL Lacs (BZB), flat-spectrum radio quasars (BZQ), and blazars of uncertain type (BZU). The median values of $N_{\rm H}$ are listed in Tables 10 and 11 for nonblazar AGNs and blazars, respectively.

stacking *XMM-Newton* data by Corral et al. (2011). While the origin of this difference is still not clear, a possible explanation could be that the stacking of spectra with different column densities would artificially produce the curvature observed in the averaged spectrum.

5.3. Absorption Properties

5.3.1. Neutral Absorption

A total of 366 nonblazar AGNs in our sample have $\log(N_{\rm H}/{\rm cm}^{-2}) \geqslant 22$, while 365 have $\log(N_{\rm H}/{\rm cm}^{-2}) < 22$ (top and middle panels of Figure 23). Among the blazars, only 13 sources are obscured, while the remaining 92 objects are unobscured (bottom panel of Figure 23). The difference between the column density distributions of blazars and nonblazar AGNs could be related to (i) the very strong radiation field of the former; (ii) the fact that in blazars a significant fraction of the X-ray emission is emitted by the jet, which implies that the region producing X-ray radiation is more extended and hence more difficult to significantly obscure in blazars than in nonblazar AGNs; or (iii) the fact that blazars are observed pole-on and therefore it is less likely for the X-ray source to be obscured by the torus.

In Figure 24 we show the redshift (left panel) and distance (right panel) distribution of nonblazar AGNs, divided according to their line-of-sight column density into unobscured (top panel), obscured Compton-thin (middle panel), and CT (bottom panel). The fact that obscured Compton-thin AGNs (middle panel) have a lower median redshift ($z = 0.033$) than the unobscured AGNs ($z = 0.047$) is related to the difference in their luminosity distributions (see Section 5.1 for discussion), while the lower redshift of CT AGNs ($z = 0.017$) is instead due to the influence of obscuration, which allows us to detect only the nearest objects of this class (see Figure 3 of Ricci et al. 2015).

In Figure 25 we illustrate the ratio between the observed fluxes in the 2–10 keV and 14–195 keV bands ($F^{\rm obs}_{2-10}/F^{\rm obs}_{14-195}$) versus the column density. Due to the very different impact of absorption in these two bands, we expect that, as the line-of-sight column density increases, $F^{\rm obs}_{2-10}/F^{\rm obs}_{14-195}$ would decrease. For $N_{\rm H} \geqslant 10^{23.5}\,{\rm cm}^{-2}$ absorption plays a significant role also in the 14–195 keV band, so that the trend is expected to flatten. The plot shows a clear decrease of $F^{\rm obs}_{2-10}/F^{\rm obs}_{14-195}$ for $\log(N_{\rm H}/{\rm cm}^{-2}) \gtrsim 22$. In particular, ∼90% of the nonblazar AGNs for which $F^{\rm obs}_{2-10}/F^{\rm obs}_{14-195} < 0.1$ have $N_{\rm H} > 10^{23}\,{\rm cm}^{-2}$. For flux ratios of $F^{\rm obs}_{2-10}/F^{\rm obs}_{14-195} < 0.03$, ∼94% of the AGNs are CT.

However, we identify a few exceptions to this general trend. Two AGNs with $\log(N_{\rm H}/{\rm cm}^{-2}) \geqslant 24$ have $F^{\rm obs}_{2-10}/F^{\rm obs}_{14-195} > 0.11$, both of which are well-known CT AGNs: ESO 138−G001 ($F^{\rm obs}_{2-10}/F^{\rm obs}_{14-195} = 0.113$; e.g., Piconcelli et al. 2011) and NGC 1068 ($F^{\rm obs}_{2-10}/F^{\rm obs}_{14-195} = 0.14$; e.g., Bauer et al. 2015). These two objects are among the most obscured of our sample, and the 14–195 keV flux is also strongly affected by absorption, which naturally leads to a higher value of $F^{\rm obs}_{2-10}/F^{\rm obs}_{14-195}$ with respect to the transmission-dominated CT AGNs. In Figure 25 we also illustrate that for most sources $F^{\rm obs}_{2-10}/F^{\rm obs}_{14-195}$ is consistent with the expected flux ratios. These theoretical values were obtained using two different spectral models: the torus model of Brightman & Nandra (2011; red dashed lines) and MYTorus (Murphy & Yaqoob 2009; black dotted lines). The expected $F^{\rm obs}_{2-10}/F^{\rm obs}_{14-195}$ were calculated considering the maximum value of the inclination angle allowed by the models, a half-opening angle of 60° for the torus model of Brightman & Nandra (2011), and two different values of the photon index ($\Gamma = 1.5$ and $\Gamma = 2.5$). We added to the models a scattered power-law component with $f_{\rm scatt} = 1\%$, consistent with the typical value found for *Swift*/BAT AGNs (see Section 5.4.2).

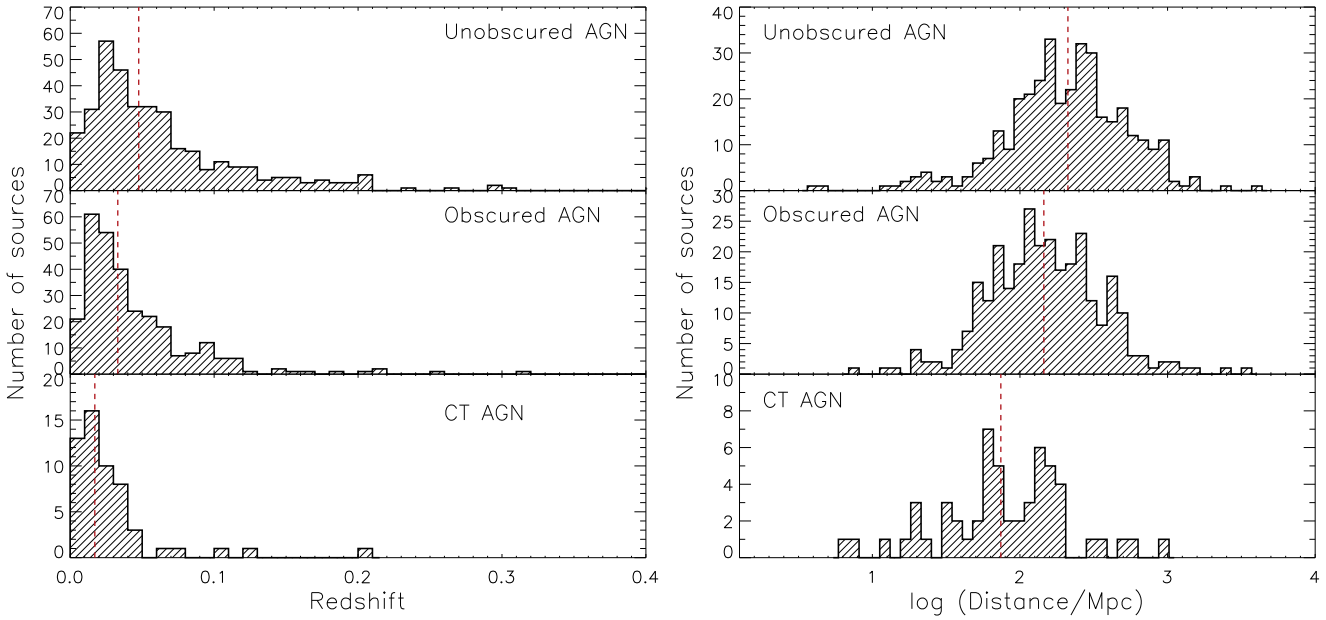

Figure 24. Distribution of the spectroscopic redshifts (left panels) and distances (right panels) of nonblazar AGNs divided according to their line-of-sight column density: unobscured (top panels; $N_{\rm H} < 10^{22}$ cm^{-2}), obscured Compton-thin (middle panels; $10^{22} < N_{\rm H} < 10^{24}$ cm^{-2}), and CT (bottom panels; $N_{\rm H} \geqslant 10^{24}$ cm^{-2}). The red dashed lines show the median values of the redshift for the three subsamples. The plots are zoomed in on the $z = 0$–0.4 range, similarly to Figure 2. The fact that obscured Compton-thin AGNs (middle panel) have a lower median redshift and distance ($z = 0.033$, $D = 145.2$ Mpc) than the unobscured AGNs ($z = 0.047$, $D = 211.3$ Mpc) is related to the difference in their luminosity distributions (see Section 5.1 for discussion). The lower redshift and distance of CT AGNs ($z = 0.017$, $D = 74.2$ Mpc) are instead due to the influence of obscuration, which allows us to detect only the nearest objects of this class (see Figure 3 of Ricci et al. 2015).

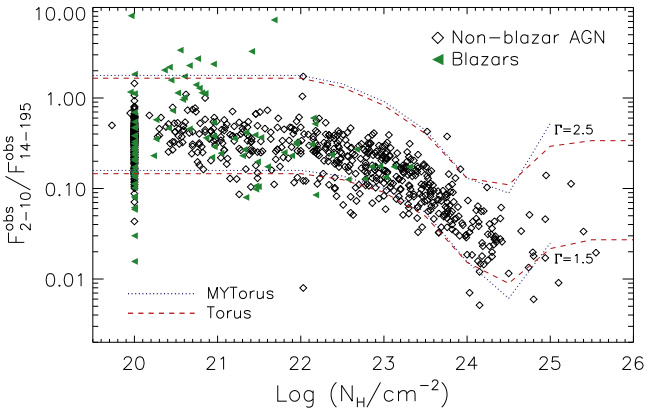

Figure 25. Ratio of the observed 2–10 keV and 14–195 keV flux vs. the column density inferred from the broadband X-ray spectral analysis for the nonblazar AGNs (black diamonds) and the blazars (green triangles). The plot shows the clear decrease of the $F^{\rm obs}_{2-10}/F^{\rm obs}_{14-150}$ flux ratio for $\log(N_{\rm H}/{\rm cm}^{-2}) > 22$ owing to the stronger effect of absorption below 10 keV. The black dotted and red dashed lines represent the expected flux ratios (for $\Gamma = 1.5$ and $\Gamma = 2.5$) obtained considering the MYTorus model and the torus model of Brightman & Nandra (2011), respectively.

The only Compton-thin object with a very low flux ratio ($F^{\rm obs}_{2-10}/F^{\rm obs}_{14-195} < 0.01$) is UGC 12243. This source requires a very large cross-calibration constant ($C_{\rm BAT} = 11.8^{+22}_{-3.4}$), which could be due to extreme variability, with the source being in a very low flux state at the time of the *XMM-Newton* observation.

While for most sources we consider only a single layer of neutral obscuring material, the unabsorbed power-law component used in our analysis to reproduce the scattered emission allows us to account also for partially covering obscuration of the X-ray source. Typically, the values of $f_{\rm scatt}$ of optically selected AGNs are of the order of ∼1%–5% (e.g., Bianchi & Guainazzi 2007), so that values considerably larger than this might imply the contribution of some leaked primary X-ray continuum. In our sample we find that a total of 22 (40) nonblazar AGNs have $f_{\rm scatt} \geqslant 10\%$ (⩾5%). Alternative explanations for the significant contribution of an unobscured component at low energies include the presence of strong star formation or a jet component dominating the X-ray emission below ∼2–3 keV. This has been found to be the case for radio galaxies (Hardcastle et al. 2006, 2009), which very often show additional unobscured power-law emission. In agreement with this, we find that several of the objects with $f_{\rm scatt} \geqslant 10\%$ are radio loud, such as Cygnus A ($f_{\rm scatt} = 13.3\%$) and 4C +21.55 (30.6%). Three out of the six blazars for which a scattered component was added to the X-ray spectrum also show $f_{\rm scatt} \geqslant 5\%$. For three objects, SWIFT J0552.2−0727 (NGC 2110),[32] SWIFT J2124.6+5057 (4C 50.55),[33] and SWIFT J2223.9−0207 (3C 445),[34] we find that two layers of partially covering neutral material are needed to reproduce the X-ray spectrum. For these sources the values of the column density reported in Table 5 are the sum of the different components multiplied by the covering factor (as noted in Section 4.2).

[32] For NGC 2110 the two absorbers have column densities of $N^1_{\rm H} = 17.9^{+1.6}_{-1.5} \times 10^{22}$ cm^{-2} and $N^2_{\rm H} = 2.70^{+0.03}_{-0.03} \times 10^{22}$ cm^{-2} and cover $f^1_{\rm cov} = 34.5^{+0.9}_{-0.9}\%$ and $f^2_{\rm cov} = 95.3^{+0.5}_{-0.4}\%$ of the X-ray source, respectively. An additional, fully covering absorber with a column density of $N_{\rm H} = 1.0^{+0.1}_{-0.1} \times 10^{21}$ cm^{-2} is required to well reproduce the data.

[33] For 4C 50.55 the absorbers have column densities of $N^1_{\rm H} = 2.2^{+0.1}_{-0.2} \times 10^{22}$ cm^{-2} and $N^2_{\rm H} = 20^{+3}_{-4} \times 10^{22}$ cm^{-2}, covering $f^1_{\rm cov} = 92^{+1}_{-1}\%$ and $f^2_{\rm cov} = 43^{+2}_{-6}\%$ of the X-ray source, respectively.

[34] For 3C 445 the two absorbers have column densities of $N^1_{\rm H} = 34^{+7}_{-6} \times 10^{22}$ cm^{-2} and $N^2_{\rm H} = 6.7^{+1.4}_{-1.2} \times 10^{22}$ cm^{-2}, covering $f^1_{\rm cov} = 83^{+4}_{-5}\%$ and $f^2_{\rm cov} = 98.3^{+0.5}_{-0.4}\%$ of the X-ray source, respectively.

To better constrain the column density, the 75 objects with values of $N_{\rm H}$ consistent with $10^{24}\,{\rm cm}^{-2}$ within their 90% confidence interval were fitted with the torus model of Brightman & Nandra (2011) (see Table 9 for the parameters obtained by the spectral fitting). With this approach we found that 55 *Swift*/BAT AGNs are CT (Ricci et al. 2015), of which 26 were identified as CT candidates for the first time. A similar study was recently carried out by Akylas et al. (2016), who found 53 CT AGNs, confirming the CT nature of most of our candidates. The two objects reported by Akylas et al. (2016) as CT but not listed in Ricci et al. (2015) are NGC 4941 and NGC 3081. Both of these sources have column densities that are either consistent with being CT or heavily obscured. From our analysis we find that NGC 4941 has a line-of-sight column density of $\log(N_{\rm H}/{\rm cm}^{-2}) = 23.91$ and the 90% confidence interval is $\log(N_{\rm H}/{\rm cm}^{-2}) = 23.81$–$24.00$. NGC 3081 is also found to be heavily obscured ($\log(N_{\rm H}/{\rm cm}^{-2}) = 23.91$), with a 90% confidence interval of $\log(N_{\rm H}/{\rm cm}^{-2}) = 23.87$–$23.95$. The fact that these two AGNs are heavily obscured is supported also by the very large EW of their Fe Kα features: 340^{+87}_{-17} eV and 304^{+33}_{-18} eV for NGC 4941 and NGC 3081, respectively. In Ricci et al. (2015) we did not report SWIFT J0025.8+6818 (2MASX J00253292+6821442) as CT, since the analysis of the combined *Swift*/BAT and the XRT spectra resulted in a column density consistent with CT within the 90% confidence interval, but with the best-fit value below the threshold ($7.8^{+5.4}_{-4.5} \times 10^{23}\,{\rm cm}^{-2}$ and $6.8^{+7.4}_{-1.7} \times 10^{23}\,{\rm cm}^{-2}$ for the phenomenological and torus model, respectively). However, the analysis of the combined *Chandra* and *Swift*/BAT spectra, carried out with the torus model, confirms that this source is CT, with a column density of $1.4^{+0.7}_{-0.9} \times 10^{24}\,{\rm cm}^{-2}$. The large EW of the Fe Kα (836^{+595}_{-778} eV) also strongly supports the idea that this source is CT.

In the top panel of Figure 26 we compare the column density obtained using the PEXRAV model versus that inferred from the torus model. There is a good agreement between the two values of $N_{\rm H}$ up to $\log(N_{\rm H}/{\rm cm}^{-2}) \simeq 24.3$. Around $\log(N_{\rm H}/{\rm cm}^{-2}) \simeq 24.5$ the column densities obtained with the torus model become typically larger (five out of seven objects). Performing a linear fit of the form $\log N_{\rm H}({\rm Torus}) = \alpha \times \log N_{\rm H}({\rm Pexrav}) + \beta$, we found a slope of $\alpha = 1.17 \pm 0.10$. The fact that $\alpha > 1$ is due to the difficulty of constraining column densities with PEXRAV for $\log(N_{\rm H}/{\rm cm}^{-2}) \gtrsim 24.5$, since for these levels of obscuration most of the primary X-ray emission is depleted by absorption and the source is reflection dominated. Using torus models, on the other hand, it is possible to employ the shape of the reprocessed emission, as well as that of the absorbed primary X-ray emission, to infer the column density. In the middle panel of Figure 26 we show the values of Γ obtained by the two models. The plot shows that the slopes inferred by the torus model tend to be steeper than those obtained with the phenomenological model (i.e., using PEXRAV). In particular, $\sim$72% of the sources have $\Gamma({\rm Torus}) > \Gamma({\rm Pexrav})$. This shows the importance of self-consistently taking into account absorbed and reprocessed X-ray emission in the most obscured AGNs. The absorption-corrected fluxes obtained with PEXRAV and the torus model in the 2–10 keV and 14–150 keV energy ranges are illustrated in the bottom panel of Figure 26. The plot shows that the dispersion between the fluxes obtained with the two models is lower in the 14–150 keV than in the 2–10 keV band. This is a straightforward consequence of the fact that the corrections are smaller in the 14–150 keV band.

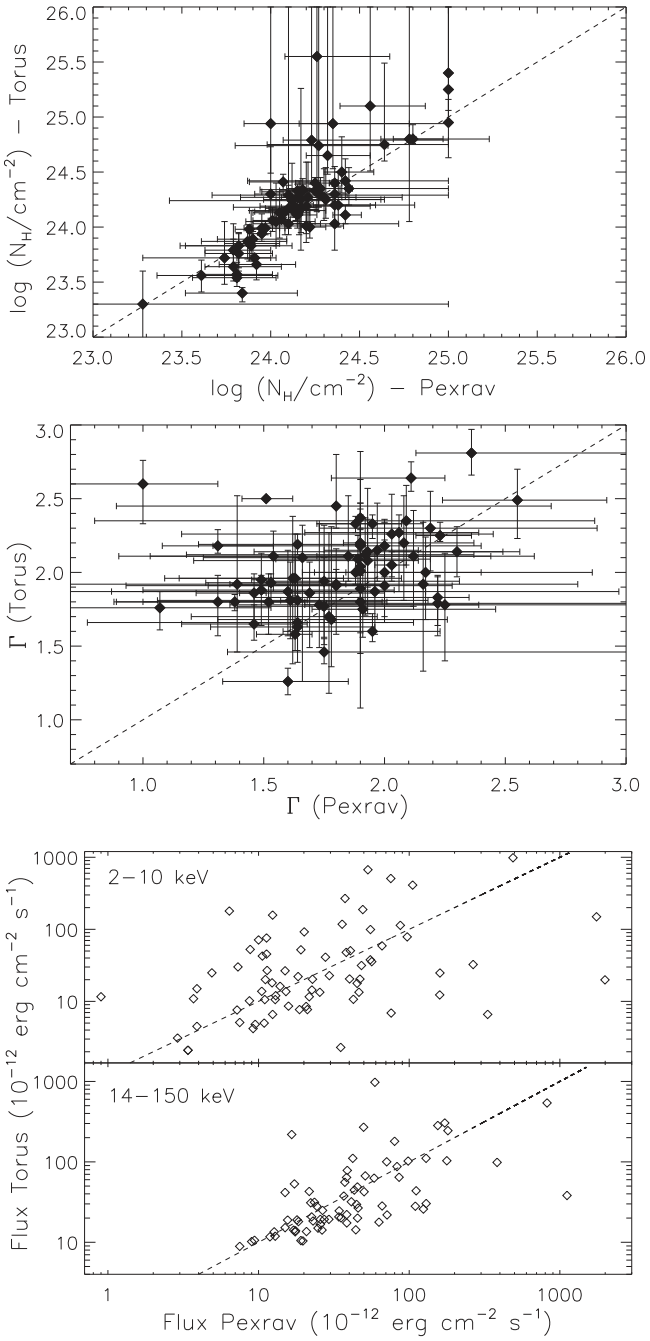

Figure 26. Top panel: scatter plot of the values of the column density obtained by fitting the 75 most obscured objects of our sample (i.e., all those with column densities consistent with $10^{24}\,{\rm cm}^{-2}$ within their 90% confidence intervals) using PEXRAV and the torus model of Brightman & Nandra (2011). The dashed line shows the 1:1 relation between the two values of $N_{\rm H}$. Middle panel: same as the top panel, but for the photon index of the primary X-ray continuum (Γ). Bottom panel: same as the top panel, but for the absorption-corrected flux in the 2–10 keV and 14–150 keV energy ranges. The plots show that PEXRAV tends to underestimate $N_{\rm H}$ (for $\log(N_{\rm H}/{\rm cm}^{-2}) \gtrsim 24.3$) and Γ with respect to torus models.

The distribution of the half-opening angle of the torus obtained by our analysis is illustrated in Figure 27. For most of the objects (28) we could not constrain $\theta_{\rm OA}$, while for 18 (17) we are only able to infer an upper (lower) limit. For the 12 objects for which we could constrain $\theta_{\rm OA}$ we find a median

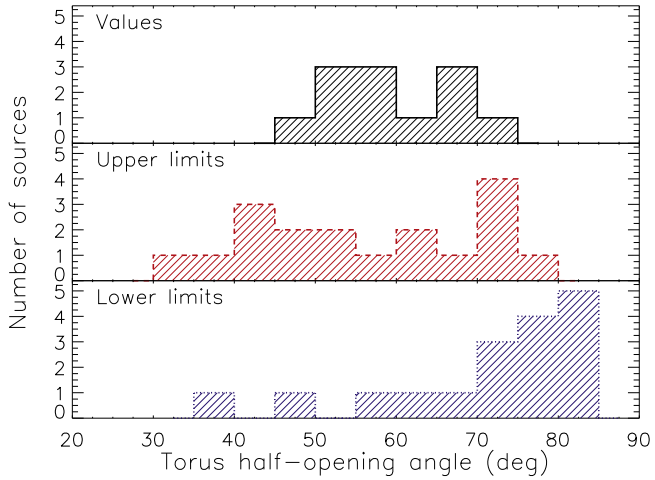

Figure 27. Distribution of the half-opening angle of the torus obtained by fitting with the torus model of Brightman & Nandra (2011) the broadband X-ray spectra of the objects with column densities consistent with $\log(N_{\rm H}/{\rm cm}^{-2}) = 24$ within their 90% uncertainties. The plot shows the values (top panels), upper limits (middle panel), and lower limits (bottom panel).

value of $58^\circ \pm 3^\circ$. A detailed study of the obscuration properties of *Swift*/BAT AGNs is Ricci et al. (2017c), where we discuss how absorption is related to the physical characteristics of the accreting SMBH.

5.3.2. Ionized Absorption

Ionized absorption has been found to be a common characteristic of unobscured AGNs. Early studies carried out with *ASCA* found evidence of O VII and O VIII absorption edges in ∼50% of the sources (e.g., Reynolds 1997; George et al. 1998). More recent studies, carried out using *Suzaku*, *XMM-Newton*, and *Chandra*, have confirmed the presence of these warm absorbers, showing that they are related to outflows (e.g., Kaastra et al. 2000; Kaspi et al. 2000) with velocities of the order of 100–1000 km s^{-1} (e.g., Tombesi et al. 2013 and references therein). The analysis of high-quality *Suzaku* and *XMM-Newton* spectra has additionally pointed out that some objects also show highly ionized outflows with velocities exceeding 10,000 km s^{-1}, the so-called ultrafast outflows (e.g., Tombesi et al. 2010a, 2010b; Gofford et al. 2013).

Evidence of ionized absorption was found in 86 AGNs in our sample. Of these, five are blazars, one is an obscured AGN (NGC 1365), and the remaining 80 are unobscured AGNs. This implies that, on average, the covering factor of the warm absorbers in nonblazar unobscured AGNs is $\gtrsim$22%. This can be used only as a lower limit, since we might be missing ionized absorbers in objects for which high-quality X-ray spectra are not available. Eleven nonblazar AGNs and two blazars require two ionized absorbers to well reproduce the 0.3–10 keV spectra.

In Figure 28 we show the distribution of the column density (top panel), the ionization parameter (middle panel), and the covering factor (lower panel) of the warm absorbers. We find that the median column density is $N_{\rm H}^{\rm W} = 2.8 \times 10^{22}$ cm^{-2}. The median value of the ionization parameter (covering factor), for the objects for which we could constrain the values, is $\log[\xi/(\,{\rm erg\ cm\ s}^{-1})] = 1.45$ ($f_{\rm cov}^{\rm W} = 63\%$). These values are in good agreement with what was found by previous studies of warm absorbers (e.g., Tombesi et al. 2013 and references therein). A more detailed study of the properties of ionized absorption and on the relation between the warm absorbers and the physical properties of the accreting SMBH will be discussed in a forthcoming paper.

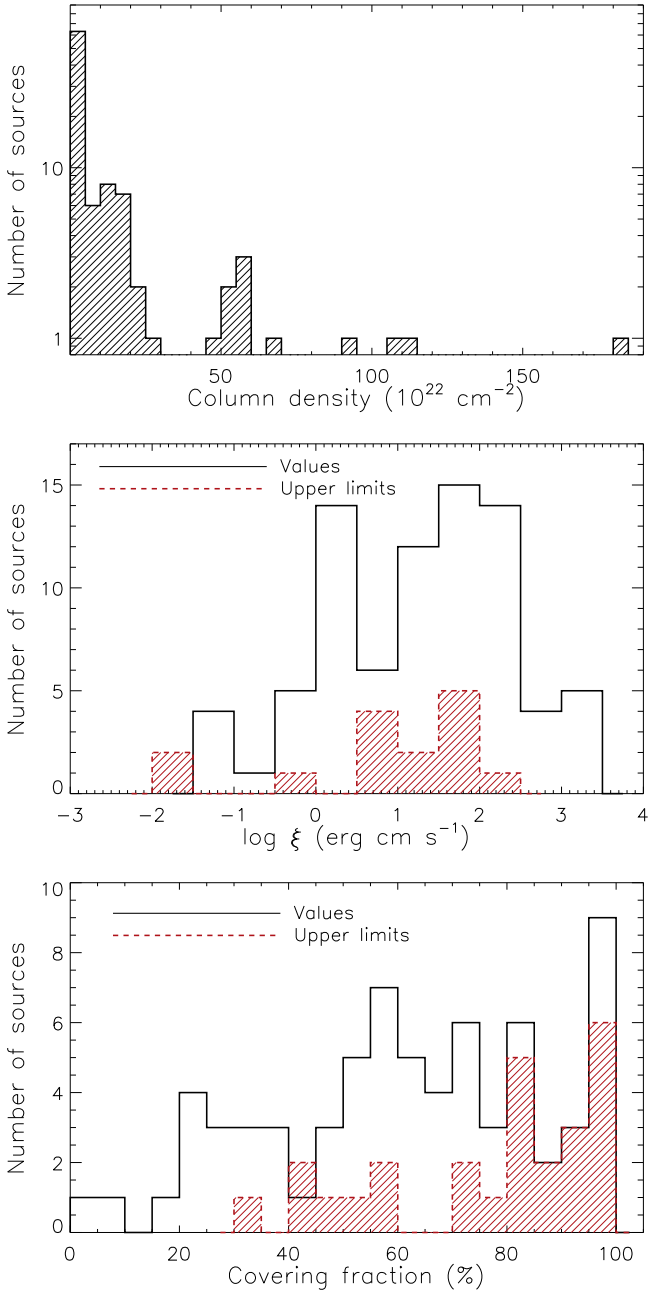

Figure 28. Distribution of the column density (top panel), ionization parameter (middle panel), and covering factor (bottom panel) of the ionized absorbers for the sources of our sample (see Section 5.3.2 for details). For the ionization parameter and the covering factor we also show the values of the upper limits (red dashed lines) obtained. The median values of the parameters are listed in Table 10.

5.4. Soft Excess

5.4.1. Unobscured AGNs

A total of 209 unobscured AGNs (i.e., ∼57%) in our sample show evidence for soft excesses. This is in agreement with what has been found by Winter et al. (2008, 2009a; ∼40%–50%) studying X-ray observations of smaller samples of *Swift*/BAT AGNs, and with previous works carried out with *ASCA*

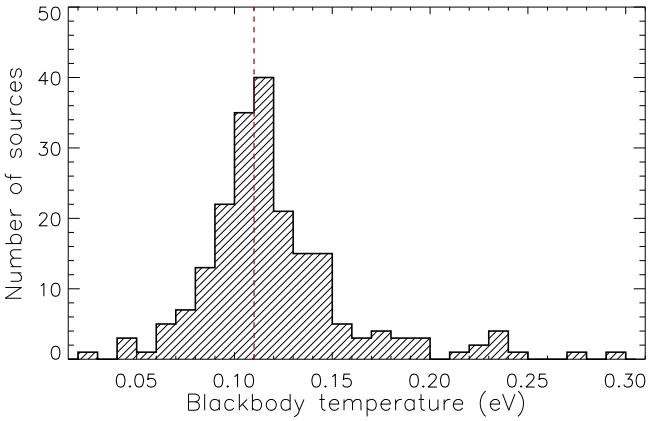

Figure 29. Distribution of the blackbody temperatures obtained for unobscured nonblazar AGNs. The red dashed vertical line shows the median value (see Table 10).

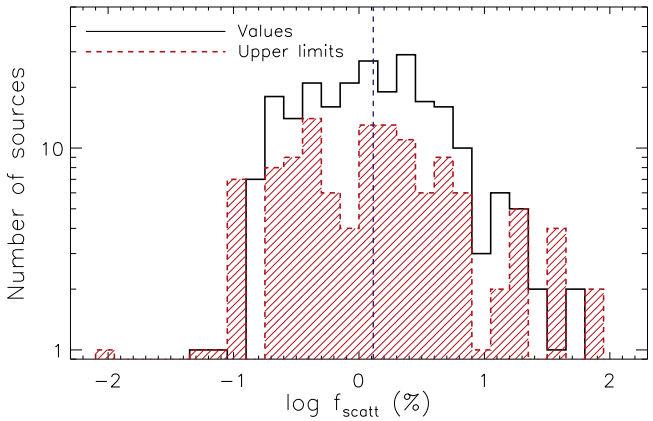

Figure 30. Distribution of the fraction of scattered X-ray radiation inferred for the obscured nonblazar AGNs. The black line represents the measured values, while the red dashed line represents the upper limits. The vertical blue dashed line shows the median value of the distribution (see Table 10).

(∼40%; Reeves & Turner 2000). The presence of a soft excess had been found to be ubiquitous in optically selected quasars (e.g., Piconcelli et al. 2005). Scott et al. (2012) estimated that, by correcting the results obtained for a large sample of type I AGNs (Scott et al. 2011) to take into account detectability, the true percentage of sources with a soft excess is 75% ± 23%. Similarly, studying a sample of 48 Seyfert 1–1.5 galaxies observed by *Suzaku* and *XMM-Newton*, Winter et al. (2012) found that 94% of the objects show a soft excess.

The soft excess was reproduced here using a simple phenomenological model, i.e., a blackbody with a variable temperature and normalization. We found that the median temperature of our sample is $kT_{\rm bb} = 0.110 \pm 0.003$ eV. As shown in Figure 29, the distribution of $kT_{\rm bb}$ is very narrow ($\sigma = 0.04$ eV), which is also in agreement with previous works (e.g., Gierliński & Done 2004; Winter et al. 2012).

5.4.2. Obscured AGNs

The soft excess in obscured AGNs could have several origins. It could be related to Thomson scattering of the primary X-ray radiation in ionized gas, possibly located in the photoionized region (e.g., Noguchi et al. 2010). In support of this idea, Ueda et al. (2015) recently demonstrated that AGNs with low scattering fractions also show smaller ratios of the extinction-corrected [O III] λ5007 emission line to the intrinsic 2–10 keV luminosity. In addition to this, star formation could contribute significantly to the flux below ∼2 keV. X-ray emission in star-forming regions is due to a population of X-ray binaries and to collisionally ionized plasma (e.g., Ranalli et al. 2008). A significant contribution might also come from radiative recombination, which would create emission lines and a continuum below ∼2 keV (e.g., Marinucci et al. 2011).

Here we do not attempt to model photoionized emission, and we reproduced the soft excess in obscured AGNs as a combination of a scattered continuum and one or more collisionally ionized plasmas. A scattered component was added to the X-ray spectral model of 388 sources. The value of $f_{\rm scatt}$ could be constrained for 251 objects, while for 137 only an upper limit was obtained (Figure 30). The median value of the scattered fraction for the objects for which this value could be constrained is $f_{\rm scatt} = 1.4 \pm 0.6\%$, with 101 objects having $f_{\rm scatt} < 1\%$. Following the same approach described in Section 5.2.3, we took into account also the lower limits in the calculation of the median value of $f_{\rm scatt}$ and found a median of $f_{\rm scatt} = 1.0 \pm 0.4\%$ for the total sample (see Table 10). Optically selected AGNs have been shown to have significantly higher values of the fraction of scattered radiation ($f_{\rm scatt} \sim 1\%$–5%; e.g., Bianchi & Guainazzi 2007). Smaller values of $f_{\rm scatt}$ imply either a small opening angle of the torus or a smaller amount of gas responsible for the scattering. Studying *Suzaku* observations of *Swift*/BAT type II AGNs, Ueda et al. (2007) found the first evidence for AGNs with $f_{\rm scatt} < 0.5\%$ and concluded that these objects are "buried AGNs," i.e., objects that have a torus with a very large covering factor (see also Eguchi et al. 2009, 2011). It has been argued by Hönig et al. (2014) that objects with $f_{\rm scatt} < 0.5\%$ reside in highly inclined galaxies or merger systems, which would increase the probability that the scattered emission is obscured by the host galaxy. Ueda et al. (2015) showed that, while in some cases it is possible that the host galaxy is responsible for the lower scattered fraction, more than half of the objects with $f_{\rm scatt} < 0.5\%$ in their sample are free from absorption by interstellar matter along the disk of the host galaxies. In our sample, 93 AGNs (∼25% of the objects) have $f_{\rm scatt} < 0.5\%$. The scattered emission, as well as the relation between $f_{\rm scatt}$ and the physical properties of the accreting system, will be the subject of a forthcoming work (C. Ricci et al., in preparation).

A thermal plasma has been used for 112 objects in total (Figure 31). For 88 objects we applied a single thermal component, while for 23 two components were necessary, and in one case (MCG −03−34−064) we used three thermal plasma components with different temperatures. The median value of the temperature of this component is $kT_{\rm therm.} = 0.49 \pm 0.06$ keV.

6. Summary and Conclusion

We described here our detailed broadband X-ray spectral analysis of the AGNs reported in the *Swift*/BAT 70-month catalog. Soft X-ray (0.3–10 keV) spectra are available for 836 of the 838 sources detected by *Swift*/BAT in its first 70 months of observations, implying a completeness of ∼99.8%. Our sample consists of the 836 *Swift*/BAT sources with soft X-ray observations, of which 731 are non-beamed AGNs and 105 are blazars (26 BL Lacs, 53 flat-spectrum radio quasars, and 26 of uncertain type). A variety of X-ray spectral models were applied to the 0.3–150 keV spectra. The median values of the

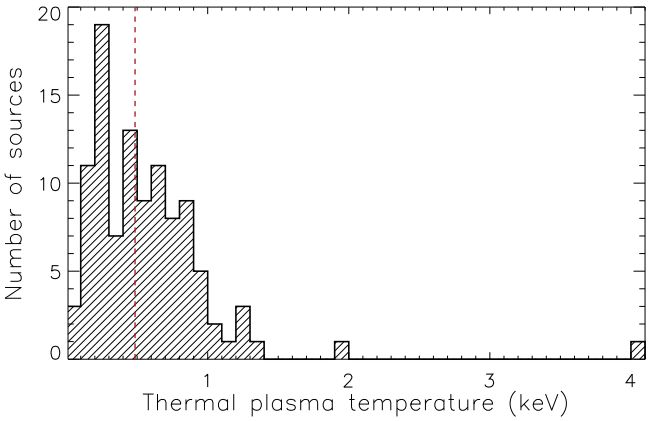

Figure 31. Distribution of the temperatures of the thermal plasma. When more than one component was present, we averaged the values of the temperature of each object. The vertical red dashed line shows the median value of the distribution (see Table 10).

spectral parameters of nonblazar AGNs and blazars obtained by our spectral analysis are listed in Tables 10 and 11, respectively. The sample and the X-ray observation log are listed in Tables 1 and 2, respectively. In Table 5 we report the main spectral parameters obtained by our analysis for all sources. In the following we summarize our main findings.

1. We report the values of the intrinsic (i.e., absorption-corrected and *k*-corrected) luminosities for all objects of our sample in the 2–10 keV, 20–50 keV, 14–150 keV, and 14–195 keV bands. We find that unobscured AGNs have typically higher *intrinsic* luminosities than obscured AGNs, in agreement with the decrease of the fraction of obscured sources with increasing luminosity. Among the blazars, flat-spectrum radio quasars are significantly more luminous, in all the bands discussed here, than BL Lacs, while blazars of uncertain type typically have the lowest luminosities (see Section 5.1 and Figure 14).
2. The median value of the photon index obtained by the broadband X-ray spectral analysis of the nonblazar AGNs is $\Gamma = 1.78 \pm 0.01$. Obscured and unobscured objects have consistent spectral slopes, with medians of $\Gamma = 1.76 \pm 0.02$ and $\Gamma = 1.80 \pm 0.02$, respectively (see Section 5.2.1 and Figure 17). The values of Γ and of the photon index obtained by fitting the 0.3–10 keV spectrum alone ($\Gamma_{0.3-10}$) are typically lower than the *Swift*/BAT photon index ($\Gamma_{\rm BAT}$; see Figure 18). The steepening of the X-ray continuum in the hard X-ray band suggests that the presence of a high-energy cutoff is almost ubiquitous in nonblazar AGNs.
3. Flat-spectrum radio quasars have typically flatter slopes ($\Gamma = 1.54 \pm 0.05$, $\Gamma_{\rm BAT} = 1.71 \pm 0.06$) than BL Lacs ($\Gamma = 2.05 \pm 0.06$, $\Gamma_{\rm BAT} = 2.42 \pm 0.10$). See Section 5.2.1 and Figure 17.
4. A cross-calibration constant was added to all models. We found that both nonblazar AGNs and blazars have a median value of $C_{\rm BAT} = 1$ (see Section 5.2.2 and Figure 20). From the dispersion in $C_{\rm BAT}$ of nonblazar AGNs we conclude that the typical variability of these objects, on the timescales probed by our study (days to several years), is $\sim$0.2 dex.
5. The cutoff energy of nonblazar AGNs, considering also the upper and lower limits (assuming a maximum value of $E_{\rm C} = 1000$ keV), has a median of $E_{\rm C} = 381 \pm 16$ keV, and obscured and unobscured AGNs have consistent median $E_{\rm C}$ (see Section 5.2.3 and the left panel of Figure 21). Ignoring the upper and lower limits, the median values is significantly lower ($E_{\rm C} = 76 \pm 6$ keV). This is due to the fact that, at the typical signal-to-noise ratio of our data, we can mostly constrain values of $E_{\rm C} \lesssim 100$ keV. Using the Kaplan–Meier estimator and including the lower limits, we found that, for the whole sample, the median (mean) is 200 ± 29 keV (319 ± 23 keV).
6. We find that the reflection parameter of nonblazar AGNs, taking into account also upper and lower limits, has a median of $R = 0.53 \pm 0.09$ (see Section 5.2.4 and the right panel of Figure 21). Unobscured objects have a larger median value ($R = 0.83 \pm 0.14$) than Compton-thin obscured AGNs ($R = 0.38 \pm 0.11$) and CT sources ($R = 0.15 \pm 0.12$). The decrease of the reflection component with increasing obscuration is in agreement with the idea that most of the reprocessed X-ray radiation originates in the accretion disk. For the objects for which we could constrain R we find a median value of $R = 1.2 \pm 0.2$. This is larger in unobscured AGNs ($R = 1.4 \pm 0.3$) than in Compton-thin obscured AGNs ($R = 0.6 \pm 0.2$) and in CT sources ($R = 0.25 \pm 0.10$).
7. We find that the nonblazar sample is almost equally divided into AGNs with $N_{\rm H} < 10^{22}$ cm^{-2} (365) and those with $N_{\rm H} \geqslant 10^{22}$ cm^{-2} (366). Among the latter, 56 are Compton-thick ($N_{\rm H} \geqslant 10^{24}$ cm^{-2}) and 75 have column densities consistent with $N_{\rm H} \sim 10^{24}$ cm^{-2} (see Section 5.3.1 and Figure 23).
8. Evidence of ionized absorption is found in 86 AGNs (Section 5.3.2 and Figure 28), most of which are unobscured. This allowed us to conclude that the covering factor of the ionized material in AGNs with $N_{\rm H} < 10^{22}$ cm^{-2} is $\gtrsim$22%.
9. The soft excess in unobscured AGNs could be well reproduced by a blackbody model. We found that the range of temperatures is very narrow, with a median of $kT_{\rm bb} = 0.11$ keV (see Section 5.4.1 and Figure 29).
10. The typical fraction of scattered radiation is $f_{\rm scatt} = 1.0 \pm 0.5$%, lower than what is usually inferred for optically selected AGNs (see Section 5.4.2 and Figure 30). A total of 93 objects ($\sim$25%) have values of $f_{\rm scatt} < 0.5$%, which might imply either that they are surrounded by a torus with a very large covering factor or that the amount of material responsible for the Thomson scattering in these objects is small. A total of 22 (40) objects have values of $f_{\rm scatt} \geqslant 10$% ($\geqslant$5%), which implies either that the obscuring material partially covers the X-ray source or that jet emission contributes significantly to the X-ray flux at $\lesssim$2 keV.

In the tables in the appendices we report the parameters of the broken power laws (Table 6), of the warm absorbers (Table 9), and of the Gaussian lines (Table 8), as well as the observed and intrinsic fluxes (Table 12) and luminosities (Tables 13 and 14). In Table 15 we list the values of $\Gamma_{\rm nEC}$ and $\Gamma_{0.3-10}$, while in Table 9 we report the parameters obtained by fitting with a torus model the broadband X-ray spectra of the 75 AGNs with values of $N_{\rm H}$ consistent with 10^{24} cm^{-2} within their 90% confidence interval.

This work is part of a large effort aimed at shedding light on the multiwavelength properties of the least biased sample of local AGNs available. A series of forthcoming publications will investigate, in detail, the relations between several of the properties measured here and those of the accreting SMBHs and host galaxies. These include, among others, the absorption properties (Ricci et al. 2017c, C. Ricci et al., in preparation), the Fe Kα line (D. Tubin-Arenas et al., in preparation), the fraction of scattered radiation (C. Ricci et al., in preparation), and the relation between mergers and SMBH accretion (M. J. Koss et al., in preparation).

This work is dedicated to the memory of our friend and collaborator Neil Gehrels. We acknowledge the work that the *Swift*/BAT team has done to make this project possible. We thank the anonymous referee for the prompt report that helped us improve the quality of the manuscript. We thank Taro Shimizu and Chin-Shin Chang for valuable discussion and for their help with the manuscript. This work made use of data supplied by the UK Swift Science Data Centre at the University of Leicester. This work is sponsored by the Chinese Academy of Sciences (CAS), through a grant to the CAS South America Center for Astronomy (CASSACA) in Santiago, Chile. We acknowledge financial support from the CONICYT-Chile grants "EMBIGGEN" Anillo ACT1101 (C.R., E.T.), FONDECYT 1141218 (C.R.), FONDECYT 1160999 (E.T.), Basal-CATA PFB–06/2007 (C.R., E.T.), the China-CONICYT fund (C.R.), the Swiss National Science Foundation (grants PP00P2_138979 and PP00P2_166159, K.S.; grant 200021_157021, K.O.), the Swiss National Science Foundation (SNSF) through the Ambizione fellowship grant PZ00P2 154799/1 (M.K.), the National Key R&D Program of China grant No. 2016YFA0400702 (LH), the National Science Foundation of China grants No. 11473002 and 1721303 (LH), the European Union's Seventh Framework program under grant agreement 337595 (ERC Starting Grant, "CoSMass"; I.D.). Part of this work was carried out while C.R. was Fellow of the Japan Society for the Promotion of Science (JSPS) at Kyoto University. This work was partly supported by the Grant-in-Aid for Scientific Research 17K05384 (Y.U.) from the Ministry of Education, Culture, Sports, Science and Technology of Japan (MEXT). This research has made use of the Tartarus (version 3.1) database, created by Paul O'Neill and Kirpal Nandra at Imperial College London and Jane Turner at NASA/GSFC. This publication made use of data products from the *Wide-field Infrared Survey Explorer*, which is a joint project of the University of California, Los Angeles, and the Jet Propulsion Laboratory/California Institute of Technology, funded by the National Aeronautics and Space Administration. This research made use of the NASA/IPAC Extragalactic Database (NED), which is operated by the Jet Propulsion Laboratory, California Institute of Technology, under contract with the National Aeronautics and Space Administration. This research has made use of: the SIMBAD database, operated at CDS, Strasbourg, France (Wenger et al. 2000); the Aladin sky atlas, developed at CDS, Strasbourg Observatory, France (Bonnarel et al. 2000; Boch & Fernique 2014); Astropy, a community-developed core Python package for Astronomy (Astropy Collaboration et al. 2013); TOPCAT (Taylor 2005).

Facilities: AKARI, *ASCA*, *BeppoSAX*, *Chandra*, *GALEX*, *IRAS*, *Suzaku*, *Swift*, *XMM-Newton*, *WISE*.

Appendix A
New Soft X-Ray Counterparts

We found a different X-ray counterpart than that reported by the *Swift*/BAT 70-month catalog and by the studies reported above for only eight sources. In the following we report details about these objects.

SWIFT J0216.3+5128. The X-ray counterpart reported in the BAT catalog is 2MASX J02162987+5126246. The source is instead more likely associated to the X-ray-bright Seyfert 2 IGR J02164+5126/2MASS J02162672+5125251, which is clearly detected in the 10.0 ks *XMM-Newton* EPIC/PN observation (see also Masetti et al. 2009).

SWIFT J0223.4+4551. The *Swift*/BAT source was identified with the triplet of galaxies V Zw 232, but the X-ray counterpart of this object is the central galaxy, 2MASX J02233309+4549162.

SWIFT J0350.1−5019. The source is reported as being the counterpart of 2MASX J03502377−5018354. Besides 2MASX J03502377−5018354, three other X-ray sources are evident around the BAT position of the sources: 2MASX J03501198−5017165, 2MASX J03502377−5018354, and ESO 201−4. The first two objects are too weak to be the counterpart of the *Swift*/BAT source, while the CT AGN ESO 201−4 is at a flux level consistent with that of SWIFT J0350.1−5019.

SWIFT J0528.1−3933. The source is identified with the interacting galaxy pair ESO 306−IG001. From the analysis of the *XMM-Newton* image we found that the X-ray counterpart of this source is ESO 306−IG001 NED01.

SWIFTJ0654.6+0700. This object was previously identified with 2MASS J06543368+0703024 (also in Cusumano et al. 2010b), while we find that the right counterpart is 2MASS J06543417+0703210 (see also Parisi et al. 2014). The new identification is coincident with a bright *WISE* source.

SWIFT J0744.0+2914. The 10.8 ks *Chandra*/ACIS observation did not detect the counterpart reported in the 70-month BAT catalog, UGC 03995A. The most likely counterpart of SWIFT J0744.0+2914 is the nearby galaxy UGC 03995B, which is detected in the 0.3–10 keV band and is interacting with UGC 03995A (Koss et al. 2012).

SWIFT J0919.2+5528. The counterpart is not SBS 0915+556, as reported in the 70-month catalog, but it is the CT AGN Mrk 106, which is significantly brighter and closer to the position of the hard X-ray source than SBS 0915+556.

SWIFT J1238.6+0928. The source was identified as being the hard X-ray counterpart of the galaxy VCC 1759. VCC 1759 was not detected in the 20.1 ks *XMM-Newton* EPIC/PN image, and the most likely counterpart for SWIFT J1238.6+0928 is the Seyfert 2 2MASX J12384342+0927362 (see also Malizia et al. 2016).

SWIFTJ1354.5+1326. The source was originally identified with 2MASX J13542913+1328068, which is part of an interacting galaxy pair with 2MASS J13542908+1327571 (at a distance of 10″). However, the former object is not detected in *WISE*, while the latter has an infrared brightness consistent with what is expected from its intrinsic X-ray flux. Therefore, it is more likely that the *Swift*/BAT source is associated with 2MASS J13542908+1327571.

SWIFT J1535.8−5749. The 0.3–10 keV counterpart of the source is IGR J15360−5750 (Malizia et al. 2010), which is brighter and closer to the BAT position than the object reported in the BAT catalog, 1RXS J153552.8−575055.

SWIFTJ1747.8+6837B. The source was identified with VII Zw 742, a system made of an interacting pair of galaxies (2MASX J17465994+6836392 and 2MASS J17465953 +6836303) with a separation of 8.″8. The two sources are blended in *WISE*, with the southern one being brighter. The *Swift/XRT* observation of this source showed that the position of the X-ray counterpart coincides with that of 2MASS J17465953+6836303.

SWIFTJ1856.1+1539. This object was originally identified with 2MASX J18560128+1538059. However, the right counterpart is more likely to be 2MASS J18560056+1537584, which has a bright, red *WISE* counterpart. This new identification is supported by what is reported by Rodriguez et al. (2008).

SWIFT J2007.0−3433. The *Chandra*/ACIS 0.3–10 keV image shows that the X-ray counterpart is not ESO 399−20, but the nearby galaxy MCG −06−44−018, with which ESO 399−20 is interacting.

Appendix B
Dual AGNs

Several objects in our sample are known to be dual AGNs (e.g., Koss et al. 2012); in the following we discuss the influence of the two sources on the *Swift*/BAT emission and list the cases in which the X-ray spectral properties of both sources are reported in our catalog. Those objects are listed as D1 and D2.

SWIFT J0209.5−1010. This object is the combination of two AGNs at 56″: NGC 833 and NGC 835, with the former having a 2–10 keV flux ∼1/3 of the latter (Koss et al. 2011a). Due to the fact that both sources contribute to the 14–195 keV flux, we report the spectral characteristics of both NGC 833 (SWIFT J0209.5-1010D1) and NGC 835 (SWIFT J0209.5-1010D2).

SWIFT J0324.9+4044. This object is composed of two AGNs at 12″ from each other: IRAS 03219+4031 and 2MASX J03251221+4042021. In the 2–10 keV band IRAS 03219+4031 is ∼12 times brighter than 2MASX J03251221 +4042021 (Koss et al. 2011a) and was therefore considered to be the counterpart of the *Swift*/BAT source.

SWIFT J0602.2+2829. This source is composed of IRAS 05589+2828 and 2MASX J06021107+2828382 (at a distance of 20″), with the former having a 2–10 keV X-ray flux 1100 higher than the latter (Koss et al. 2011a).

SWIFT J0945.6−1420. This object is composed by two sources at 180″ from each other: NGC 2992 and NGC 2993. Since the former AGN is ∼7 times brighter in the 2–10 keV band than the latter (Koss et al. 2011a), it was considered as the counterpart of SWIFT J0945.6−1420.

SWIFT J1023.5+1952. This dual AGN is composed of NGC 3227 and NGC 3226, located at 130″ from each other. In the 2–10 keV band NGC 3227 is ∼73 times brighter than NGC 3226 (Koss et al. 2011a) and was therefore assumed to be the counterpart of SWIFT J1023.5+1952.

SWIFT J1136.0+2132. The counterpart of this source is a late-stage galaxy merger composed of two nuclei with a projected separation of 3.4 kpc (5″): Mrk 739E and Mrk 739W (Koss et al. 2011a). The 2–10 keV observed flux of Mrk 739W is ∼9% of that of Mrk 739E (Koss et al. 2011a), and the latter source was reported as the counterpart of the BAT AGN.

SWIFT J1315.8+4420. This source is composed of UGC 8327 NED01 and UGC 8327 NED02, located at 37″ from each other. The 2–10 keV flux of UGC 8327 NED01 is ∼1140 times higher than that of UGC 8327 NED02 (Koss et al. 2011a), and this source was therefore considered to be the counterpart of the *Swift*/BAT object.

SWIFT J1334.8−2328. The *XMM-Newton* EPIC/PN image reveals that, within the error box of the *Swift*/BAT position, both members of the interacting pair ESO 509−IG066 (Guainazzi et al. 2005) are detected. These two sources are ESO 509−IG066E/NED02 (SWIFT J1334.8−2328D1) and ESO 509−IG066W/NED01 (SWIFT J1334.8−2328D2), with the eastern component having a 2–10 keV flux ∼60% of the western component.

SWIFT J1341.2+3023. The source is composed of two objects at 59″: Mrk 268 and Mrk 268SE. The counterpart of the *Swift*/BAT source is Mrk 268, since it has a 2–10 keV flux >108 times higher than that of its companion (Koss et al. 2011a).

SWIFT J1355.9+1822. This source is another known dual AGN, with the two nuclei (Mrk 463E and Mrk 463W, at 4″) having a projected separation of 3.4 kpc (Bianchi et al. 2008a). The *Chandra* study of Bianchi et al. (2008a) showed that both nuclei are obscured, and Koss et al. (2011a) reported that the 2–10 keV observed flux of Mrk 463W is ∼25% that of Mrk 463E.

SWIFT J1652.9+0223. The luminous infrared galaxy NGC 6240 is known to host two Compton-thick AGNs separated by 0.7 kpc (1.″8): NGC 6240N and NGC 6240S (Komossa et al. 2003). The two sources have comparable observed 2–10 keV fluxes (Koss et al. 2011a), and Puccetti et al. (2016) have recently shown that both sources contribute significantly to the flux above 10 keV. The intrinsic 10–40 keV luminosities are 7.1×10^{43} erg s^{-1} and 2.7×10^{43} erg s^{-1} for the southern and northern nucleus, respectively (Puccetti et al. 2016). Since the *XMM-Newton* observation used here lacks the spatial resolution to resolve the two nuclei, the system was considered to be one source.

SWIFT J1816.0+4236. The source is composed of UGC 11185 NED01 and UGC 11185 NED02 (at 28″). Since UGC 11185 NED02 has a 2–10 keV flux >23.3 times larger than UGC 11185 NED01 (Koss et al. 2011a), it was considered to be the counterpart of the BAT source.

SWIFT J2028.5+2543. This source is a combination of two objects at 91″ from each other: NGC 6921 and MCG +04−48 −002, with the former AGN contributing to ∼20% of the 14–195 keV flux. Since the two AGNs contribute significantly to the *Swift*/BAT flux, we reported the characteristics of both NGC 6921 (SWIFT J2028.5+2543D1) and MCG +04−48 −002 (SWIFT J2028.5+2543D2) in the catalog.

SWIFT J2328.9+0328. This object is the combination of the unobscured AGN NGC 7679 and the CT AGN NGC 7682 (at 270″). Since NGC 7679 contributes to only ∼10% of the 14–195 keV flux, we adopted NGC 7682 as the counterpart of the *Swift*/BAT source.

Appendix C
The Starburst Galaxy SWIFT J0956.1+6942 (M82)

The starburst galaxy M82 does not host an AGN, and its broadband X-ray spectrum was fitted with the D1 model (Section 4.2.4; χ^2/DOF = 1294.9/1209). We obtained a photon index of $\Gamma = 1.31^{+0.43}_{-0.55}$, a cutoff energy of 11^{+17}_{-6} keV, and temperatures of the thermal plasma of $0.68^{+0.23}_{-0.32}$ keV and $1.62^{+0.20}_{-0.13}$ keV. The column density of the neutral material obscuring the cutoff power-law component is $3.5^{+1.1}_{-1.4} \times$

10^{22} cm^{-2}, while that of the material obscuring the thermal plasma is $5.0^{+6.8}_{-2.3} \times 10^{21}$ cm^{-2}. The cross-calibration constant between the *XMM-Newton* and the *Swift*/BAT spectrum is consistent with unity ($C_{\rm BAT} = 1.2^{+0.5}_{-0.3}$).

The observed fluxes in the 2–10 and 14–195 keV bands are $F^{\rm obs}_{2-10} = 11.2 \times 10^{-12}$ erg cm^{-2} s^{-1} and $F^{\rm obs}_{14-195} = 6.4 \times 10^{-12}$ erg cm^{-2} s^{-1}, respectively. The intrinsic fluxes in the 2–10 keV, 20–50 keV, and 14–150 keV bands are $F_{2-10} = 13.8 \times 10^{-12}$ erg cm^{-2} s^{-1}, $F_{20-50} = 2.5 \times 10^{-12}$ erg cm^{-2} s^{-1}, and $F_{14-150} = 5.0 \times 10^{-12}$ erg cm^{-2} s^{-1}, respectively. The intrinsic luminosities, in the same energy ranges, are $\log(L_{2-10}/{\rm erg\ s^{-1}}) = 40.17$, $\log(L_{20-50}/{\rm erg\ s^{-1}}) = 39.43$, and $\log(L_{14-150}/{\rm erg\ s^{-1}}) = 39.73$.

ORCID iDs

C. Ricci https://orcid.org/0000-0001-5231-2645
B. Trakhtenbrot https://orcid.org/0000-0002-3683-7297
M. J. Koss https://orcid.org/0000-0002-7998-9581
Y. Ueda https://orcid.org/0000-0001-7821-6715
I. Del Vecchio https://orcid.org/0000-0001-8706-2252
K. Schawinski https://orcid.org/0000-0001-5464-0888
S. Paltani https://orcid.org/0000-0002-8108-9179
K. Oh https://orcid.org/0000-0002-5037-951X
I. Lamperti https://orcid.org/0000-0003-3336-5498
P. Gandhi https://orcid.org/0000-0003-3105-2615
K. Ichikawa https://orcid.org/0000-0002-4377-903X
F. E. Bauer https://orcid.org/0000-0002-8686-8737
L. C. Ho https://orcid.org/0000-0001-6947-5846
D. Asmus https://orcid.org/0000-0003-0220-2063
V. Beckmann https://orcid.org/0000-0002-2778-8569
M. Baloković https://orcid.org/0000-0003-0476-6647
C. B. Markwardt https://orcid.org/0000-0001-9803-3879

References

Ahn, C. P., Alexandroff, R., Allende Prieto, C., et al. 2014, ApJS, 211, 17
Aird, J., Coil, A. L., Georgakakis, A., et al. 2015, MNRAS, 451, 1892
Ajello, M., Alexander, D. M., Greiner, J., et al. 2012, ApJ, 749, 21
Ajello, M., Costamante, L., Sambruna, R. M., et al. 2009, ApJ, 699, 603
Ajello, M., Rau, A., Greiner, J., et al. 2008, ApJ, 673, 96
Akylas, A., Georgakakis, A., Georgantopoulos, I., Brightman, M., & Nandra, K. 2012, A&A, 546, A98
Akylas, A., Georgantopoulos, I., Ranalli, P., et al. 2016, A&A, 594, A73
Alexander, D. M., Stern, D., Del Moro, A., et al. 2013, ApJ, 773, 125
Annuar, A., Alexander, D. M., Gandhi, P., et al. 2017, ApJ, 836, 165
Annuar, A., Gandhi, P., Alexander, D. M., et al. 2015, ApJ, 815, 36
Arévalo, P., Bauer, F. E., Puccetti, S., et al. 2014, ApJ, 791, 81
Arnaud, K. A. 1996, in ASP Conf. Ser. 101, Astronomical Data Analysis Software and Systems V, ed. G. H. Jacoby & J. Barnes (San Francisco, CA: ASP), 17
Arnouts, S., Cristiani, S., Moscardini, L., et al. 1999, MNRAS, 310, 540
Asmus, D., Gandhi, P., Hönig, S. F., Smette, A., & Duschl, W. J. 2015, MNRAS, 454, 766
Astropy Collaboration, Robitaille, T. P., Tollerud, E. J., et al. 2013, A&A, 558, A33
Ballantyne, D. R. 2014, MNRAS, 437, 2845
Ballantyne, D. R., Bollenbacher, J. M., Brenneman, L. W., et al. 2014, ApJ, 794, 62
Baloković, M., Comastri, A., Harrison, F. A., et al. 2014, ApJ, 794, 111
Baloković, M., Matt, G., Harrison, F. A., et al. 2015, ApJ, 800, 62
Barthelmy, S. D., Barbier, L. M., Cummings, J. R., et al. 2005, SSRv, 120, 143
Bauer, F. E., Alexander, D. M., Brandt, W. N., et al. 2004, AJ, 128, 2048
Bauer, F. E., Arévalo, P., Walton, D. J., et al. 2015, ApJ, 812, 116
Baumgartner, W. H., Tueller, J., Markwardt, C. B., et al. 2013, ApJS, 207, 19
Bautista, M. A., & Kallman, T. R. 2001, ApJS, 134, 139
Beckmann, V., Gehrels, N., Shrader, C. R., & Soldi, S. 2006, ApJ, 638, 642
Beckmann, V., & Shrader, C. R. 2012, Active Galactic Nuclei (Wiley-VCH)
Beckmann, V., Soldi, S., Ricci, C., et al. 2009, A&A, 505, 417
Berney, S., Koss, M., Trakhtenbrot, B., et al. 2015, MNRAS, 454, 3622
Bianchi, S., Chiaberge, M., Piconcelli, E., Guainazzi, M., & Matt, G. 2008a, MNRAS, 386, 105
Bianchi, S., & Guainazzi, M. 2007, in AIP Conf. Ser. 924, The Multicolored Landscape of Compact Objects and Their Explosive Origins, ed. T. di Salvo et al. (Melville, NY: AIP), 822
Bianchi, S., Guainazzi, M., & Chiaberge, M. 2006, A&A, 448, 499
Bianchi, S., La Franca, F., Matt, G., et al. 2008b, MNRAS, 389, L52
Boch, T., & Fernique, P. 2014, in ASP Conf. Ser. 485, Astronomical Data Analysis Software and Systems XXIII, ed. N. Manset & P. Forshay (San Francisco, CA: ASP), 277
Boissay, R., Paltani, S., Ponti, G., et al. 2014, A&A, 567, A44
Boissay, R., Ricci, C., & Paltani, S. 2016, A&A, 588, A70
Bonnarel, F., Fernique, P., Bienaymé, O., et al. 2000, A&AS, 143, 33
Boorman, P. G., Gandhi, P., Alexander, D. M., et al. 2016, ApJ, 833, 245
Brandt, W. N., & Alexander, D. M. 2015, A&ARv, 23, 1
Brenneman, L. W., Madejski, G., Fuerst, F., et al. 2014, ApJ, 788, 61
Brenneman, L. W., & Reynolds, C. S. 2009, ApJ, 702, 1367
Brenneman, L. W., Weaver, K. A., Kadler, M., et al. 2009, ApJ, 698, 528
Brightman, M., Baloković, M., Stern, D., et al. 2015, ApJ, 805, 41
Brightman, M., & Nandra, K. 2011, MNRAS, 413, 1206
Burlon, D., Ajello, M., Greiner, J., et al. 2011, ApJ, 728, 58
Burlon, D., Ghirlanda, G., Murphy, T., et al. 2013, MNRAS, 431, 2471
Burrows, D. N., Hill, J. E., Nousek, J. A., et al. 2005, SSRv, 120, 165
Calzetti, D., Armus, L., Bohlin, R. C., et al. 2000, ApJ, 533, 682
Cash, W. 1979, ApJ, 228, 939
Chen, C.-T. J., Brandt, W. N., Reines, A. E., et al. 2017, ApJ, 837, 48
Corral, A., Della Ceca, R., Caccianiga, A., et al. 2011, A&A, 530, A42
Crummy, J., Fabian, A. C., Gallo, L., & Ross, R. R. 2006, MNRAS, 365, 1067
Cusumano, G., La Parola, V., Segreto, A., et al. 2010a, A&A, 510, A48
Cusumano, G., La Parola, V., Segreto, A., et al. 2010b, A&A, 524, A64
De Luca, A., & Molendi, S. 2004, A&A, 419, 837
Della Ceca, R., Caccianiga, A., Severgnini, P., et al. 2008, A&A, 487, 119
Done, C., Davis, S. W., Jin, C., Blaes, O., & Ward, M. 2012, MNRAS, 420, 1848
Draper, A. R., & Ballantyne, D. R. 2010, ApJL, 715, L99
Eguchi, S., Ueda, Y., Awaki, H., et al. 2011, ApJ, 729, 31
Eguchi, S., Ueda, Y., Terashima, Y., Mushotzky, R., & Tueller, J. 2009, ApJ, 696, 1657
Esposito, V., & Walter, R. 2016, A&A, 590, A49
Evans, D. A., Kraft, R. P., Worrall, D. M., et al. 2004, ApJ, 612, 786
Evans, P. A., Beardmore, A. P., Page, K. L., et al. 2009, MNRAS, 397, 1177
Fabian, A. C., Iwasawa, K., Reynolds, C. S., & Young, A. J. 2000, PASP, 112, 1145
Fabian, A. C., Lohfink, A., Kara, E., et al. 2015, MNRAS, 451, 4375
Fabian, A. C., Zoghbi, A., Ross, R. R., et al. 2009, Natur, 459, 540
Ferrarese, L., & Merritt, D. 2000, ApJL, 539, L9
Fossati, G., Maraschi, L., Celotti, A., Comastri, A., & Ghisellini, G. 1998, MNRAS, 299, 433
Fruscione, A., McDowell, J. C., Allen, G. E., et al. 2006, Proc. SPIE, 6270, 62701V
Gabriel, C., Denby, M., Fyfe, D. J., et al. 2004, in ASP Conf. Ser. 314, Astronomical Data Analysis Software and Systems (ADASS) XIII, ed. F. Ochsenbein, M. G. Allen, & D. Egret (San Francisco, CA: ASP), 759
Gandhi, P., Fabian, A. C., Suebsuwong, T., et al. 2007, MNRAS, 382, 1005
Gandhi, P., Hönig, S. F., & Kishimoto, M. 2015, ApJ, 812, 113
Gandhi, P., Horst, H., Smette, A., et al. 2009, A&A, 502, 457
Gandhi, P., Isobe, N., Birkinshaw, M., et al. 2011, PASJ, 63, 505
Gandhi, P., Lansbury, G. B., Alexander, D. M., et al. 2014, ApJ, 792, 117
Garmire, G. P., Bautz, M. W., Ford, P. G., Nousek, J. A., & Ricker, G. R., Jr. 2003, Proc. SPIE, 4851, 28
Gebhardt, K., Bender, R., Bower, G., et al. 2000, ApJL, 539, L13
Gehrels, N., Chincarini, G., Giommi, P., et al. 2004, ApJ, 611, 1005
George, I. M., Turner, T. J., Netzer, H., et al. 1998, ApJS, 114, 73
Ghisellini, G., Tavecchio, F., Foschini, L., et al. 2010, MNRAS, 402, 497
Giacconi, R., Gursky, H., Paolini, F. R., & Rossi, B. B. 1962, PhRvL, 9, 439
Gierliński, M., & Done, C. 2004, MNRAS, 349, L7
Gilli, R., Comastri, A., & Hasinger, G. 2007, A&A, 463, 79
Gofford, J., Reeves, J. N., Tombesi, F., et al. 2013, MNRAS, 430, 60
Guainazzi, M., & Bianchi, S. 2007, MNRAS, 374, 1290
Guainazzi, M., Piconcelli, E., Jiménez-Bailón, E., & Matt, G. 2005, A&A, 429, L9
Haardt, F., Fossati, G., Grandi, P., et al. 1998, A&A, 340, 35
Haardt, F., & Maraschi, L. 1991, ApJL, 380, L51
Hardcastle, M. J., Evans, D. A., & Croston, J. H. 2006, MNRAS, 370, 1893

Hardcastle, M. J., Evans, D. A., & Croston, J. H. 2009, MNRAS, 396, 1929
Harrison, F. A., Aird, J., Civano, F., et al. 2016, ApJ, 831, 185
Harrison, F. A., Craig, W. W., Christensen, F. E., et al. 2013, ApJ, 770, 103
Hogg, J. D., Winter, L. M., Mushotzky, R. F., Reynolds, C. S., & Trippe, M. 2012, ApJ, 752, 153
Hönig, S. F., Gandhi, P., Asmus, D., et al. 2014, MNRAS, 438, 647
Ichikawa, K., Ricci, C., Ueda, Y., et al. 2017, ApJ, 835, 74
Ichikawa, K., Ueda, Y., Terashima, Y., et al. 2012, ApJ, 754, 45
Ilbert, O., Arnouts, S., McCracken, H. J., et al. 2006, A&A, 457, 841
Inoue, Y., & Totani, T. 2009, ApJ, 702, 523
Ishisaki, Y., Maeda, Y., Fujimoto, R., et al. 2007, PASJ, 59, 113
Iwasawa, K., Mainieri, V., Brusa, M., et al. 2012, A&A, 537, A86
Iwasawa, K., Sanders, D. B., Teng, S. H., et al. 2011, A&A, 529, A106
Jansen, F., Lumb, D., Altieri, B., et al. 2001, A&A, 365, L1
Kaastra, J. S., Mewe, R., Liedahl, D. A., Komossa, S., & Brinkman, A. C. 2000, A&A, 354, L83
Kalberla, P. M. W., Burton, W. B., Hartmann, D., et al. 2005, A&A, 440, 775
Kallman, T., & Bautista, M. 2001, ApJS, 133, 221
Kaspi, S., Brandt, W. N., Netzer, H., et al. 2000, ApJL, 535, L17
Kataoka, J., Reeves, J. N., Iwasawa, K., et al. 2007, PASJ, 59, 279
Kawamuro, T., Ueda, Y., Tazaki, F., Ricci, C., & Terashima, Y. 2016a, ApJS, 225, 14
Kawamuro, T., Ueda, Y., Tazaki, F., Terashima, Y., & Mushotzky, R. 2016b, ApJ, 831, 37
Komossa, S., Burwitz, V., Hasinger, G., et al. 2003, ApJL, 582, L15
Kormendy, J., & Ho, L. C. 2013, ARA&A, 51, 511
Kormendy, J., & Richstone, D. 1995, ARA&A, 33, 581
Koss, M., Mushotzky, R., Baumgartner, W., et al. 2013, ApJL, 765, L26
Koss, M., Mushotzky, R., Treister, E., et al. 2011a, ApJL, 735, L42
Koss, M., Mushotzky, R., Treister, E., et al. 2012, ApJL, 746, L22
Koss, M., Mushotzky, R., Veilleux, S., et al. 2011b, ApJ, 739, 57
Koss, M., Mushotzky, R., Veilleux, S., & Winter, L. 2010, ApJL, 716, L125
Koss, M., Trakhtenbrot, B., Ricci, C., et al. 2017, ApJ, 850, 74
Koss, M. J., Assef, R., Baloković, M., et al. 2016a, ApJ, 825, 85
Koss, M. J., Glidden, A., Baloković, M., et al. 2016b, ApJL, 824, L4
Koss, M. J., Romero-Cañizales, C., Baronchelli, L., et al. 2015, ApJ, 807, 149
Koyama, K., Tsunemi, H., Dotani, T., et al. 2007, PASJ, 59, 23
Krimm, H. A., Holland, S. T., Corbet, R. H. D., et al. 2013, ApJS, 209, 14
Lamperti, I., Koss, M., Trakhtenbrot, B., et al. 2017, MNRAS, 467, 540
Lansbury, G. B., Alexander, D. M., Aird, J., et al. 2017a, ApJ, 846, 20
Lansbury, G. B., Gandhi, P., Alexander, D. M., et al. 2015, ApJ, 809, 115
Lansbury, G. B., Stern, D., Aird, J., et al. 2017b, ApJ, 836, 99
Lubiński, P., Beckmann, V., Gibaud, L., et al. 2016, MNRAS, 458, 2454
Lutovinov, A. A., Burenin, R. A., Revnivtsev, M. G., & Bikmaev, I. F. 2012, AstL, 38, 1
Lutz, D., Maiolino, R., Spoon, H. W. W., & Moorwood, A. F. M. 2004, A&A, 418, 465
Magdziarz, P., & Zdziarski, A. A. 1995, MNRAS, 273, 837
Malizia, A., Bassani, L., Bazzano, A., et al. 2012, MNRAS, 426, 1750
Malizia, A., Bassani, L., & Negueruela, I. 2000, A&A, 359, 509
Malizia, A., Bassani, L., Sguera, V., et al. 2010, MNRAS, 408, 975
Malizia, A., Landi, R., Molina, M., et al. 2016, MNRAS, 460, 19
Malizia, A., Molina, M., Bassani, L., et al. 2014, ApJL, 782, L25
Marchese, E., Braito, V., Reeves, J. N., et al. 2014, MNRAS, 437, 2806
Marchesi, S., Ajello, M., Comastri, A., et al. 2017, ApJ, 836, 116
Marinucci, A., Bianchi, S., Matt, G., et al. 2011, A&A, 526, A36
Marinucci, A., Matt, G., Bianchi, S., et al. 2015, MNRAS, 447, 160
Marinucci, A., Matt, G., Kara, E., et al. 2014a, MNRAS, 440, 2347
Marinucci, A., Matt, G., Miniutti, G., et al. 2014b, ApJ, 787, 83
Marinucci, A., Tortosa, A. & NuSTAR AGN Physics Working Group 2016, AN, 337, 490
Markwardt, C. B., Tueller, J., Skinner, G. K., et al. 2005, ApJL, 633, L77
Martin, D. C., Fanson, J., Schiminovich, D., et al. 2005, ApJL, 619, L1
Maselli, A., Massaro, F., Cusumano, G., et al. 2013, ApJS, 206, 17
Masetti, N., Parisi, P., Jiménez-Bailón, E., et al. 2012, A&A, 538, A123
Masetti, N., Parisi, P., Palazzi, E., et al. 2009, A&A, 495, 121
Masetti, N., Parisi, P., Palazzi, E., et al. 2010, A&A, 519, A96
Massaro, E., Giommi, P., Leto, C., et al. 2009, A&A, 495, 691
Massaro, E., Maselli, A., Leto, C., et al. 2015, Ap&SS, 357, 75
Matt, G., Baloković, M., Marinucci, A., et al. 2015, MNRAS, 447, 3029
Matt, G., Marinucci, A., Guainazzi, M., et al. 2014, MNRAS, 439, 3016
Matt, G., Perola, G. C., & Piro, L. 1991, A&A, 247, 25
Mehdipour, M., Branduardi-Raymont, G., Kaastra, J. S., et al. 2011, A&A, 534, A39
Meléndez, M., Kraemer, S. B., Armentrout, B. K., et al. 2008, ApJ, 682, 94
Meléndez, M., Mushotzky, R. F., Shimizu, T. T., Barger, A. J., & Cowie, L. L. 2014, ApJ, 794, 152
Miniutti, G., & Fabian, A. C. 2004, MNRAS, 349, 1435
Mitsuda, K., Bautz, M., Inoue, H., et al. 2007, PASJ, 59, 1
Murphy, K. D., & Yaqoob, T. 2009, MNRAS, 397, 1549
Mushotzky, R. F., Done, C., & Pounds, K. A. 1993, ARA&A, 31, 717
Mushotzky, R. F., Fabian, A. C., Iwasawa, K., et al. 1995, MNRAS, 272, L9
Mushotzky, R. F., Shimizu, T. T., Meléndez, M., & Koss, M. 2014, ApJL, 781, L34
Mushotzky, R. F., Winter, L. M., McIntosh, D. H., & Tueller, J. 2008, ApJL, 684, L65
Nandra, K. 2006, MNRAS, 368, L62
Nandra, K., George, I. M., Mushotzky, R. F., Turner, T. J., & Yaqoob, T. 1997, ApJ, 477, 602
Nandra, K., & Pounds, K. A. 1994, MNRAS, 268, 405
Netzer, H. 2013, The Physics and Evolution of Active Galactic Nuclei (Cambridge: Cambridge Univ. Press)
Netzer, H. 2015, ARA&A, 53, 365
Neugebauer, G., Habing, H. J., van Duinen, R., et al. 1984, ApJL, 278, L1
Noguchi, K., Terashima, Y., Ishino, Y., et al. 2010, ApJ, 711, 144
Oda, S., Tanimoto, A., Ueda, Y., et al. 2017, ApJ, 835, 179
Oh, K., Schawinski, K., Koss, M., et al. 2017, MNRAS, 464, 1466
Onori, F., La Franca, F., Ricci, F., et al. 2017a, MNRAS, 464, 1783
Onori, F., Ricci, F., La Franca, F., et al. 2017b, MNRAS, 468, L97
Page, M. J., Breeveld, A. A., Soria, R., et al. 2003, A&A, 400, 145
Paltani, S., Walter, R., McHardy, I. M., et al. 2008, A&A, 485, 707
Panessa, F., Bassani, L., de Rosa, A., et al. 2008, A&A, 483, 151
Parisi, P., Masetti, N., Jiménez-Bailón, E., et al. 2009, A&A, 507, 1345
Parisi, P., Masetti, N., Jiménez-Bailón, E., et al. 2012, A&A, 545, A101
Parisi, P., Masetti, N., Rojas, A. F., et al. 2014, A&A, 561, A67
Parker, M. L., Wilkins, D. R., Fabian, A. C., et al. 2014, MNRAS, 443, 1723
Patrick, A. R., Reeves, J. N., Porquet, D., et al. 2012, MNRAS, 426, 2522
Piconcelli, E., Bianchi, S., Vignali, C., Jiménez-Bailón, E., & Fiore, F. 2011, A&A, 534, A126
Piconcelli, E., Jimenez-Bailón, E., Guainazzi, M., et al. 2005, A&A, 432, 15
Polletta, M., Tajer, M., Maraschi, L., et al. 2007, ApJ, 663, 81
Puccetti, S., Comastri, A., Bauer, F. E., et al. 2016, A&A, 585, A157
Ranalli, P., Comastri, A., Origlia, L., & Maiolino, R. 2008, MNRAS, 386, 1464
Reeves, J., Done, C., Pounds, K., et al. 2008, MNRAS, 385, L108
Reeves, J. N., & Turner, M. J. L. 2000, MNRAS, 316, 234
Reynolds, C. S. 1997, MNRAS, 286, 513
Reynolds, C. S. 2014, SSRv, 183, 277
Ricci, C., Assef, R. J., Stern, D., et al. 2017a, ApJ, 835, 105
Ricci, C., Bauer, F. E., Arevalo, P., et al. 2016a, ApJ, 820, 5
Ricci, C., Bauer, F. E., Treister, E., et al. 2016b, ApJ, 819, 4
Ricci, C., Bauer, F. E., Treister, E., et al. 2017b, MNRAS, 468, 1273
Ricci, C., Beckmann, V., Audard, M., & Courvoisier, T. J.-L. 2010, A&A, 518, A47
Ricci, C., Paltani, S., Awaki, H., et al. 2013a, A&A, 553, A29
Ricci, C., Paltani, S., Ueda, Y., & Awaki, H. 2013b, MNRAS, 435, 1840
Ricci, C., Trakhtenbrot, B., Koss, M. J., et al. 2017c, Natur, 549, 488
Ricci, C., Ueda, Y., Ichikawa, K., et al. 2014a, A&A, 567, A142
Ricci, C., Ueda, Y., Koss, M. J., et al. 2015, ApJL, 815, L13
Ricci, C., Ueda, Y., Paltani, S., et al. 2014b, MNRAS, 441, 3622
Ricci, C., Walter, R., Courvoisier, T. J.-L., & Paltani, S. 2011, A&A, 532, A102
Ricci, F., La Franca, F., Onori, F., & Bianchi, S. 2017d, A&A, 598, A51
Rodriguez, J., Tomsick, J. A., & Chaty, S. 2008, A&A, 482, 731
Salvato, M., Hasinger, G., Ilbert, O., et al. 2009, ApJ, 690, 1250
Salvato, M., Ilbert, O., Hasinger, G., et al. 2011, ApJ, 742, 61
Sambruna, R. M., Donato, D., Ajello, M., et al. 2010, ApJ, 710, 24
Schawinski, K., Khochfar, S., Kaviraj, S., et al. 2006, Natur, 442, 888
Schawinski, K., Koss, M., Berney, S., & Sartori, L. F. 2015, MNRAS, 451, 2517
Scott, A. E., Stewart, G. C., Mateos, S., et al. 2011, MNRAS, 417, 992
Scott, A. E., Stewart, G. C., & Mateos, S. 2012, MNRAS, 423, 2633
Segreto, A., Cusumano, G., Ferrigno, C., et al. 2010, A&A, 510, A47
She, R., Ho, L. C., & Feng, H. 2017a ApJ, 835, 223
She, R., Ho, L. C., & Feng, H. 2017b ApJ, 842, 131
Shimizu, T. T., Meléndez, M., Mushotzky, R. F., et al. 2016, MNRAS, 456, 3335
Shimizu, T. T., & Mushotzky, R. F. 2013, ApJ, 770, 60
Shimizu, T. T., Mushotzky, R. F., Meléndez, M., Koss, M., & Rosario, D. J. 2015, MNRAS, 452, 1841
Shu, X. W., Yaqoob, T., & Wang, J. X. 2010, ApJS, 187, 581

Shu, X. W., Yaqoob, T., & Wang, J. X. 2011, ApJ, 738, 147
Singh, K. P., Tandon, S. N., Agrawal, P. C., et al. 2014, Proc. SPIE, 9144, 91441S
Skrutskie, M. F., Cutri, R. M., Stiening, R., et al. 2006, AJ, 131, 1163
Smith, K. L., Koss, M., & Mushotzky, R. F. 2014, ApJ, 794, 112
Soldi, S., Beckmann, V., Baumgartner, W. H., et al. 2014, A&A, 563, A57
Soldi, S., Türler, M., Paltani, S., et al. 2008, A&A, 486, 411
Stern, D. 2015, ApJ, 807, 129
Stern, D., Lansbury, G. B., Assef, R. J., et al. 2014, ApJ, 794, 102
Stroh, M. C., & Falcone, A. D. 2013, ApJS, 207, 28
Strüder, L., Briel, U., Dennerl, K., et al. 2001, A&A, 365, L18
Tanimoto, A., Ueda, Y., Kawamuro, T., & Ricci, C. 2016, PASJ, 68, S26
Taylor, M. B. 2005, in ASP Conf. Ser. 347, Astronomical Data Analysis Software and Systems XIV, ed. P. Shopbell, M. Britton, & R. Ebert (San Francisco, CA: ASP), 29
Tazaki, F., Ueda, Y., Terashima, Y., & Mushotzky, R. F. 2011, ApJ, 738, 70
Tazaki, F., Ueda, Y., Terashima, Y., Mushotzky, R. F., & Tombesi, F. 2013, ApJ, 772, 38
Teng, S. H., Mushotzky, R. F., Sambruna, R. M., Davis, D. S., & Reynolds, C. S. 2011, ApJ, 742, 66
Tombesi, F., Cappi, M., Reeves, J. N., et al. 2010a, A&A, 521, A57
Tombesi, F., Cappi, M., Reeves, J. N., et al. 2013, MNRAS, 430, 1102
Tombesi, F., Sambruna, R. M., Reeves, J. N., et al. 2010b, ApJ, 719, 700
Tortosa, A., Marinucci, A., Matt, G., et al. 2017, MNRAS, 466, 4193
Trakhtenbrot, B., Ricci, C., Koss, M. J., et al. 2017, MNRAS, 470, 800
Treister, E., & Urry, C. M. 2005, ApJ, 630, 115
Treister, E., & Urry, C. M. 2006, ApJL, 652, L79
Treister, E., Urry, C. M., & Virani, S. 2009, ApJ, 696, 110
Tremaine, S., Gebhardt, K., Bender, R., et al. 2002, ApJ, 574, 740
Tueller, J., Baumgartner, W. H., Markwardt, C. B., et al. 2010, ApJS, 186, 378
Tueller, J., Mushotzky, R. F., Barthelmy, S., et al. 2008, ApJ, 681, 113
Turner, T. J., & Miller, L. 2009, A&ARv, 17, 47
Turner, T. J., Nandra, K., Turcan, D., & George, I. M. 2001, in AIP Conf. ser. 599, X-RAY ASTRONOMY: Stellar Endpoints, AGN, and the Diffuse X-ray Background, ed. N. E. White, G. Malaguti, & G. G. C. Palumbo (Melville, NY: AIP), 991
Ueda, Y., Akiyama, M., Hasinger, G., Miyaji, T., & Watson, M. G. 2014, ApJ, 786, 104
Ueda, Y., Akiyama, M., Ohta, K., & Miyaji, T. 2003, ApJ, 598, 886
Ueda, Y., Eguchi, S., Terashima, Y., et al. 2007, ApJL, 664, L79
Ueda, Y., Hashimoto, Y., Ichikawa, K., et al. 2015, ApJ, 815, 1
Ulrich, M.-H., Maraschi, L., & Urry, C. M. 1997, ARA&A, 35, 445
Ursini, F., Marinucci, A., Matt, G., et al. 2015, MNRAS, 452, 3266
Vasudevan, R. V., Brandt, W. N., Mushotzky, R. F., et al. 2013a, ApJ, 763, 111
Vasudevan, R. V., Fabian, A. C., Reynolds, C. S., et al. 2016, MNRAS, 458, 2012
Vasudevan, R. V., Mushotzky, R. F., & Gandhi, P. 2013b, ApJL, 770, L37
Vasudevan, R. V., Mushotzky, R. F., Reynolds, C. S., et al. 2014, ApJ, 785, 30
Vasudevan, R. V., Mushotzky, R. F., Winter, L. M., & Fabian, A. C. 2009, MNRAS, 399, 1553
Weaver, K. A., Meléndez, M., Mushotzky, R. F., et al. 2010, ApJ, 716, 1151
Weisskopf, M. C., Tananbaum, H. D., Van Speybroeck, L. P., & O'Dell, S. L. 2000, Proc. SPIE, 4012, 2
Wenger, M., Ochsenbein, F., Egret, D., et al. 2000, A&AS, 143, 9
Wilms, J., Allen, A., & McCray, R. 2000, ApJ, 542, 914
Winkler, C., Courvoisier, T. J.-L., Di Cocco, G., et al. 2003, A&A, 411, L1
Winter, L. M., Lewis, K. T., Koss, M., et al. 2010, ApJ, 710, 503
Winter, L. M., Mushotzky, R. F., Reynolds, C. S., & Tueller, J. 2009a, ApJ, 690, 1322
Winter, L. M., Mushotzky, R. F., Terashima, Y., & Ueda, Y. 2009b, ApJ, 701, 1644
Winter, L. M., Mushotzky, R. F., Tueller, J., & Markwardt, C. 2008, ApJ, 674, 686
Winter, L. M., Veilleux, S., McKernan, B., & Kallman, T. R. 2012, ApJ, 745, 107
Wong, O. I., Koss, M. J., Schawinski, K., et al. 2016, MNRAS, 460, 1588
Wright, E. L., Eisenhardt, P. R. M., Mainzer, A. K., et al. 2010, AJ, 140, 1868
Young, A. J., Wilson, A. S., & Shopbell, P. L. 2001, ApJ, 556, 6